VOLUME 33 MAY 1955 NUMBER 5

Canadian Journal of Physics

Editor: G. M. VOLKOFF

Associate Editors:

L. G. ELLIOTT, *Atomic Energy of Canada, Ltd., Chalk River*
J. S. FOSTER, *McGill University*
G. HERZBERG, *National Research Council of Canada*
L. LEPRINCE-RINGUET, *Ecole Polytechnique, Paris*
D. W. R. McKINLEY, *National Research Council of Canada*
B. W. SARGENT, *Queen's University*
Sir FRANCIS SIMON, *Clarendon Laboratory, University of Oxford*
W. H. WATSON, *University of Toronto*

Published by THE NATIONAL RESEARCH COUNCIL
OTTAWA CANADA

CANADIAN JOURNAL OF PHYSICS

(*Formerly Section A, Canadian Journal of Research*)

Under the authority of the Chairman of the Committee of the Privy Council on Scientific and Industrial Research, the National Research Council issues THE CANADIAN JOURNAL OF PHYSICS and six other journals devoted to the publication, in English or French, of the results of original scientific research. Matters of general policy concerning these journals are the responsibility of a joint Editorial Board consisting of: members representing the National Research Council of Canada; the Editors of the Journals; and members representing the Royal Society of Canada and four other scientific societies.

EDITORIAL BOARD

Representatives of the National Research Council

A. N. Campbell, *University of Manitoba*
G. E. Hall, *University of Western Ontario*
E. G. D. Murray, *McGill University*
D. L. Thomson, *McGill University*
W. H. Watson (Chairman), *University of Toronto*

Editors of the Journals

D. L. Bailey, *University of Toronto*
J. B. Collip, *University of Western Ontario*
E. H. Craigie, *University of Toronto*
G. A. Ledingham, *National Research Council*
Léo Marion, *National Research Council*
R. G. E. Murray, *University of Western Ontario*
G. M. Volkoff, *University of British Columbia*

Representatives of Societies

D. L. Bailey, *University of Toronto*
Royal Society of Canada
J. B. Collip, *University of Western Ontario*
Canadian Physiological Society
E. H. Craigie, *University of Toronto*
Royal Society of Canada
R. G. E. Murray, *University of Western Ontario*
Canadian Society of Microbiologists
H. G. Thode, *McMaster University*
Chemical Institute of Canada
T. Thorvaldson, *University of Saskatchewan*
Royal Society of Canada
G. M. Volkoff, *University of British Columbia*
Royal Society of Canada; Canadian Association of Physicists

Ex officio

Léo Marion (Editor-in-Chief), *National Research Council*

Manuscripts for publication should be submitted to Dr. Léo Marion, Editor-in-Chief, Canadian Journal of Physics, National Research Council, Ottawa 2, Canada.
(For instructions on preparation of copy, see **Notes to Contributors** (inside back cover).)

Proof, correspondence concerning proof, and orders for reprints should be sent to the Manager, Editorial Office (Research Journals), Division of Administration, National Research Council, Ottawa 2, Canada.

Subscriptions, renewals, requests for single or back numbers, and all remittances should be sent to Division of Administration, National Research Council, Ottawa 2, Canada. Remittances should be made payable to the Receiver General of Canada, credit National Research Council.

The journals published, frequency of publication, and prices are:

Canadian Journal of Biochemistry and Physiology	Bimonthly	$3.00 a year
Canadian Journal of Botany	Bimonthly	$4.00 a year
Canadian Journal of Chemistry	Monthly	$5.00 a year
Canadian Journal of Microbiology*	Bimonthly	$3.00 a year
Canadian Journal of Physics	Monthly	$4.00 a year
Canadian Journal of Technology	Bimonthly	$3.00 a year
Canadian Journal of Zoology	Bimonthly	$3.00 a year

The price of single numbers of all journals is 75 cents.

*Volume 1 will combine three numbers published in 1954 with six published in 1955 and will be available at the regular annual subscription rate of $3.00.

Canadian Journal of Physics

Issued by THE NATIONAL RESEARCH COUNCIL OF CANADA

VOLUME 33 MAY 1955 NUMBER 5

A SUGGESTED METHOD FOR STUDYING THE MECHANISM OF ENERGY TRANSFER IN COLLISIONS[1]

BY TA-YOU WU

ABSTRACT

It is shown that information can be obtained concerning the nature of the energy transfer process in collisions in which an excited atom (or molecule) A′ transfers its energy of excitation to another atom (or molecule) B,

$$A'+B \rightarrow A+B', \text{ cross section } \sigma_q,$$

by comparing the experimental value of the ratio of the cross section σ_q and the σ_{ex} of the inverse process with the theoretical values of this ratio for various modes of excitation of B, which values can be readily obtained from statistical mechanical considerations alone. For example, for the study of the nature of the "quenching" collisions, the ratio σ_q/σ_{ex} can be determined from a measurement of the intensity of the radiation emitted by A′ as a function of time. Such measurements are possible with the photomultiplier and electronic timing circuit techniques now available.

INTRODUCTION

There are many collision processes in which an atom or molecule A in an excited state (electronic, vibrational, or rotational) transfers its energy of excitation upon collision to another atom or molecule B thereby exciting B to an excited state, namely,

$$A'+B \rightarrow A+B'. \quad [1]$$

A familiar type of such processes is the so-called quenching collisions in which the emission of radiation by the excited atom A′ is "quenched" by the admixture of a foreign gas. A great deal of experimental work has been done on such problems as the cross sections of various atoms or molecules B for the quenching of various excited states of different atoms or molecules A (2). While in some cases it is possible to tell with great plausibility the nature of the excitation of B, no direct theoretical or experimental method seems available for ascertaining the exact mode in which the particle B has taken up the energy transferred from A. The purpose of the present note is to suggest a method for a study of this aspect of such processes.

THEORY

Let N_n, N_k be the number densities of atom (or molecule) N in states n, k respectively. Let X_a, X_b be the number densities of atom (or molecule) X in

[1]*Manuscript received January 6, 1955.*
Contribution from the Division of Physics, National Research Council, Ottawa, Canada. Issued as N.R.C. No. 3565.

states a, b respectively. Let us consider the collision process in which the atom N in state k on colliding with atom X in state a transfers its energy of excitation $E_k - E_n$ to X, thereby raising the latter to a state b, i.e.,

$$[2] \qquad N_k + X_a \rightarrow N_n + X_b + \text{K.E.},$$

where K.E. represents the amount of kinetic energy given by

$$[3] \qquad \text{K.E.} = (E_k - E_n) - (E_b - E_a)$$

and may be positive or negative. Let σ_q be the cross section of [2]. $\sigma_q(v)$, for a given pair of atoms N_k, X_a, is a function of the relative velocity v of the atoms N_k and X_a. $\sigma_q(v)$ has been measured for a large number of cases.

If now the theoretical values of the cross section $\sigma_q(v)$ for various kinds of energy transfer mechanisms were known, a comparison of these values with the observed $\sigma_q(v)$ would enable one to know the actual process taking place under the conditions of the experiment. A theoretical evaluation of $\sigma_q(v)$ for any given process, however, necessitates a knowledge of the interaction potential involving the particles N and X, and a quantum mechanical calculation of $\sigma_q(v)$ with this potential. A knowledge of such a potential is not available even for the simplest of systems N+X, and even if such a potential were known, the calculation of $\sigma_q(v)$ would still have to be carried out with many approximations whose validity is usually difficult to judge. In the following, a method is suggested which does not call for any theoretical calculation of the $\sigma_q(v)$ themselves, but only the ratio of σ_q and the cross section $\sigma_{ex}(u)$ of the inverse process of [2],

$$[4] \qquad N_n + X_b + \text{K.E.} \rightarrow N_k + X_a.$$

$\sigma_{ex}(u)$ is a function of the relative velocity u of N_n and X_b. The ratio $\sigma_q(v)/\sigma_{ex}(u)$ for any given mode of energy transfer process is an "atomic" property and can be obtained from statistical mechanical considerations alone. Thus the principle of detailed balancing gives

$$[5] \qquad \frac{v\,\sigma_q(v)}{u\,\sigma_{ex}(u)} = \frac{g_n\,g_b\,g_u}{g_k\,g_a\,g_v},$$

where g_n, g_k are the statistical weights of the states n, k of N; g_b, g_a those of states b, a of X, respectively; g_v is the number of states of the system N_k and X_a having relative velocities between v and $v+dv$, etc.; and u, v are related by the energy equation

$$[6] \qquad E_k + E_a + \tfrac{1}{2}\mu v^2 = E_n + E_b + \tfrac{1}{2}\mu u^2,$$

where μ is the reduced mass of the particles N and X. The ratio σ_q/σ_{ex}, depending on the g's of N and X before and after the collision, is determined by the nature of the energy transfer process. It can be readily calculated for any assumed mechanism. Thus, for the following cases:

Case 1—Translational excitation of X *alone*

One has

$$\frac{g_u}{g_v} = \frac{u^2\,du}{v^2\,dv}, \qquad g_b = g_a,$$

and from [6],

$$u|du| = v|dv|,$$

so that

$$\frac{\sigma_q(v)}{\sigma_{ex}(u)} = \left(\frac{u}{v}\right)^2 \frac{g_n}{g_k}.$$

If the process [2] involves the transfer of electronic energy $E_k - E_n$ of about 2 ev. into the translational motion of the particles initially having thermal energies, i.e., $\frac{1}{2}\mu v^2 \simeq kT$ ($T \simeq 300°$K.) = 0.03 ev., then $(u/v)^2 \simeq 10^2$, and

$$\frac{\sigma_q(v)}{\sigma_{ex}(u)} \simeq 10^2 \frac{g_n}{g_k}. \tag{7}$$

Case 2—Vibrational excitation of X *alone*

For exact resonance and for the non-degenerate vibrational states of X, one has

$$u = v, \qquad g_b/g_a = 1,$$

and

$$\frac{v\,\sigma_q(v)}{u\,\sigma_{ex}(u)} = \frac{g_n}{g_k}. \tag{8}$$

Case 3—Rotational excitation of X *alone*

In this case, $u = v$, and

$$\frac{v\,\sigma_q(v)}{u\,\sigma_{ex}(u)} = \frac{g_n}{g_k} \cdot \begin{cases} (2J_b+1)/(2J_a+1), \\ (2J_b+1)^2/(2J_a+1)^2, \end{cases} \tag{9}$$

the upper value on the right being for linear or symmetrical top molecules, the lower one for spherical top molecules. If $E_k - E_n \simeq 2$ ev., and

$$(J_a+1)\frac{h^2}{4\pi^2 I} \simeq kT, \qquad J_b^2 \frac{h^2}{8\pi^2 I} \simeq 2 \text{ ev.},$$

then

$$\frac{\sigma_q(v)}{\sigma_{ex}(u)} \simeq \frac{g_n}{g_k} \cdot \begin{cases} 10/\sqrt{J_a}, \\ 10^2/J_a, \end{cases} \tag{9a}$$

for linear or symmetrical top, and spherical molecules respectively.

Case 4—Electronic plus translational excitation of X

In this case

$$\frac{\sigma_q(v)}{\sigma_{ex}(u)} = \frac{g_n}{g_k}\frac{g_b^e}{g_a^e}\left(\frac{u}{v}\right)^2$$

where g^e denotes the statistical weight of the electronic states of X. If $\Delta E = \frac{1}{2}\mu(u^2 - v^2)$ has to go into the translational motion of N and X, then

$$\frac{\sigma_q(v)}{\sigma_{ex}(u)} = \frac{g_n}{g_k}\frac{g_b^e}{g_a^e}\left[1 + \frac{\Delta E}{\frac{1}{2}\mu v^2}\right]. \tag{10}$$

Case 5—Vibrational plus translational excitation of X

Similarly,

$$[11] \qquad \frac{\sigma_q(v)}{\sigma_{ex}(u)} = \frac{g_n\, g_b^v}{g_k\, g_a^v}\left[1+\frac{\Delta E}{\frac{1}{2}\mu v^2}\right]$$

where g^v denotes the statistical weight of the vibrational states of X. Similar expressions can readily be written down for any other assumed mechanisms.

It is seen from the expressions [7]–[11] that, if the ratio $\sigma_q(v)/\sigma_{ex}(u)$ can be determined experimentally, a comparison of the experimental value of this ratio with the theoretical values of σ_q/σ_{ex} for various assumed mechanisms will enable one to know the actual process taking place in the experiment.

A SUGGESTED EXPERIMENT

Let us illustrate the method by the following experiment. A gas containing a mixture of N_n and X_a (both, say, are in their normal states) is excited by the absorption by N_n of radiation $\nu_{kn} = (E_k - E_n)/h$ in a flash of very short duration. Let the number densities at this instant ($t = 0$) be $N_n(0)$, $N_k(0)$. Let the intensity of the emitted radiation by the gas be measured as a function of time in small time intervals (say, in intervals of 10^{-7} sec., from $t = 0$ to 10^{-2} or 10^{-1} sec., depending on the pressure of the gases). Such measurements can now be carried out with the techniques developed by McCoubrey and others (1). Initially, the N_k atoms disappear through the emission of radiation ν_{kn} (or various radiations if there are more than one allowed transitions from state k), and through the "quenching" collisions by X,

$$[12] \qquad dN_k/dt = -(A + v\sigma_q(v)X_a(0))N_k$$

where A is the Einstein A coefficient for the transition $k \rightarrow n$ (or the sum of A coefficients $\sum_m A_{km}$). A being known either theoretically or from a separate measurement without quenching collisions, $v\sigma_q$ can be determined.

At time t, N_k is removed by emission and by quenching, but is replenished by re-excitation by the inverse process [4], and

$$[13] \qquad dN_k/dt = -(A + v\sigma_q(v)X_a(t))N_k(t) + u\sigma_{ex}(u)X_b(t)N_k(t).$$

If the initial $N_k(0)$ can disappear only either by emission of radiation or by the quenching process (2) (i.e., if the effect of the walls etc. can be neglected), then

$$[14] \qquad X_b(t) = N_k(0) - N_k(t) - A\int_0^t N_k(t)\, dt.$$

Also

$$[15] \qquad N_n(t) = N_0 - N_k(t),$$

where N_0 is the total number density of N atoms. If the experimental condition is such that

$$[16] \qquad N_0 \gg N_k(0) > N_k(t),$$

and if, to a first approximation, we replace $N_k(t)$ in the integrand [14] by $N_k(0)[1-e^{-At}]$, we have, from [13]–[16],

[17] $dN_k/dt \simeq -[A+v\,\sigma_q(v)X_a(t)+u\,\sigma_{ex}(u)N_0]N_k(t)+u\,\sigma_{ex}(u)N_0N_k(0)e^{-At}.$

Again, on replacing $X_a(t)$ by $X_a(0)$, equation [17] can readily be solved, giving

[18] $$N_k(t) = N_k(0)\left[1+\frac{v\,\sigma_q(v)\,X_a(0)}{u\,\sigma_{ex}(u)\,N_0}\right]^{-1}e^{-At}.$$

The ln $N_k(t)$ vs. t curve thus has an initial slope $-[A+v\sigma_q(v)X_a(0)]$ and an asymptotic slope $-A$ for large t. The difference between the intercepts of the initial tangent and the asymptotic tangent is

[19] $$\ln\left[1+\frac{v\,\sigma_q(v)X_a(0)}{u\,\sigma_{ex}(u)N_0}\right]$$

from which the ratio $v\sigma_q(v)/u\sigma_{ex}(u)$ can be determined. It is seen that only relative intensities of the emitted radiation need to be measured for determining this ratio, since the factor $N_k(0)$ in $N_k(t)$ to which the intensity is proportional cancels out in the expression [19].

The above analysis holds for an experiment with many simplifying assumptions corresponding to special conditions of the experiment. Thus the removal of both excited N_k and X_b by processes other than [2] and [4] and the effect of "imprisonment" of the emitted radiation have been neglected. To a certain extent these simplifying assumptions can be made valid by properly choosing the conditions of the experiment such as the pressures of N and X atoms and the size of the tube. For any actual experimental condition, a similar but more complicated analysis to obtain the ratio σ_q/σ_{ex} from the appropriate data can be carried out.

REFERENCES

1. McCoubrey, A. O. Phys. Rev. 82: 567. 1951. Phys. Rev. 1955. In press. Phelps, A. V. and Molnar, J. P. Phys. Rev. 89: 1202. 1953.
2. Mitchell, A. G. C. and Zemansky, M. V. Resonance radiation and excited atoms. Cambridge University Press, London. 1934.

NUCLEAR MAGNETIC RESONANCE SPECTRUM OF B^{11} IN KERNITE[1]

By H. H. Waterman[2] and G. M. Volkoff

ABSTRACT

The radio-frequency spectrum of B^{11} in a single crystal of $Na_2B_4O_7.4H_2O$ (kernite) is examined experimentally as the monoclinic crystal is rotated in an external magnetic field of 7060 gauss in turn about each of three axes (b, c crystallographic axes, and a third perpendicular direction) held normal to the magnetic field. A maximum of 21 lines (some of which show small additional splitting) is observed, which reduces to 11 when the b symmetry axis is perpendicular or parallel to the magnetic field. The results are interpreted in terms of four essentially non-equivalent B^{11} sites in kernite characterized respectively by quadrupole coupling constants $|eQ\phi_{zz}/h| = 0.645\pm0.003$, 0.588 ± 0.003, 2.563 ± 0.007, 2.567 ± 0.010 Mc./sec., and asymmetry parameters $\eta \equiv (\phi_{xx}-\phi_{yy})/\phi_{zz} = 0.54\pm0.01$, 0.60 ± 0.02, 0.163 ± 0.010, 0.116 ± 0.010. The orientations of the principal axes of the four ϕ_{ij} tensors are also determined. These observations on boron are consistent with previous X-ray results, but preliminary observations on Na^{23} in kernite contradict previous X-ray position assignments.

1. INTRODUCTION

Two previous papers from this laboratory (14, 10) reported observations on the radio-frequency nuclear resonance spectra of Li^7 and Al^{27} in a single crystal of $LiAl(SiO_3)_2$ (spodumene). These observations were interpreted in terms of the perturbation of the Zeeman energy levels of the nuclei in the external magnetic field H_0, into which the crystal was placed, by the interaction of the nuclear electric quadrupole moments with axially asymmetric crystalline electric field gradients at the nuclear sites. In this paper the spectrum of B^{11} in a single crystal of $Na_2B_4O_7.4H_2O$ (kernite) is treated in a similar way.

The object of this investigation is twofold: (1) to demonstrate the applicability to more complicated spectra of methods of analyzing nuclear resonance spectra in single crystals which were previously tested experimentally only on simpler special cases, and (2) to obtain quantitative data on quadrupole coupling tensors at B^{11} sites in kernite.

Although spodumene contains four Li (and four Al) atoms per unit cell, the known symmetry of the crystal guarantees that all four Li (or Al) sites are completely equivalent from the point of view of the field gradient tensor and that, moreover, one of the principal axes of this tensor coincides with the twofold symmetry axis of the monoclinic spodumene crystal. This advance knowledge of the direction of one of the tensor axes further simplifies the analysis of the observed spectrum, which in any case is a simple one consisting of only $2I$ lines (three for Li^7, five for Al^{27}) for *all* orientations of the crystal with respect to the external magnetic field, since all the Li (or Al) sites in a unit cell, and therefore in the whole crystal, are equivalent.

[1]*Manuscript received February 2, 1955.*
Contribution from the Department of Physics, University of British Columbia, Vancouver, B.C. Work supported by grants from the National Research Council of Canada.
[2]*On study leave from the Defence Research Board of Canada. Now at the Naval Research Establishment, Dartmouth, N.S.*

We decided to extend the study of nuclear resonance spectra in single crystals to a more general case in which several non-equivalent sites for a given nuclear species are present in a single crystal, and to demonstrate that the theory previously developed (13) to interpret the simple spectra can also be used to facilitate the identification of lines and the interpretation of the more complex spectra produced by the superposition of several simple spectra each of which is due to nuclei in one of the several non-equivalent sites.

The spin of B^{11} is known to be $I = 3/2$, so that only three lines would be expected (as for Li^7 in spodumene) if all the boron sites in a crystal were equivalent. Observations on the B^{11} spectrum in kernite showed that for those orientations of the monoclinic crystal in which its twofold axis of symmetry was perpendicular or parallel to the external magnetic field 11 lines were evident, while in all other orientations of the crystal 21 lines were obtained, which varied in frequency and relative intensity as the crystal was rotated in the magnetic field. In all cases one of the lines had a frequency which did not depend on crystal orientation and was very close to the unperturbed Larmor frequency ν_0. This number of lines can be explained by assuming four essentially non-equivalent boron sites in kernite (by "essentially non-equivalent" we shall denote those sites which differ in the eigenvalues of the electric field gradient tensor), with four more sites obtained from these by a 180° rotation about a symmetry axis. These differ from the first four only in the orientation of the field gradient tensor principal axes. The principal axes at any pair of sites related by a 180° rotation are symmetrically inclined with respect to the symmetry axis, and therefore with respect to the external magnetic field, whenever the symmetry axis is parallel or perpendicular to the field. In this latter case the field gradient tensors at the two sites related by a rotation become equivalent from the point of view of the perturbation of the Zeeman levels which they produce, and the four essentially non-equivalent sites can give rise to a maximum of $4 \times 3 = 12$ lines. For all other crystal orientations the two sites related by a rotation have non-equivalent orientations with respect to the magnetic field, so that there are eight non-equivalent sites which can give rise to a maximum of $8 \times 3 = 24$ lines. However, if the field gradients at two of the four essentially non-equivalent sites are assumed to be sufficiently weak that only first order perturbation effects are observable, then the two central lines for these two sites in the special crystal orientations, or the four central lines for these two sites, and for the other two derived from them by a 180° rotation in the general orientation, all coincide at the unperturbed Larmor frequency ν_0, reducing the theoretically possible maximum of 12 and 24 lines to 11 and 21 lines respectively. This hypothesis is supported by the detailed analysis of the spectrum given below which yields the complete information (eigenvalues and orientation of principal axes) for the quadrupole coupling tensors $eQ\phi_{ij}/h$ at the four essentially non-equivalent boron sites. Preliminary results of this analysis have been reported earlier (3, 15).

The above conclusion as to the existence of four essentially non-equivalent boron sites and of a twofold symmetry axis in kernite is derived directly from the observed nuclear resonance spectrum, independently of, but in agreement

with, information available from previous X-ray studies of kernite (11, 7). On the other hand, some preliminary results on the Na^{23} spectrum in kernite reported below lead to results directly contradicting the proposal made on the basis of X-ray studies (11, 7) of placing some Na^{23} atoms on the symmetry axis of the crystal.

An additional small splitting, independent of the value of H_0, of some of the B^{11} lines in some crystal orientations has been observed. Its magnitude is such that it might be explained by dipole–dipole interaction of adjacent B^{11} nuclei, but a detailed study of its dependence on crystal orientation has not yet been made.

2. THEORY

A summary of the relevant theory from a previous paper (13) specialized to the case $I = 3/2$ is presented here for convenience. In the case that the electric quadrupole interaction is weak in comparison with the magnetic interaction, each of the non-equivalent sites gives rise to three lines: a "central" line ν_c from the transition $m = \frac{1}{2} \leftrightarrow -\frac{1}{2}$, and two "satellites" ν', ν'' from the transitions $m = \pm\frac{3}{2} \leftrightarrow \pm\frac{1}{2}$. If the crystal is rotated about *any* axis perpendicular to the magnetic field H_0 the following dependence of the three frequencies ν_c, ν', ν'' on the angle of rotation θ about the chosen axis is expected:

$$[1] \qquad \nu'-\nu'' = a + b\cos 2\theta + c\sin 2\theta,$$

$$[2] \qquad \bar{\nu}-\nu_0 = n + p\cos 2\theta + r\sin 2\theta + u\cos 4\theta + v\sin 4\theta,$$

where $\bar{\nu}$ stands either for ν_c or for $\frac{1}{2}(\nu'+\nu'')$ and $\nu_0 = \mu H_0/hI$ is the unperturbed Larmor frequency expected in the absence of effects due to quadrupole interaction. If the crystal is rotated in turn about each of three mutually perpendicular axes X, Y, Z chosen so that they can be easily identified with respect to the crystallographic axes, then three independent sets of the coefficients a, b, c, n, p, r, u, v may be obtained from the experimentally observed curves showing the dependence of $\nu'-\nu''$ and $\bar{\nu}-\nu_0$ on θ_X, θ_Y, and θ_Z. These coefficients are related to the components of the quadrupole coupling tensor $\psi_{ij} \equiv eQ\phi_{ij}/h$ (where ϕ is the electrostatic potential at the nuclear site and eQ is the nuclear electric quadrupole moment) expressed in terms of the X, Y, Z axes by the following equations. In equation [1] for the frequency splitting $\nu'-\nu''$ of a pair of satellites in the X rotation we have:

$$[3] \qquad \begin{aligned} a_X &= \tfrac{1}{2}(\psi_{YY} + \psi_{ZZ}), \\ b_X &= \tfrac{1}{2}(\psi_{YY} - \psi_{ZZ}), \\ c_X &= -\psi_{YZ}. \end{aligned}$$

Equation [1] neglects terms of third and higher odd orders in the ratio of the electric quadrupole to magnetic interactions.

In equation [2] for the shift of the center of gravity $\bar{\nu}-\nu_0 = \frac{1}{2}(\nu'+\nu'')-\nu_0$ of the pair of satellites in the X rotation we have:

$$\tilde{n}_X = \frac{1}{12\nu_0}(b_X^2+c_X^2+c_Y^2+c_Z^2),$$

$$\tilde{p}_X = -\frac{1}{12\nu_0}(c_Y^2-c_Z^2),$$

[4] $$\tilde{r}_X = -\frac{1}{6\nu_0}c_Y c_Z,$$

$$\tilde{u}_X = -\frac{1}{12\nu_0}(b_X^2-c_X^2),$$

$$\tilde{v}_X = -\frac{1}{6\nu_0}b_X c_X.$$

In equation [2] for the shift of the central line $\nu_c-\nu_0$ in the X rotation we have:

$$n_X = \frac{1}{96\nu_0}[18a_X^2-7(b_X^2+c_X^2)-4(c_Y^2+c_Z^2)],$$

$$p_X = \frac{1}{8\nu_0}[-a_X b_X+c_Y^2-c_Z^2],$$

[5] $$r_X = \frac{1}{8\nu_0}[-a_X c_X+2c_Y c_Z],$$

$$u_X = \frac{3}{32\nu_0}(b_X^2-c_X^2),$$

$$v_X = \frac{3}{16\nu_0}b_X c_X.$$

Equation [2] neglects terms of the fourth and higher even orders in the ratio of the electric quadrupole to magnetic interactions.

Corresponding relations for the rotations about the Y and Z axes may be obtained by a cyclic permutation of the subscripts. A consequence of Laplace's equation are the identities:

[6] $$a_X = \tfrac{1}{2}(b_Y-a_Y) = -\tfrac{1}{2}(b_Z+a_Z),$$
$$b_X = -\tfrac{1}{2}(3a_Y+b_Y) = \tfrac{1}{2}(3a_Z-b_Z).$$

The experimental values of n, p, r, u, v lead to values of a, b, c. These, combined with other values of a, b, c, obtained from the $\nu'-\nu''$ curves, lead through equations [3] to values of the components of the quadrupole coupling tensor ψ_{ij} in the X, Y, Z coordinate system. The relative, but not the absolute, signs of these components are determined because in this experiment it is not possible to find out which of the two observed satellites ν', ν'' corresponds to which of the two transitions $m = \pm\frac{3}{2} \leftrightarrow \pm\frac{1}{2}$.

This tensor can then be diagonalized in the usual way as outlined in (14). Setting

[7] $$a \equiv (\psi_{XY}^2+\psi_{YZ}^2+\psi_{ZX}^2-\psi_{XX}\psi_{YY}-\psi_{YY}\psi_{ZZ}-\psi_{ZZ}\psi_{XX}),$$
$$b \equiv (\psi_{XX}\psi_{YY}\psi_{ZZ}+2\psi_{XY}\psi_{YZ}\psi_{ZX}-\psi_{XX}\psi_{YZ}^2-\psi_{YY}\psi_{ZX}^2-\psi_{ZZ}\psi_{XY}^2),$$

we compute first

[8] $$\alpha = \frac{1}{3}\arccos\left[\frac{|b|}{2}\left(\frac{3}{a}\right)^{3/2}\right], \qquad 0 \leqslant \alpha \leqslant \tfrac{1}{6}\pi,$$

and then*

[9] $$\gamma_n = 2\left(\frac{a}{3}\right)^{\frac{1}{2}}\cos\left(\alpha-\frac{2\pi n}{3}\right), \qquad n = 1, 2, 3.$$

We then have

[10] $$|C_z| \equiv |eQ\phi_{zz}/h| = |\psi_{zz}| = \gamma_3; \qquad \eta \equiv (\phi_{zz}-\phi_{yy})/\phi_{zz} = (\gamma_1-\gamma_2)/\gamma_3.$$

The direction cosines λ_n, μ_n, ν_n of the principal axes x, y, z ($n = 1, 2, 3$) of the ψ_{ij} tensor with respect to the axes X, Y, Z are given by

[11] $$\frac{\lambda_n}{D_{1n}} = \frac{\mu_n}{D_{2n}} = \frac{\nu_n}{D_{3n}} = \pm(D_{1n}^2+D_{2n}^2+D_{3n}^2)^{-\frac{1}{2}}$$

where

[12] $$D_{1n} = \psi_{XY}\psi_{YZ}-\psi_{ZX}[\psi_{YY}-\gamma_n],$$
$$D_{2n} = \psi_{ZX}\psi_{XY}-\psi_{YZ}[\psi_{XX}-\gamma_n],$$
$$D_{3n} = (\psi_{XX}-\gamma_n)(\psi_{YY}-\gamma_n)-\psi_{XY}^2.$$

The relative, but not the absolute, sign of λ_n, μ_n, ν_n is determined by equations [11], [12] since for the second rank tensor ψ_{ij} it does not matter which direction along a principal axis is chosen to be the positive one.

3. APPARATUS AND EXPERIMENTAL PROCEDURE

The recording nuclear resonance spectrometer used in this work presents no novel features. Its details are available in a Ph.D. thesis by one of us (16). Its block diagram is identical with that of Reference (14). The oscillating detector uses a circuit very similar to that described by Watkins (17). The external magnetic field of 7060 gauss in a gap 2.08 in. wide and 7.5 in. in diameter is provided by a permanent magnet utilizing 1040 lb. of Alnico 5 as the flux producing element, and 3000 lb. of construction steel as the yoke. Armco iron is used for the pole tips. Using the Al^{27} signal from a solution of $AlCl_3$ Dr. R. G. Eades, who also used the same magnet, determined the temperature variation of the magnetic field of this magnet to be a decrease of 9 parts in 10^5 per 1° F. temperature rise in the neighborhood of 75° F. For the B^{11} frequency of 9.66 Mc./sec. this shift amounts to -0.87 kc./sec. ° F. Since the magnet temperature changed by as much as 4° F. in the course of a rotation, this correction had to be applied. However, with this correction, the frequency of strong lines could be reproduced to within about 150 c./sec. For the investigation of the dependence on the magnetic field of the small addi-

*In Ref. (14) the exponent in γ_n was erroneously given as $\frac{1}{2}$.

tional line splitting observed in some crystal orientations the older spectrometer using an electromagnet and described in Ref. (14) was used.

The frequency of the oscillating detector was measured by mixing in a radio receiver the radiation from the detector with that from a frequency meter, and displaying the output of the receiver on an oscilloscope. When the beat frequency passed through zero a mark was made on the record chart. Such marks were made at intervals of from 10 kc./sec. to 30 kc./sec., and linear interpolation was used in between.

The axis about which the crystal was rotated in the magnetic field could be made perpendicular to the field to within 0.1°. The scale on the final improved version of the crystal mount which measured the angle of rotation θ of the crystal about this axis permitted θ to be read to within 0.1°.

Several specimens of kernite were used in this investigation. Specimens I*a* ($1\frac{1}{4}\times\frac{1}{2}\times\frac{3}{8}$ in.), I*b* ($2\times\frac{3}{4}\times\frac{1}{2}$ in.), I*c* ($\frac{5}{8}\times\frac{5}{8}\times\frac{3}{4}$ in.) all came from one original crystal, and were used to obtain preliminary data for the X rotation. I*a* was also used for studying the effect of the magnetic field on the small additional line splitting. Specimen II ($\frac{3}{4}\times\frac{1}{2}\times\frac{1}{2}$ in.) was used for a preliminary study of the Z rotation. Specimens III ($1\frac{3}{4}\times\frac{5}{8}\times\frac{3}{8}$ in.), I*c*, and IV ($\frac{5}{8}\times\frac{1}{2}\times\frac{1}{2}$ in.) were used for the quantitative X, Y, Z rotations respectively. The X axis was chosen parallel to the b crystallographic axis of the monoclinic kernite crystal which was determined by the intersection of the clean (100) and (001) cleavage planes which were identified by Dr. R. M. Thompson of the U.B.C. Geology Dept. The (100) cleavage plane contains both the b and c axis. The normal to this plane was chosen as the Y axis. The c axis was chosen for the Z rotation axis. This is defined as the line in the (100) plane which is perpendicular to the b axis.

4. EXPERIMENTAL RESULTS AND CALCULATIONS

The observations consisted of recording the resonance absorption spectrum of kernite over a wide frequency range for each one of many crystal positions as the crystal was rotated in turn about its X, Y, Z axes which were held perpendicular to the magnetic field. $\theta = 0°$ in each of these rotations corresponds respectively to the Y, Z, X axes lined up with H_0. Two such sample chart records are reproduced in Figs. 1(*a*), (*b*). As the crystal was rotated most of these lines shifted in frequency, occasionally coalescing and crossing over one another, and varied in relative intensity. The line width of these lines also varied considerably with crystal orientation but was of the order of 7 kc./sec. (equivalent to approximately 5 gauss, as compared to a magnetic field inhomogeneity of about 0.2 gauss) between the maxima of the recorded derivative curve. Several hundred crystal positions spaced by a few degrees were first investigated semiquantitatively to trace out the dependence on the angle of rotation of the frequencies of each of the individual lines. This resulted in curves like those of Figs. 2, 3 which show the dependence on θ_z of the frequencies of some of the 21 lines observed. Each crystal position corresponds to a chart of the type of Fig. 1, and each point for a given crystal position corresponds to a B^{11} line on the chart.

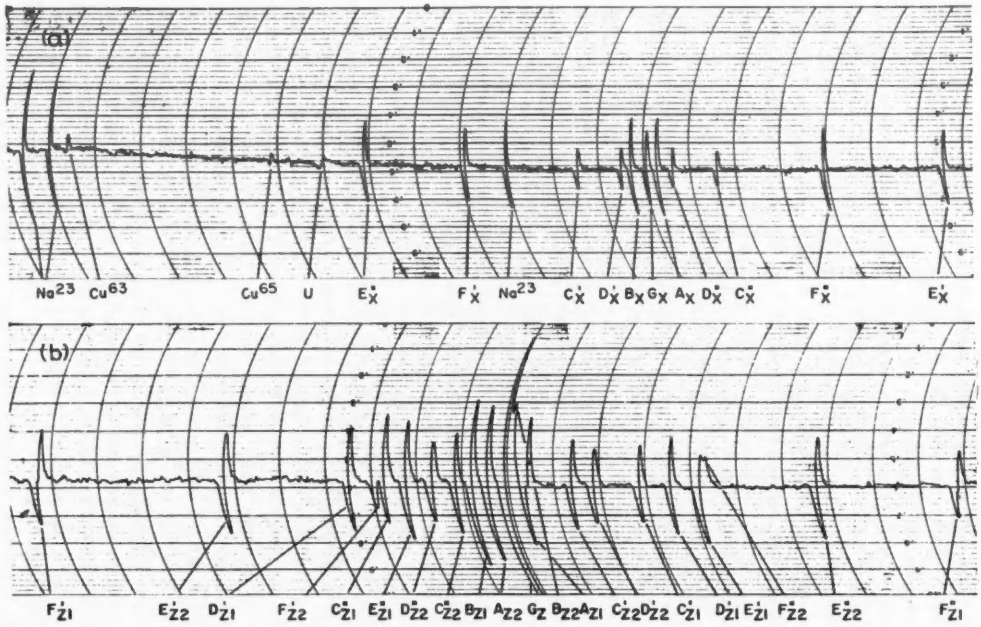


FIG. 1. Selected traces of the recorded derivative of absorption lines (mostly B^{11}) in kernite. The various lines have been identified as labelled (cf. Table I).

(*a*) $\theta_X = 30°$. Sweep rate is approximately 120 kc./sec. per chart division, and the frequency range covered is 7.85 to 10.6 Mc./sec. from left to right. The X symmetry axis of the crystal is perpendicular to H_0. $\theta_X = 0°$ corresponds to the Z axis (c crystal axis) perpendicular to H_0. The line marked U is probably a Na^{23} satellite line.

(*b*) $\theta_Z = 30°$. Sweep rate is approximately 65 kc./sec. per chart division, and the frequency range covered is 8.9 to 10.4 Mc./sec. from left to right. $\theta_Z = 0°$ corresponds to the X symmetry axis along H_0. The lines F'_{Z1}, A_{Z1}, F''_{Z1} show a slight splitting (a break in the steep part of the derivative curve).

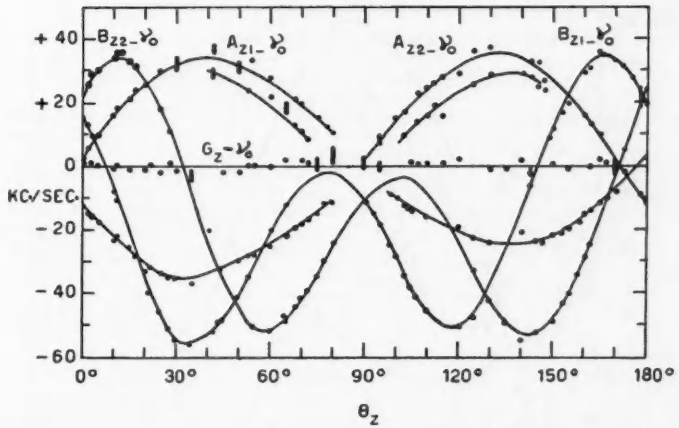


FIG. 2. Semiquantitative study of the dependence on the angular position of kernite sample II of $\nu_c - \nu_0$, where ν_c is the frequency of the "central" lines A_{Z1}, A_{Z2}, B_{Z1}, B_{Z2}, G_Z (cf. Table I) of the B^{11} spectrum for the Z rotation about the crystal c axis, and $\nu_0 = 9.660$ Mc./sec. $\theta_Z = 0°$ corresponds to the b symmetry axis of the crystal along H_0. The lines A_{Z1} and A_{Z2} show some splitting, and the lower parts of the A_Z curves drawn through the experimental points are not joined to the upper parts because of the large number of unresolved lines all falling together near $\phi_Z = 90°$. The B_Z lines are not split in this rotation and a curve of the theoretically expected form is fitted to the experimental points. The G_Z line does not differ appreciably from ν_0. The plotted points have not been corrected for the temperature dependence of the magnetic field.

In addition to the B^{11} lines the chart of Fig. 1(a) contains some Na^{23} lines, and Cu^{63} and Cu^{65} lines. The latter come from the copper in the oscillator coil, and are recognized by their asymmetric shape, and by their frequencies being independent of crystal position and corresponding to the given H_0 and the known gyromagnetic ratios of the two copper isotopes. The "central" lines due to B^{11} and Na^{23} are recognized by their strong intensity and weak dependence on crystal orientation, and by their proximity to the frequencies calculated from the known value of H_0 and the known gyromagnetic ratios of the B^{11} and Na^{23} nuclei. The satellite lines can not be identified by looking at just a single chart of the type shown in Fig. 1, but are identified by looking at the angular dependence of the curves of the type shown in Figs. 2, 3, and by noticing whether these curves are disposed symmetrically with respect to the B^{11} or the Na^{23} "central" lines. In this way the identification of the individual lines on the charts of Fig. 1 has been made.

As described in the introductory section four essentially non-equivalent boron sites (labelled C, D, E, F) have to be assumed to interpret the results. Examination of the magnitude and the θ dependence of the frequency of each of the observed lines permitted the assignments of Table I to be made. Details of these assignments are available in Ref. (16). In two different rotations the lines corresponding to the same site, and to the transition between the same pair of levels, could be identified since each pair of rotations has one orientation in common (e.g. $\theta_Z = 90°$ and $\theta_X = 0°$ both correspond to the Y axis

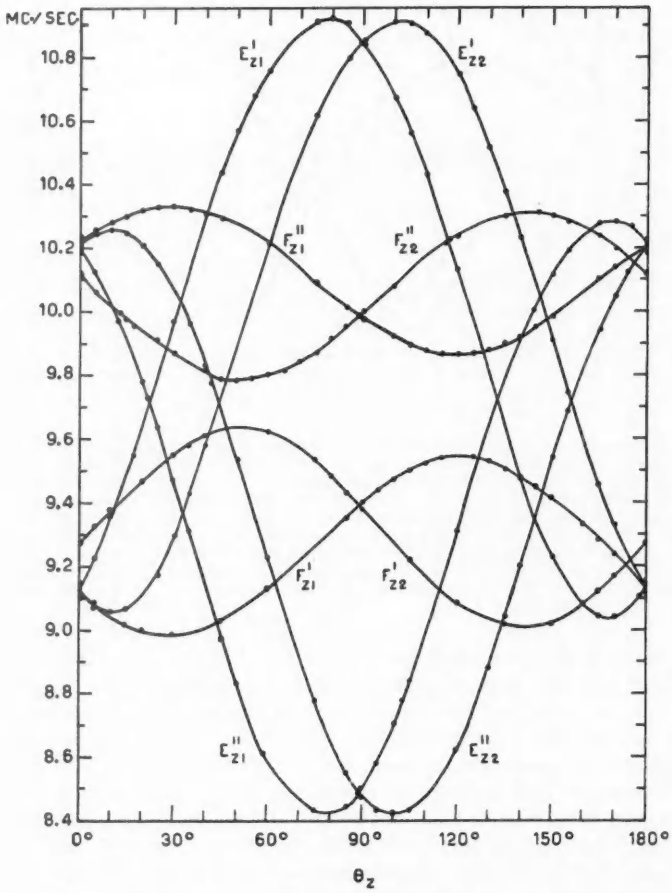


FIG. 3. Semiquantitative study of the dependence on the angular position of kernite sample II of the frequencies of the "satellites" at the E, F sites (cf. Table I) of the B^{11} spectrum for the Z rotation about the crystal c axis. $\theta_Z = 0°$ corresponds to the b symmetry axis of the crystal along H_0. The F_Z lines are split in some orientations but the splitting is too small to show up on the scale of this figure. The E_Z lines were not split.

lined up along H_0). To decide which of the two lines labelled C'_{Y1}, C'_{Y2} corresponds to the same site as a particular member of the pair C'_{Z1}, C'_{Z2} one has to examine quantitatively the data for the second order effect. In a similar way the assignment of which of the two "central" lines A, B belongs to the E and which belongs to the F site has to be made on the basis of a quantitative consideration of the second order effect. The lines A_{Z1}, A_{Z2} in Fig. 2 show some splitting with a maximum amount of about 8 kc./sec. while B_{Z1}, B_{Z2} show no such splitting. The same amount of splitting was present in the F_{Z1},

TABLE I

NOMENCLATURE OF LINES OBSERVED IN THE RESONANCE ABSORPTION SPECTRUM OF B^{11} IN KERNITE

(Lines which show additional small splitting for some crystal orientations are underlined)

Non-equivalent B^{11} sites		C	D	E	F
		"Small" field gradients		"Large" field gradients	
$\lvert eQ\phi_{zz}/h\rvert$, Mc./sec. } deduced from		0.645±.003	0.588±.003	2.563±.007	2.567±.010
$\eta \equiv (\phi_{xx}-\phi_{yy})/\phi_{zz}$ } spectrum		0.54 ±.01	0.60 ±.02	0.163±.010	.117±.010
Calc. pure quadrupole freq., Mc./sec.		0.338±.002	0.312±.003	1.286±.004	1.287±.003
Sites related by 180° rotation about symmetry axis		C_1 C_2	D_1 D_2	E_1 E_2	F_1 F_2

Axis	Transition	Line	Designation of observed lines							
X	$\pm 3/2 \leftrightarrow \pm 1/2$	ν'	C_X'		D_X'		$\underline{E_X}'$		F_X'	
	$+1/2 \leftrightarrow -1/2$	ν_c	$G_X \approx \nu_0$				$\underline{B_X}$		A_X	
	$\mp 3/2 \leftrightarrow \mp 1/2$	ν''	C_X''		D_X''		$\underline{E_X}''$		F_X''	
Y	$\pm 3/2 \leftrightarrow \pm 1/2$	ν'	C_{Y1}'	C_{Y2}'	D_{Y1}'	D_{Y2}'	$\underline{E_{Y1}}'$	$\underline{E_{Y2}}'$	F_{Y1}'	F_{Y2}'
	$+1/2 \leftrightarrow -1/2$	ν_c	$G_Y \approx \nu_0$				$\underline{B_{Y1}}$	$\underline{B_{Y2}}$	A_{Y1}	A_{Y2}
	$\mp 3/2 \leftrightarrow \mp 1/2$	ν''	C_{Y1}''	C_{Y2}''	D_{Y1}''	D_{Y2}''	$\underline{E_{Y1}}''$	$\underline{E_{Y2}}''$	F_{Y1}''	F_{Y2}''
Z	$\pm 3/2 \leftrightarrow \pm 1/2$	ν'	C_{Z1}'	C_{Z2}'	D_{Z1}'	D_{Z2}'	E_{Z1}'	E_{Z2}'	$\underline{F_{Z1}}'$	$\underline{F_{Z2}}'$
	$+1/2 \leftrightarrow -1/2$	ν_c	$G_Z \approx \nu_0$				B_{Z1}	B_{Z2}	$\underline{A_{Z1}}$	$\underline{A_{Z2}}$
	$\mp 3/2 \leftrightarrow \mp 1/2$	ν''	C_{Z1}''	C_{Z2}''	D_{Z1}''	D_{Z2}''	E_{Z1}''	E_{Z2}''	$\underline{F_{Z1}}''$	$\underline{F_{Z2}}''$

F_{Z2} lines, but it does not show up on the scale of Fig. 3. The lines E_{Z1}, E_{Z2} showed no such splitting. All the lines which showed some splitting are underlined in Table I.

After all the lines were properly identified by examination of such curves as those of Figs. 2 and 3, 36 special record charts were carefully prepared for the detailed quantitative analysis of the dependence of the line frequencies on θ. These corresponded to 12 crystal positions spaced by 30° in each of the three rotations, and were made with the final improved version of the crystal mount. The experimental values of $\nu'-\nu''$, $\frac{1}{2}(\nu'+\nu'')-\nu_0$, and $\nu_c-\nu_0$ from these charts were plotted as functions of θ over the interval of 0° to 180°. The theoretical curves of equations [1], [2] are expected to be periodic with a period of 180°. The experimental points at θ and $\theta+180°$ in each case differed very little and were averaged. Also whenever a line showed splitting the mean of the two frequencies was used. Such averaged points appear in the sample curves of Figs. 4, 5, 6. Curves of the form

$$[13] \qquad y = \sum_{n=0}^{5} C_n \cos n\theta + \sum_{n=1}^{6} S_n \sin n\theta$$

were then fitted to these experimental points by the 12-point analysis of Whittaker and Robinson (18). As expected theoretically from equations [1] and [2], the coefficients of all terms in equation [13] involving angles other than $0, 2\theta, 4\theta$ turned out to be zero within experimental error. The other coefficients, labelled in accordance with the notation of equations [1] and [2], are listed in Tables II, III. The solid curves in Figs. 4, 5, 6 represent such curves of the

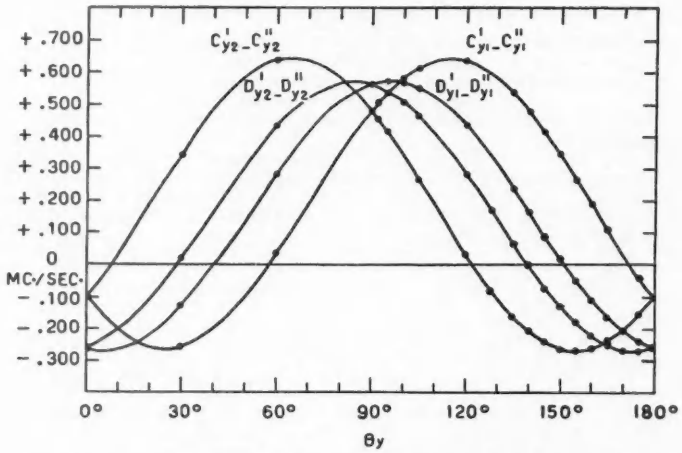


FIG. 4. Quantitative study of the dependence of the frequency difference $\nu'-\nu''$ between the "satellites" at the C and D sites (cf. Table I) of B^{11} in kernite sample Ic on the angular position in the Y rotation (about an axis perpendicular to the crystal b and c axes). $\theta_Y = 0°$ corresponds to the b symmetry axis of the crystal perpendicular to H_0. The solid lines are curves of the theoretically expected form fitted to points spaced every 30°. A few additional experimental points are plotted to show how well they fall on the curves.

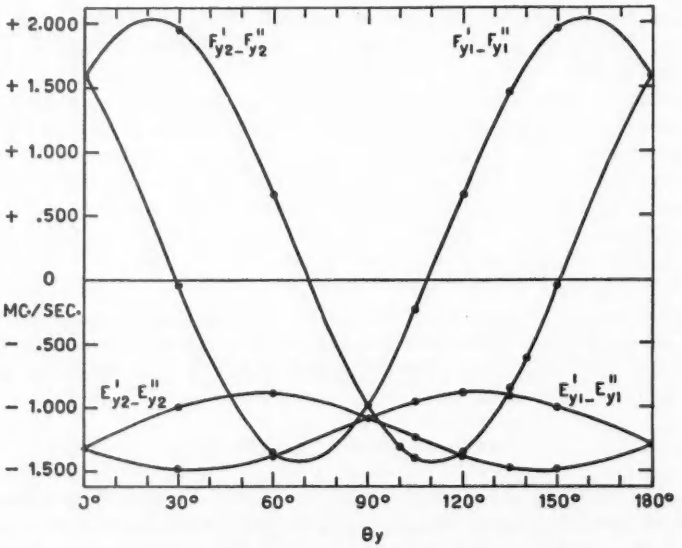


FIG. 5. Quantitative study of the dependence of the frequency difference $\nu'-\nu''$ between the "satellites" at the E and F sites (cf. Table I) of B^{11} in kernite sample Ic on the angular position in the Y rotation (about an axis perpendicular to the crystal b and c axes). $\theta_Y = 0°$ corresponds to the b symmetry axis of the crystal perpendicular to H_0. The solid lines are curves of the theoretically expected form fitted to points spaced every 30°. A few additional experimental points are plotted to show how well they fall on the curves.

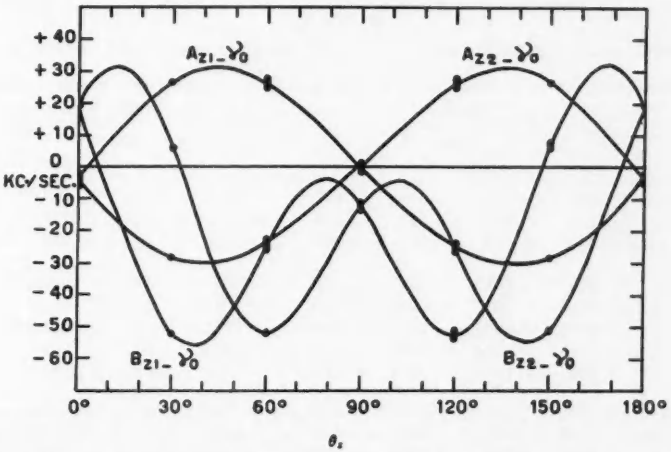


FIG. 6. Quantitative study of the dependence of the frequency shift $\nu_c - \nu_0$ of the "central" lines A_{Z1}, A_{Z2}, B_{Z1}, B_{Z2} at the F and E sites (cf. Table I) in kernite sample IV on the angular position in the Z rotation (about the c crystal axis). $\theta_Z = 0°$ corresponds to the b symmetry axis along H_0. The solid lines are curves of the theoretically expected form fitted to experimental points spaced every 30°. These curves represent information similar to that of Fig. 2, except that the frequencies of the split A_Z lines have been averaged. The size of the marks denoting the experimental points represents the estimated accuracy of the frequency determination.

TABLE II

EXPERIMENTAL VALUES OF FOURIER COEFFICIENTS (IN MC./SEC.) FOR B^{11} AT SITES C AND D (CF. EQUATIONS [1], [2])

		First order coefficients			Second order coefficients				
Site	Curve	a	b	c	$\bar{n}$	$\bar{p}$	$\bar{r}$	$\bar{u}$	$\bar{v}$
C	X	−.2389	−.1384	−.1271	.0027	−.001	.0009		
	$Y_{1,2}$	.1889	−.2916	∓.3483	.0022		±.0005	.0005	∓.0023
	Z_1	.0523	.4285	.1135	.0030	.0005	−.0007	−.0014	−.0012
	Z_2	.0519	.4280	−.1174	.0030	.0005	.0005	−.0016	.0009
D	X	−.2816	−.0190	.1644	.0018		−.0003		
	$Y_{1,2}$	.1519	−.4114	±.0864	.0016		∓.0005	−.0017	±.0007
	Z_1	.1311	.4325	.1321	.0018			−.0012	−.0014
	Z_2	.1304	.4327	−.1358	.0019			−.0015	.0014

Experimental errors are about 0.0008 Mc./sec. for the first order coefficients a, b, c, and about 0.0004 Mc./sec. for the second order coefficients $\bar{n}$, $\bar{p}$, $\bar{r}$, $\bar{u}$, $\bar{v}$. Those second order coefficients for which no values are given were less than 0.0003.

form of equations [1], [2] fitted to the six points spaced by 30°. In Figs. 4, 5 points corresponding to a few additional crystal positions are plotted to show how closely they fall on the curves fitted to the points spaced by 30°. In the Y rotation the crystal alignment was sufficiently good that the curves corresponding to the boron sites related by a 180° rotation were very symmetrical with respect to the $\theta_Y = 0°$, 90°, 180° points, so that the points at θ_Y and $180° - \theta_Y$ coincided very closely. These points were averaged and only one set

TABLE III

EXPERIMENTAL VALUES OF FOURIER COEFFICIENTS (IN MC./SEC.) FOR B^{11} AT SITES E AND F (CF. EQUATIONS [1], [2])

		Site E				Site F			
		Curve				Curve			
		X	$Y_{1,2}$	Z_1	Z_2	X	$Y_{1,2}$	Z_1	Z_2
$\nu'-\nu''$	a	.538	−1.186	.647	.647	.488	.307	.799	.802
	b	1.838	−.108	−1.722	−1.730	−1.124	1.288	.178	.179
	c	.304	∓.278	.741	−.725	−1.153	∓1.160	.486	−.485
$\bar{\nu}-\nu_0$	$\bar{n}$	.0365	.0063	.0321	.0321	.0373	.0400	.0260	.0260
	$\bar{p}$	−.0039	−.0036	−.0006	−.0006	−.0105	.0100	0	−.0003
	$\bar{r}$	.0036	∓.0041	.0018	−.0016	−.0102	∓.0103	−.0239	.0238
	$\bar{u}$	−.0284	.0004	−.0210	−.0213	.0005	−.0030	.0017	.0017
	$\bar{v}$	−.0097	∓.0003	.0218	−.0216	−.0223	±.0255	−.0013	.0012
$\nu_c-\nu_0$	n	−.0224	No	−.0193	−.0193	−.0214	−.0279	−.0009	−.0007
	p	−.0194	curve	.0155	.0154	.0224	−.0201	−.0017	−.0020
	r	−.0072	fitted	−.0088	.0088	.0221	±.0192	.0305	−.0303
	u	.0315		.0231	.0230	−.0012	.0034	−.0011	−.0015
	v	.0109		.0251	.0240	.0255	∓.0289	.0012	−.0015

Experimental errors are about 0.002 Mc./sec. for the first order coefficients a, b, c, and about 0.0004 Mc./sec. for the second order coefficients n, p, r, u, v.

of curves was obtained. The curves at the two sites are mirror images of each other, and differ only in the sign of the c, r, v coefficients. In the Z rotation the crystal alignment was not quite as good, so that separate curves were fitted to the lines arising from the two positions related by a 180° rotation. For the Z rotation the coefficients at the two sites related by a rotation differ not only in sign but also slightly in magnitude.

For the C and D sites the second order effect is so small that the $\nu_c-\nu_0$ curves were not plotted at all, and the $\frac{1}{2}(\nu'+\nu'')-\nu_0$ curves gave only very small coefficients in Table II, just outside the experimental error. That the observed order of magnitude of these coefficients is correct was checked by substituting the experimental values of a, b, c into equation [3]. The only use made of these second order coefficients is their sign, which enables one to determine with the aid of equation [3] which curves in the Y and Z rotations belong to the same sites (e.g. which of the two $C_Y'-C_Y''$ curves belongs to the same site as $C_{Z1}'-C_{Z1}''$ and which to $C_{Z2}'-C_{Z2}''$). No use is made of the numerical magnitudes of these second order coefficients, other than to increase our confidence in the correctness of their sign. Only the a, b, c coefficients of Table II are used to determine the components of $\psi_{ij} \equiv eQ\phi_{ij}/h$ in the X, Y, Z system in Table IV. When diagonalized these lead to $|C_z| \equiv |eQ\phi_{zz}/h|$ and η listed in Table I, and direction cosines listed in Table VI.

Table V for the E and F sites contains more ψ_{ij} entries, because the second order coefficients were large enough to use in the evaluation of ψ_{ij}. Because the components of ψ_{ij} derived from different rotations are not quite compatible

TABLE IV

COMPONENTS OF THE TENSOR $\psi_{ij} \equiv eQ\phi_{ij}/h$ IN X, Y, Z COORDINATES AT SITES C AND D (IN MC./SEC.)

Site	Component	X rotation	Y rotation	Z rotation	Average
$C_{1,2}$	ψ_{XX}	.4780	.4805	.4803	.4799
	ψ_{YY}	−.3774	−.3778	−.3761	−.3770
	ψ_{ZZ}	−.1007	−.1027	−.1042	−.1026
	ψ_{XY}			∓.1155	∓.1155
	ψ_{YZ}	.1271			.1271
	ψ_{ZX}		±.3483		±.3483
$D_{1,2}$	ψ_{XX}	.5632	.5633	.5634	.5633
	ψ_{YY}	−.3006	−.3038	−.3018	−.3021
	ψ_{ZZ}	−.2626	−.2595	−.2616	−.2612
	ψ_{XY}			∓.1339	∓.1339
	ψ_{YZ}	−.1644			−.1644
	ψ_{ZX}		∓.0864		∓.0864

Experimental errors are about 0.001 Mc./sec. in the values in the three rotations. An error of 0.002 Mc./sec. is assumed for the average to take into account misalignment of the crystal.

TABLE V

COMPONENTS OF THE TENSOR $\psi_{ij} \equiv eQ\phi_{ij}/h$ IN X, Y, Z COORDINATES AT SITES E AND F (IN MC./SEC.)

				Z rotation	
Site	Component	X rotation	Y rotation	Z_1 curves	Z_2 curves
$E_{1,2}$	ψ_{XX}	−1.077±.002	−1.078±.001	−1.075±.002	−1.082±.002
	ψ_{YY}	2.377±.002	2.372±.001	2.369±.002	2.377±.002
	ψ_{ZZ}	−1.300±.002	−1.294±.001	−1.294±.002	−1.296±.002
	ψ_{XY}	∓(0.730±.010)	±(0.726±.010)	−0.741±.001	0.725±.002
	ψ_{YZ}	−0.304±.002	−0.33 ±.02	−0.37 ±.03	−0.37 ±.03
	ψ_{ZX}	±(0.28 ±.03)	±(0.278±.001)	0.27 ±.03	−0.25 ±.03
$F_{1,2}$	ψ_{XX}	−0.975±.001	−0.980±.002	−0.976±.001	−0.981±.001
	ψ_{YY}	−0.637±.001	−0.615±.002	−0.621±.001	−0.622±.001
	ψ_{ZZ}	1.612±.001	1.595±.001	1.597±.001	1.603±.002
	ψ_{XY}	±(0.49 ±.02)	±(0.49 ±.02)	0.485±.001	−0.485±.002
	ψ_{YZ}	1.153±.001	1.189±.008	1.179±.010	1.180±.010
	ψ_{ZX}	±(1.209±.010)	±(1.160±.001)	1.172±.010	−1.169±.010

owing to a slight misalignment of the crystal it was felt that it would be more accurate to diagonalize the tensors as determined from each set of curves individually, rather than to combine the best values of the components of ψ_{ij} from each set.

Diagonalization of the tensors in the E sites gives for the quadrupole coupling constant $|C_z| = 2.558\pm.008$, $2.556\pm.006$, $2.569\pm.008$, $2.568\pm.006$ Mc./sec., and for the asymmetry parameter $\eta = 0.174\pm.010$, $0.166\pm.010$, $0.155\pm.010$, $0.144\pm.020$ from the E_X, E_Y, E_{Z1}, E_{Z2} curves respectively. Similarly for the F sites, the curves F_X, F_Y, F_{Z1}, F_{Z2} respectively give the values $|C_z| = 2.577\pm.020$, $2.561\pm.010$, $2.564\pm.010$, $2.568\pm.008$ Mc./sec.

for the quadrupole coupling constant, and the values $\eta = 0.120 \pm .020$, $0.114 \pm .010$, $0.118 \pm .010$, $0.119 \pm .010$ for the asymmetry parameter. The weighted averages of these values are listed in Table I.

The values of the direction cosines of the principal axes of the ϕ_{ij} tensors with respect to the X, Y, Z axes (averaged over results from the three rotations) are given in Table VI. The actual agreement between the values de-

TABLE VI

DIRECTION COSINES OF THE FIELD GRADIENT TENSOR PRINCIPAL AXES (x, y, z) WITH RESPECT TO CRYSTAL AXES X, Y, Z AT B^{11} SITES C, D, E, AND F

Site	Axis	x	y	z
$C_{1,2}$	X	$-.31 \pm.01$	$+.28 \pm.01$	$-.909 \pm.008$
	Y	$\pm(.58 \pm.01)$	$\pm(.81 \pm.01)$	$\pm(.051 \pm.005)$
	Z	$\pm(.75 \pm.01)$	$\mp(.51 \pm.02)$	$\mp(.41 \pm.01)$
$D_{1,2}$	X	$-.032 \pm.003$	$-.151 \pm.007$	$.98 \pm.03$
	Y	$\mp(.65 \pm.01)$	$\mp(.75 \pm.01)$	$\mp(.13 \pm.02)$
	Z	$\pm(.81 \pm.02)$	$\mp(.61 \pm.01)$	$\mp(.07 \pm.05)$
$E_{1,2}$	X	$-.76 \pm.04$	$-.60 \pm.03$	$-.21 \pm.01$
	Y	$\mp(.22 \pm.03)$	$\mp(.05 \pm.01)$	$\mp(.97 \pm.02)$
	Z	$\mp(.60 \pm.07)$	$\pm(.79 \pm.07)$	$\mp(.10 \pm.01)$
$F_{1,2}$	X	$-.05 \pm.03$	$-.94 \pm.04$	$.340 \pm.005$
	Y	$\pm(.92 \pm.04)$	$\pm(.09 \pm.03)$	$\pm(.368 \pm.005)$
	Z	$\mp(.37 \pm.02)$	$\pm(.33 \pm.02)$	$\pm(.865 \pm.001)$

termined from the Fourier coefficients obtained in different rotations was considerably better than the quoted experimental errors which were computed on the basis of the estimated accuracy in the measured Fourier coefficients.

A quantity which can be found directly from the experimental values of the constant term in the equations for the $\frac{1}{2}(\nu'+\nu'')$ and ν_c curves is ν_0+n. The coefficient n is small with respect to ν_0 so that if n is calculated using equation [3] in terms of a, b, c, and an approximate value of ν_0 (which was taken as the observed frequency of the G lines), then an accurate value of ν_0 is obtained.

Such calculations carried out on all possible central line curves and shifts of center of gravity of the satellites show no difference in ν_0 within experimental error between the various nuclear sites, but do indicate a small difference between the value of ν_0 for the X rotation and that for the Y and Z rotations. The average value of ν_0 for the X rotation determined from six different curves is $9.6624 \pm .0005$ Mc./sec. whereas that for the Y and Z rotations determined from 16 curves is $9.6616 \pm .0005$ Mc./sec. The errors quoted are just large enough to include the worst measurements in each case.

These results indicate that there appeared to be a decrease in H_0 of about 0.008% between times of carrying out the X rotation and the Y and Z rotations. The X rotation was done about three months before the Y and Z rotations, which were done about a month apart, so that this seems quite possible.

The lines E'_X, E''_X, B_X, E'_{Y1}, E''_{Y1}, B_{Y1}, E'_{Y2}, E''_{Y2}, B_{Y2}, and F'_{Z1}, F''_{Z1}, A_{Z1}, F'_{Z2}, F''_{Z2}, A_{Z2} are split over a part of their respective rotations by an amount up to

about 11 kc./sec. The order of magnitude of the splitting in the Z rotation is illustrated by Fig. 2 in which the lines A_{z1}, A_{z2} (among others) are plotted against angle of rotation of the crystal. The splitting in the X rotation covers approximately the region $\theta_X = 75°$ to $\theta_X = 115°$.

In order to throw some light on the possible cause of this splitting the line B_X was studied as a function of field strength using the nuclear magnetic resonance spectrometer described in Ref. (14). Since this spectrometer used a proton stabilized electromagnet to produce the static field H_0 it was easy to obtain different values. The splitting of the line B_X at the position $\theta_X = 84°$ (near maximum splitting) was observed at fields of 6260, 5006, and 3794 gauss. The observed lines are shown in Table VII where $B_X(1)$ and $B_X(2)$ are the two components of B_X, and the frequencies are expressed in Mc./sec.

Since G_X approximates the unperturbed Larmor frequency (within about 2 kc./sec.), the constancy of the entries in the last column in Table VII shows that the shift of the center of gravity of the split center line B_X from the Larmor frequency ν_0 varies inversely with the magnetic field H_0, as predicted for $\nu_c - \nu_0$ by equations [2] and [5]. However, the additional splitting of the curve B_X (i.e. $B_X(2) - B_X(1)$) is independent of the external field H_0 within the experimental error in this region of magnetic field, and is thus apparently connected with some interaction within the crystal.

No detailed study of the Na^{23} lines has been made but the following observations are recorded. In the X rotation two central Na^{23} lines were seen both of which have the angular dependence of the form of equations [2] and neither of which shows additional splitting. No line without angular dependence was observed in the neighborhood of ν_0 for Na^{23}. When the central lines were observed at several crystal orientations in which the X (symmetry) axis was neither parallel nor perpendicular to the magnetic field, four lines were seen, none of which showed additional splitting.

5. DISCUSSION

This experiment has shown that the second order theory of the perturbation of the nuclear Zeeman energy levels by the interaction of the nuclear electric quadrupole moment with the crystalline electrostatic field gradient helps one to sort out the lines, and is adequate to explain the major features of the complex resonance absorption spectrum due to several non-equivalent B^{11}

TABLE VII

ADDITIONAL SPLITTING OF B_X AT $\theta_X = 84°$ AND AT DIFFERENT VALUES OF H_0
(Frequencies are expressed in Mc./sec., H_0 is in gauss)

H_0	Proton frequency	G_X	$B_X(1)$	$B_X(2)$	$B_X(2)-B_X(1)$	$\frac{B_X(1)+B_X(2)}{2}-G_X$	$\left[\frac{B_X(1)+B_X(2)}{2}-G_X\right]H_0$
6260	26.65	8.5577	8.5724	8.5805	0.0081	0.0187	117
5006	21.31	6.8872	6.9060	6.9140	0.0080	0.0228	114
3794	16.15	5.1864	5.2137	5.2214	0.0077	0.0311	118

Experimental error of the frequency measurements is about 0.0007 Mc./sec. H_0 is calculated from the proton frequency.

nuclei in a single crystal of kernite (none of which are on axes of symmetry and all of which are subject to axially asymmetric field gradients). Except for a small additional splitting in some crystal orientations, the observed 21-line spectrum is the superposition of the "simple" three-line spectra for each of the eight non-equivalent B^{11} positions in the unit cell. In addition, the present experiment has confirmed the fact that if only first order electric quadrupole effects are measurable in the spectrum three rotations are necessary to determine the quadrupole coupling tensor at a nuclear site, whereas if measurable second order effects are present one rotation determines the tensor except for an arbitrary sign corresponding to a rotation of the tensor through 180° about the rotation axis.

It may be noted from Table V that for each rotation the two components of the tensors at the *E* and *F* sites which are determined from the second order effect have much larger experimental errors than those four components which are determined from the first order effect. The quadrupole coupling constant, the asymmetry parameter, and the orientation of the electric field gradient tensor were determined separately for each rotation using the four accurate and the two less accurate tensor components. The errors in such a determination of these quantities are due largely to the two less accurate components. The accurate components from two different rotations were not combined because of slight misalignments of the rotation axes. These errors perhaps could have been reduced somewhat by using the symmetry of the crystal to tell what the misalignment was so that the best values from each rotation could be combined.

The nuclear magnetic resonance spectrum of B^{11} in kernite is consistent with the crystal symmetry and number of boron atoms per unit cell proposed on the basis of X-ray studies (11, 7) but can not at present supply any information concerning the positions of the boron atoms. In the proposed structure the boron atoms occur in BO_3 triangles sharing O vertices to form B_3O_6 rings, and B_2O_3 groups joining these rings into chains. The basic unit is a B_4O_7 group three of whose borons are in a B_3O_6 ring and one is in a B_2O_3 group. This B_4O_7 is repeated four times in a unit cell by reflection in either one of two symmetry centers, one of which is coincident with the middle oxygen of the B_2O_3 group and the other with the oxygen common to two B_3O_6 rings, followed by rotation about a symmetry axis. In such a structure the four essentially non-equivalent boron sites inferred from the nuclear resonance spectrum must coincide with the four borons in the basic B_4O_7 unit. Examination of a three-dimensional model of this proposed kernite structure showed no obvious correlations between any of the BO directions and any of the principal axes of the ϕ_{ij} tensors obtained from the spectrum. It is thus not possible at present to assign the four quadrupole coupling tensors obtained in this experiment to particular boron positions in the B_4O_7 group.

It should be noted that this experiment determined the existence of a symmetry axis independently of any previous knowledge from X-ray spectra. The fact that one of the rotation axes was the symmetry axis of the crystal

was made obvious by looking at the form of the curves like those of Figs. 2–5. However, even if the symmetry axis did not happen to be picked as a rotation axis the numerical analysis would have revealed its existence, and determined its direction. This experiment can not tell the difference between two nuclear sites which can be obtained from each other by inversion, and so gives no information about the existence of symmetry centers.

The preliminary results on the Na^{23} spectrum lead to a direct contradiction of the proposal made on the basis of X-ray studies (11, 7) that there are three essentially non-equivalent sodium sites, two of these being on axes of symmetry and each containing one quarter of all the Na atoms, while the other half of the Na atoms lie in two sites related by a 180° rotation about the symmetry axis. The presence of only two central lines in the X rotation (symmetry axis perpendicular to H_0) shows that there are at most two essentially non-equivalent sodium atoms in the unit cell. The presence of four central lines due to Na^{23} when the symmetry axis is not perpendicular to the magnetic field H_0 shows that neither of these two essentially different positions for the sodium atoms is on an axis of symmetry.

The situation in this crystal might be compared with that found by Dehmelt (4) in the molecular solids $B(CH_3)_3$ and $B(C_2H_5)_3$. In these compounds, in which the bonds are about 25% ionic, he found that $|C_z| \approx 4.9$ Mc./sec. Since the electronegativity difference between boron and oxygen (=1.5) is considerably larger than that between boron and carbon (=0.5) it is expected that the boron–oxygen bonds are considerably more ionic in character (9) and hence that the electric field gradient at the boron nucleus is considerably weaker. This is consistent with the fact that boron–oxygen bonds probably exist in kernite and that smaller quadrupole coupling constants were observed.

The pure quadrupole resonance frequencies of the B^{11} at all four sites in kernite have been calculated using formulae given by Krüger (6) and are given in Table I. The two values at the E and F sites are not significantly different, so that only one line may be expected at $H_0 = 0$ in the pure quadrupole spectrum due to B^{11} in this region. The pure quadrupole signal has been found at 1.270±.015 Mc./sec. with a superregenerative detector by Cranna (2, 3) and has been measured with greater accuracy using a Bloch apparatus at 1.279±.001 Mc./sec. by Kiddle and Proctor (5). The figures in Table I for the predicted pure quadrupole frequency are averages of the determinations from four different sets of curves so that the difference between the observed and the predicted pure quadrupole frequency appears to be significant.

The cause of the additional splitting of some of the B^{11} resonance lines has not been definitely established in this experiment. The splitting appears to be independent of the external field H_0, and in order of magnitude is consistent with the splitting due to dipole–dipole interaction. Neither the sodium lines, which have been observed in detail throughout the X rotation, nor the proton signal, which was observed by Blood and Proctor (1) for one crystal orientation, showed any splitting, so that the splitting of the B^{11} lines is not likely

to be caused by dipole–dipole interaction of the B^{11} nucleus with neighboring Na^{23} nuclei or protons. This leaves the possibility of close B^{11} nuclei interacting with each other.

The effect of a dipole–dipole interaction may be expressed as $(\mu_1\mu_2/a^3h)f(\gamma)$ where μ_1, μ_2 are the magnitudes of two dipoles at a distance a apart. $f(\gamma)$ is a function which depends on the angle γ between the line of length a joining the two dipoles and the axis of quantization, and which is of order unity. Pake (8) has shown that for two protons ($I = \frac{1}{2}$), $f(\gamma) = 6(3\cos^2\gamma - 1)$. A similar computation for $I = 3/2$ shows that several lines may appear, the largest splitting being given by $2(3\cos^2\gamma - 1)$. Using the value $\mu = 2.689$ nuclear magnetons for the magnetic moment of B^{11} and the observed maximum splitting $\Delta\nu = 11$ kc./sec. one obtains $a = 2.4$ Å which is approximately equal to the distance between boron nuclei in a B_3O_6 ring (9). The observed large and variable width of the B^{11} lines may at least in part be due to the other unresolved components produced by dipole–dipole interaction of B^{11} nuclei of spin $I = 3/2$.

The results of this experiment indicate some interesting lines for future investigation which are listed below.

1. The reason for the deviation of the observed pure quadrupole line at 1.279 Mc./sec. from the frequency predicted on the basis of the high field measurements is not apparent. Dr. J. M. Daniels has suggested that a possible cause may be an asymmetric shielding of the nucleus by its surroundings. If such a shielding took the form of a second rank tensor, as in Ref. (12), its effects could only be separated from the electric quadrupole interaction by studying the spectrum at several considerably different values of the magnetic field.

2. The cause of the observed small additional line splitting is not definitely established and further investigation of it would be of interest. Observations on the splitting were hampered by limited resolution, large line widths, and the presence of many other lines. It is desirable for best resolution to study the central components in detail because of the large line widths of the satellites. This was difficult in this experiment because of the number of lines present. However if a smaller value of H_0 was used, the central components would be separated more because the second order electric quadrupole interaction varies inversely with H_0. Consideration of the B^{10} spectrum in kernite as well as more data on the splitting in the B^{11} case would be worth while. If the splitting is due to the interaction of neighboring magnetic dipoles it should be very small in the case of B^{10} because of its small magnetic moment (1.8 nuclear magnetons).

A successful analysis of such dipole–dipole splitting would yield the length and the orientation relative to the crystal axes of the line joining the interacting B^{11} nuclei, which could then be checked against the B^{11} positions proposed on the basis of X-ray data.

3. The spectrum of B^{10} was not searched for at all in this experiment. In spite of the fact that its intensity will be much less than that of the B^{11} spectrum owing to the smaller gyromagnetic ratio and the lower abundance, at

least the inner satellites should be visible. Their investigation would indicate whether high magnetic field measurements give the same value of the ratio of the quadrupole moments of B^{11} and B^{10} as zero magnetic field measurement for this ratio made by Dehmelt (4).

4. Using the ratio of frequencies seen by Dehmelt (4) and the pure quadrupole frequency seen in kernite, a pure quadrupole line, due to the B^{10} nuclei, should appear at 1.333 Mc./sec. If this line were found it would give another check on the ratio of the quadrupole moments of B^{10} and B^{11}.

5. Two other sodium borates, namely tincalconite ($Na_2B_4O_7.5H_2O$) and borax ($Na_2B_4O_7.10H_2O$), exist in crystals of convenient size. Few data are reported about these crystals in the literature so that comparison of the Na^{23} and B^{11} spectra in these crystals with those in kernite might yield useful information concerning their structures.

6. ACKNOWLEDGMENTS

The authors would like to thank Dr. W. G. Proctor of the University of Washington for several valuable discussions of this subject, for information on magnet design, and for communicating to us in advance of publication the results obtained by himself, H. Blood, and R. Kiddle on the high and zero field spectra of B^{11}, Na^{23}, and H^1 in kernite. Our thanks are also due to Dr. R. M. Thompson of the Geology Dept., University of British Columbia, for providing some kernite crystals, and identifying their axes; to Dr. R. G. Eades for sharing in construction of some of the equipment, and for useful discussions; and to members of the Physics Department shop staff: Mr. A. J. Fraser, Mr. J. Lees, Mr. E. Price, and Mr. W. Morrison for their help with the apparatus. This work was made possible by continuing financial support from the National Research Council, which is gratefully acknowledged. One of us (H.H.W.) is indebted to the Defence Research Board for financial assistance while on study leave.

REFERENCES

1. Blood, H. and Proctor, W. G. Private communication.
2. Cranna, N. G. Ph.D. Thesis, University of British Columbia, Vancouver, B.C. 1954.
3. Cranna, N. G. and Waterman, H. H. Abstract 79, Roy. Soc. Can., Meeting Programme, June 1954.
4. Dehmelt, H. G. Z. Physik, 133: 528. 1952; 134: 642. 1953.
5. Kiddle, R. and Proctor, W. G. Private communication.
6. Krüger, H. Z. Physik, 130: 371. 1952.
7. Minder, W. Z. Krist. Abt. A, 92: 301. 1935.
8. Pake, G. E. J. Chem. Phys. 16: 327. 1948.
9. Pauling, L. Nature of the chemical bond. Cornell University Press, Ithaca, N.Y. 1948.
10. Petch, H. E., Cranna, N. G., and Volkoff, G. M. Can. J. Phys. 31: 837. 1953.
11. Portoles, L. Estud. geol. Inst. Mallada, 5: 3. 1947; 7: 21. 1948.
12. Ramsey, N. F. Phys. Rev. 86: 243. 1952.
13. Volkoff, G. M. Can. J. Phys. 31: 820. 1953.
14. Volkoff, G. M., Petch, H. E., and Smellie, D. Can. J. Phys. 30: 270. 1952.
15. Waterman, H. H. Phys. Rev. 96: 862. 1954.
16. Waterman, H. H. Ph.D. Thesis, University of British Columbia, Vancouver, B.C. 1954.
17. Watkins, G. D. Ph.D. Thesis, Harvard University, Cambridge, Mass. 1952.
18. Whittaker, E. and Robinson, G. The calculus of observations. Blackie & Son Ltd., London. 1948.

FORWARD-SCATTERING OF RADIO WAVES BY METEOR TRAILS[1]

By P. A. Forsyth and E. L. Vogan

ABSTRACT

Radio waves which are too high in frequency to be reflected by the ionospheric layers are often reflected back to the earth's surface by the ionization in meteor trails, and may be detected at distances of the order of 1000 kilometers from the transmitting station. These forward-scattered signals have been studied by the use of several transmission paths in Canada. The paper summarizes the characteristics of the individual signals and presents some preliminary results of the investigation. It seems likely that the technique will prove to be useful in meteoric studies.

INTRODUCTION

The recent work at Stanford University has stimulated a renewed interest in the forward-scattering of radio waves by meteor trails. The term forward-scattering is intended to indicate that the reflected signal from the meteor trail is received at a distance of several hundred kilometers from the transmitter, as distinct from the case of back-scattering where transmitter and receiver are at the same location. In a series of articles (6, 14, 15), the Stanford workers have outlined a theory of forward-scattering and presented some experimental evidence in its support. They have suggested that meteoric signals, received at a distance of several hundred kilometers from a very high frequency transmitter, might be sufficiently numerous to support continuous communication. McKinley has used data from his back-scatter measurements to arrive at even more favorable predictions concerning the utility of the forward-scattered signals (13).

The long-range propagation of very high frequency radio waves has been the subject of various investigations during the last quarter century. It is evident that at least some of these have included observations of the forward-scattered signals from meteor trails (see, for example, References 2, 4). One of the more recent of such investigations, that of Bailey *et al.* (1), not only confirmed the existence of the meteoric signals but demonstrated a suitable technique for their observation. The present meteoric program at the Radio Physics Laboratory grew out of an interest in the general subject of ionospheric scattering and much of the experimental technique is similar to that used by Bailey *et al.* For the past two years, the program has included a specific study of the forward-scattered signals from meteor trails. This paper presents briefly some typical results from this study and discusses the more striking characteristics of the forward-scattered meteor signal. While the results presented are neither comprehensive nor detailed, it would appear that similar studies may well provide new information concerning meteoric occurrence and meteoric ionization.

[1]*Manuscript received February 9, 1955.*
Contribution from the Radio Physics Laboratory of the Defence Research Board, Ottawa, Canada. Work carried out under Project No. 5512, PCC D48-28-35-05.

EXPERIMENTAL TECHNIQUE

The apparatus employed to study the forward-scattered meteor signals consists simply of transmitter, receiver, and recording equipment. The transmitting and receiving antennas are made directive and oriented so that their beams intersect at a height of about 100 kilometers near the mid-point of the path. The transmitter emits an unmodulated carrier continuously, except for short silent periods at regular intervals which serve both to identify the signals and to permit the recording of the background noise level. The receiver is a commercial communications receiver operated with a bandwidth of 1.3 kc./s. The noise figure of the receiving apparatus is always such that the limiting sensitivity of the system is fixed by the cosmic noise received by the antenna. At frequencies near 50 Mc./s. it is necessary to interpose a low-noise preamplifier between the antenna and receiver in order to ensure an adequate noise figure, whereas at lower frequencies no preamplifier is necessary. The automatic volume control circuit of the receiver is modified to provide an output voltage which is very nearly proportional to the logarithm of the input signal. This voltage is amplified and recorded on a moving chart recorder. The recording time constant for most of the routine records is about one second, although integration of the signal over periods as long as 64 sec. has been used for particular purposes. The response time of the various equipments used to investigate individual signals varies between 0.1 and 0.01 sec.

The transmission circuits which have been used for meteoric studies are listed in Table I. This table gives the relevant parameters for each of the circuits including the nominal value of the radiated power and the total antenna gain (the product of the receiving and transmitting antenna gains). Horizontal polarization is used on all the transmission circuits. With the exception of the first, the circuits listed were installed specifically for meteoric studies. The high power transmitter at Cedar Rapids (1) is beamed toward Stirling, West Virginia, but fortunately a significant amount of energy, associated with a side lobe of the radiation pattern, is directed toward Ottawa. This signal has been recorded continuously at Ottawa since early in 1952. It is not possible to deduce directly the absolute sensitivity of the Cedar Rapids – Ottawa circuit because of the uncertainty concerning the power radiated toward Ottawa. The figures given in Table I were arrived at by comparison of the signal records with those from other circuits.

Typical signal records for circuits 3, 4, 5, and 6 are shown in Fig. 1. The breaks in the records indicate the silent periods mentioned earlier, which occur once per hour on circuits 5 and 6 and once every two hours on circuits 3 and 4. The records show the very large number of meteoric signals which are observed. Each spike on the record represents the signal scattered from a meteor trail. The vertical scale, which indicates the amplitude of the signal, is very nearly logarithmic. For circuits 3 and 4 and again for circuits 5 and 6, it is possible to identify and compare the signals scattered at two frequencies from the same meteoric trail.

TABLE I

TRANSMISSION CIRCUITS USED FOR METEORIC STUDIES

Circuit No.	Transmitter location	Receiver location	Path			Frequency, Mc./s.	Power, kw.	Total antenna gain
			Length, km.	Mid-point	Bearing			
1	Cedar Rapids, Iowa	Ottawa	1348	43.7°N. 83.9°W.	074°	49.80	1.0*	30*
2	Ottawa	Halifax, N.S.	944	45.0°N. 69.6°W.	086°	49.00	0.9	100
3	Halifax	Ottawa	—	—	274°	49.98	0.1	100
4	Halifax	Ottawa	—	—	—	39.22	0.1	100
5	Winnipeg, Man.	Ralston, Alta.	991	50.0°N. 104.2°W.	272°	49.98	0.5	400
6	Winnipeg	Ralston	—	—	—	38.06	0.5	200
7	Winnipeg	Churchill, Man.	1014	54.3°N. 95.7°W.	011°	49.98	0.5	400
8	Winnipeg	Churchill	—	—	—	38.06	0.5	200

**Estimated "effective" values as discussed in text.*

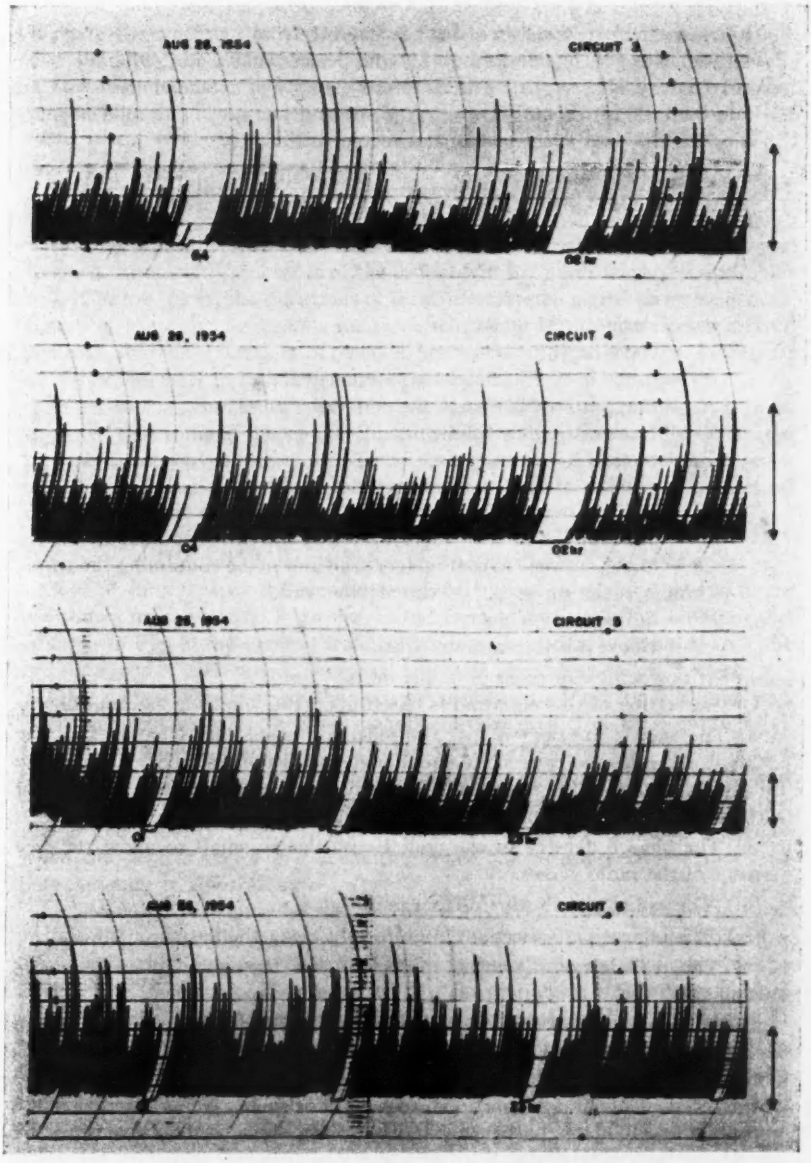


FIG. 1. Examples of routine records made at Ottawa and Ralston. The vertical scales are logarithmic and each arrow represents a recording range of 20 db.

THE THEORY OF FORWARD-SCATTERING

The theoretical treatments of back-scattering from meteor trails given by Lovell and Clegg (11), Herlofson (8), and Kaiser and Closs (9) have been summarized by Kaiser (10). The Stanford group has extended this work to include the case of forward-scattering (5, 6) and has given the following expression for the power received from a meteor trail:

$$[1] \qquad P_R = \frac{P_T}{32\pi^4}\left(\frac{\mu_0 e^2}{4m}\right)^2 \frac{2\lambda^3}{R_1 R_2 (R_1+R_2)} \frac{G_T G_R q^2 \sin^2\alpha}{1-\cos^2\beta \sin^2\phi} \exp\left(\frac{-32\pi^2 D t}{\lambda^2 \sec^2\phi}\right)$$

where P_T = transmitted power,
μ_0 = permeability of free space,
e = electronic charge,
m = electron rest mass,
λ = wavelength,
R_1 = range from transmitter to meteor trail,
R_2 = range from receiver to meteor trail,
G_T = transmitting antenna gain,
G_R = receiving antenna gain,
q = number of electrons per meter of trail length,
α = angle between electric vector of incident wave and line along R_2,
ϕ = one half the interior angle formed by the two lines along R_1 and R_2,
β = angle between axis of meteor trail and plane containing the transmitter, the receiver, and the meteor trail,
D = diffusion coefficient,
t = time after formation of trail,

all quantities being expressed in m.k.s. units.

The derivation of this equation is based upon the following assumptions:

(i) The trail is so oriented that the reflection is specular (that is, that the incident and reflected rays make equal angles with the trail axis). In order to fulfill this condition, the meteor trail must lie along a tangent to an ellipsoidal surface having the transmitting and receiving stations as foci.

(ii) The charge density in the trail is sufficiently small to allow the free passage of the radio waves.

(iii) The radial distribution of charge is Gaussian.

(iv) The ionization is distributed uniformly along the length of the trail.

(v) The trail is not distorted appreciably by the action of atmospheric turbulence.

The influence of trail orientation upon the amplitude of the signal may be illustrated by specific examples. Consider, first, a trail lying in a plane containing both the transmitter and receiver; the angle β is zero and the amplitude of the received signal is proportional to sec ϕ. For such a trail located near the mid-point of a 1000 km. path, the amplitude of the signal is about five times the equivalent back-scattered signal (for which $\phi = 0$ in Equation [1]). Secondly, consider a trail lying in a plane which is perpendicular to the transmission path; here $\beta = 90°$ and the forward-scattered signal is equal in amplitude to the equivalent back-scattered signal.

From the preceding paragraphs, it may be seen that forward-scatter measurements are most sensitive to meteor trails which are nearly horizontal and directed along the transmission path. On the other hand, the relative numbers of sporadic meteors entering a given area of the earth's atmosphere at different inclinations should vary approximately as the cosine of the zenith angle. The latter effect tends to offset the former in determining the sensitivity of the system to meteors of different orientations.

The exponential term of Equation [1], which applies only after a sharp rise to maximum amplitude, indicates that the signal should decay exponentially with time. For all orientations of the trail, the decay constant is proportional to $\sec^2\phi$. Because this factor is of the order of 25 for a trail near the mid-point of a 1000 km. path, the durations of forward-scattered signals are characteristically of the order of seconds for trails which would produce back-scattered signals lasting only fractions of seconds. Some experimental evidence in support of the exponential term has been reported by the Stanford group (14).

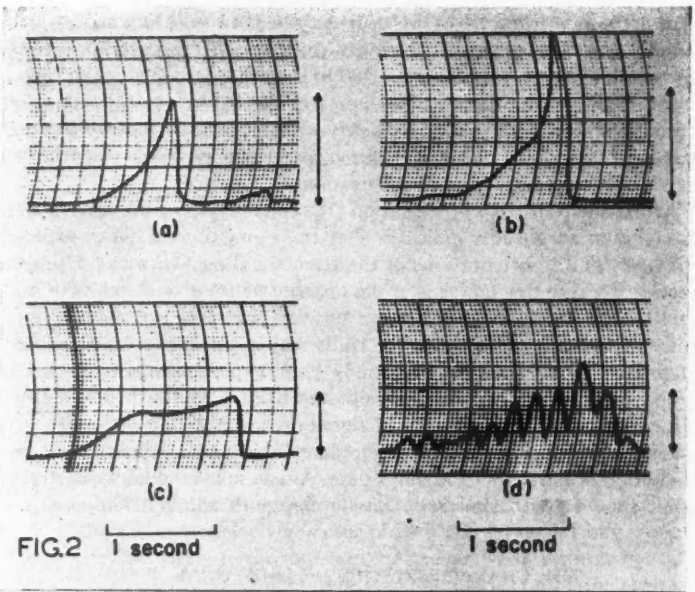
In addition to the decay type of signal described by Equation [1], it is to be expected that some of the signals should exhibit a sharp rise and fall separated by a period of fairly uniform amplitude. As in the case of back-scattering, such signals should arise from trails having charge densities in excess of a critical value.

THE CHARACTERISTICS OF INDIVIDUAL SIGNALS

Several examples of the signals observed by means of forward-scattering are shown in Figs. 2 and 3. In Fig. 2, the vertical scale is linear in amplitude, whereas in Fig. 3, the vertical scale is logarithmic. It should be noted that the ordinate axis in each record is curved and that time increases to the left.

Most meteor signals are of the decay type illustrated in Figs. 2(*a*) and 3(*a*). Such signals approximate closely the behavior predicted by Equation [1]. On some occasions, a sharp peak is observed shortly after the beginning of a signal. Records of this type of signal are shown in Figs. 2(*b*) and 3(*b*), and probably are examples of the resonance effect discussed by Herlofson (8), Kaiser and Closs (9), and Eshleman (5). Plasma resonance should occur only when the electric vector of the exciting wave has an appreciable component perpendicular to the trail axis.

Occasionally, the signal from a meteor trail has the form illustrated in Figs. 2(*c*) and 3(*c*), usually lasting longer than the decay type and exhibiting a "flat top", which is characteristic of the overdense trail. By analogy with the back-scatter case, it would be expected that the amplitude of this type of signal should be only a slowly varying function of charge density; the duration should be a function of both the charge density and the forward-scattering angle, ϕ. Most signals show shallow, irregular fading during their lifetime. Very rarely, signals of the type indicated in Figs. 2(*d*) and 3(*d*) are observed. These signals show a characteristic fading pattern, in which the minima are deep and short lived. The fading could arise by interference of the waves reflected from the two straight portions of a trail which had been bent or kinked by turbulence. It does, however, seem improbable that the conditions for specular reflection should be fulfilled separately by two parts of the same trail. Feinstein has



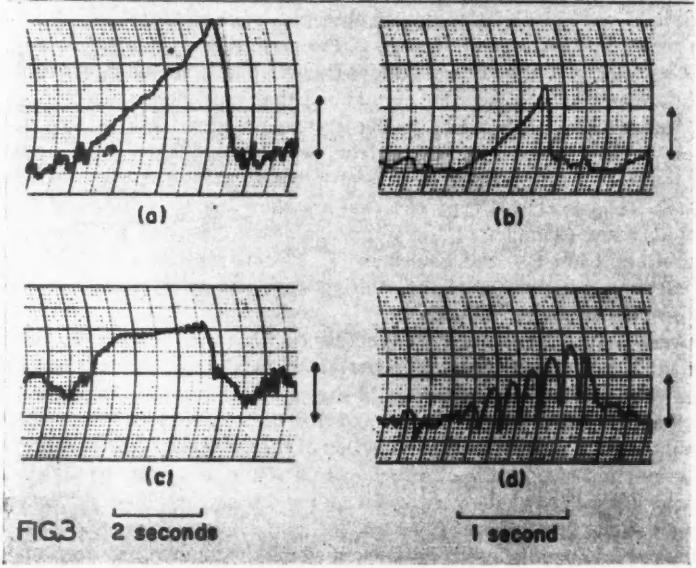


FIG. 2. Typical records of signals reflected from individual meteor trails (linear amplitude scale). Arrows represent a recording range of 3 μv.

FIG. 3. Typical records of signals reflected from individual meteor trails (logarithmic amplitude scale). Arrows represent a recording range of 20 db.

predicted similar fading characteristics for signals from trails having radial charge distributions which differ appreciably from Gaussian (7). The regular fading of the signals shown in Figs. 1(*d*) and 2(*d*) would seem to be described more reasonably in terms of the mechanism suggested by Feinstein than by simple distortion of the trail.

The examples shown in Figs. 2 and 3 were chosen from many hundreds of signals as being illustrative of the four main signal types. Most of the meteor signals can be classified as belonging to one or other of these types but some exhibit a complex structure which makes unambiguous classification impossible. While it is encouraging to find that most of the signals are of the decay type described by Equation [1], the presence of other signal types in significant numbers can not be disregarded. The experience gained from back-scatter experiments is of great assistance in interpreting forward-scattered signals but, as yet, this approach is qualitative.

METEOR SHOWERS

The major meteor showers give rise to effects which can be distinguished easily on the signal records. These effects are not the same or even closely similar for different showers. The records produced during four meteor showers are shown in Fig. 4. These records were made with an integration time constant of 64 sec. and the chart speed was reduced by a factor of four from that used for the records of Fig. 1. The transmission path in each case was that of Circuit 1 in Table I. For this circuit, the silent periods occur at half-hour intervals.

Fig. 4(*a*) (Loenids of 1952) shows relatively little change in the background integrated signals but does show very large signals of long duration occurring sporadically during the shower. Some of the spikes on this record represent integrated signal levels which rose 60 db. above the cosmic noise background. This signal level is only a few decibels below that which would be expected for free-space, line-of-sight transmission over the same distance. The major effect of the Quadrantids of 1953 (Fig. 4(*b*)) was to raise the integrated signal level during the shower. While a few large signals were recorded, the most striking effect appears to have been due to an increase in the rate of occurrence of small signals. The other two showers (Fig. 4(*c*) and (*d*)) caused both an increase in the integrated signal level and an increase in the number of very large signals. A given shower does not produce the same effect each year. Several of the major annual showers have produced records which were quite dissimilar for the two years of recording.

According to the geometrical terms of Equation [1], the effect produced by a meteor shower should depend upon the path of its radiant. An increase in meteor signal rate should occur when the shower meteors are travelling nearly parallel to, or perpendicular to the transmission path. The records taken during some showers, such as Geminids, do exhibit enhanced signal levels at certain times when the shower radiant appears to be favorably situated. On the other hand, no clear evidence of this effect has been found for other major showers. It may be that the effect is present but obscured by the normal daily variation of the sporadic meteor rate, or by random fluctuations in the signal rate.

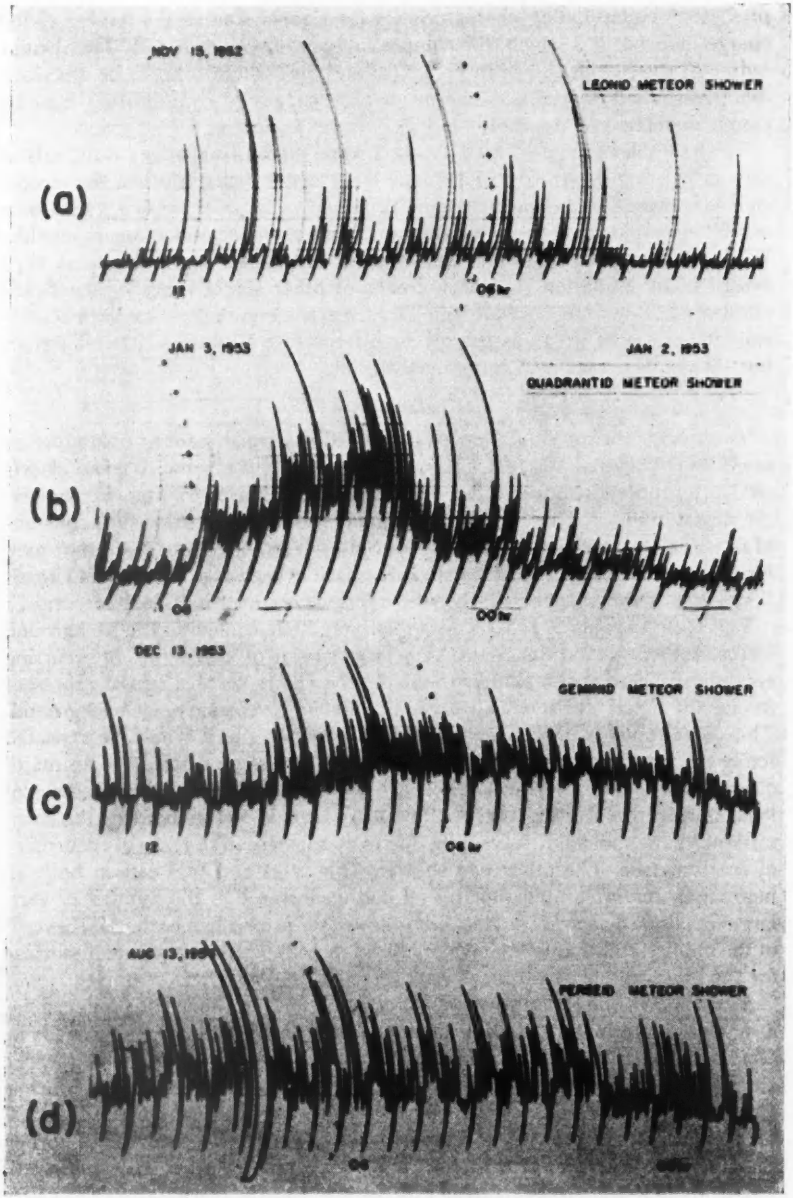


FIG. 4. Integrated signals recorded during four meteor showers.

The daytime meteor showers of May and June (12) also cause enhancements of the integrated signal which are difficult to correlate consistently with the shower radiant positions. However, the mean hourly signal rates for the months of May and June are abnormally high during the afternoon hours. This afternoon maximum is due undoubtedly to the influence of meteors belonging to the several daytime showers. Examination of the radiant positions for these showers suggests that there should be a similar maximum in the morning. It has not been possible to distinguish this morning shower effect from the normal maximum of the sporadic meteor signal rate.

In general, a meteor shower causes an increase in the signal rate but not always at a time of day which is related simply to the radiant position. A more careful analysis of the records is planned, particularly of those records obtained simultaneously from different circuits. It is hoped that in this way it will be possible to differentiate between true shower effects and random fluctuations in the rate of occurrence of sporadic meteors.

SPORADIC METEORS

The sporadic or non-shower meteors are likely to prove the most fruitful field for study by the forward-scatter technique. It is customary to assume that the radiants of sporadic meteors are uniformly distributed in a heliocentric system of coordinates. The motion of the earth causes an increase in the meteor rate on the morning side, and a decrease on the evening side of the earth. As a result, the diurnal component of the variation in meteor signal rate should have a maximum at 06 hr. local time. In the case of an east–west transmission path, a semidiurnal component with maxima at noon and midnight might be expected.

The mean daily variation of the hourly meteor signal rate as observed over Circuit 1 of Table I is shown in Fig. 5. The number of signals exceeding a given signal level were counted for each two-hour period for each of the 12 months of 1953. The curve shown in Fig. 5 is actually the mean of the monthly curves. The vertical scale indicates only relative signal rates, since the average value for each month was adjusted to a value of 100. The curve does indicate a

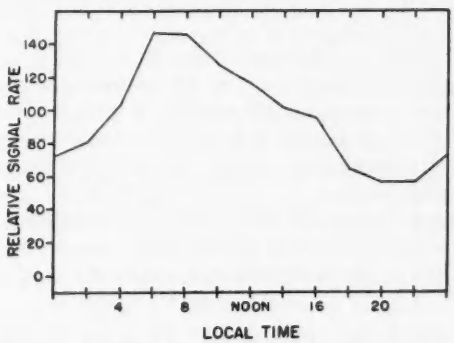


FIG. 5. Mean daily variation of the meteor signal rate.

maximum signal rate in the morning and a minimum in the evening but, contrary to expectations, the daytime signal rate is significantly larger than the nighttime signal rate. An harmonic analysis of the data of Fig. 5 reveals a diurnal component with maximum near 09 hr. and a semidiurnal component which is so small as to be of doubtful significance. In general, harmonic analyses of the data for each of the 12 months taken separately show similar results. The maxima of the diurnal components lie between 08 hr. and 10 hr., while the semidiurnal components are small and variable in phase from month to month. The failure of the observed variation to conform to the prediction of the preceding paragraph could mean that the initial assumption of uniform radiant distribution is not valid. On the other hand, the tendency toward an enhanced signal rate during the day may indicate that the ionization efficiency of the individual meteors is increased by solar radiation.

The mean daily variation of the meteor signal rate observed at Ottawa during April 1953 and April 1954 is shown in Fig. 6 (solid line) together with

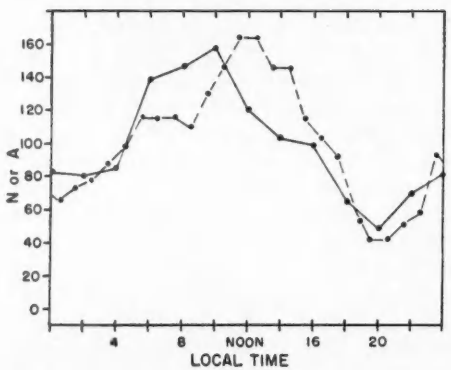


FIG. 6. The mean daily variation of the meteor signal rate, N, for the months of April 1953 and April 1954 (solid line) and the mean daily variation of the integrated signal strength, A, observed by Bailey *et al.* (1) for April 1951 (broken line).

the variation of the integrated signal strength observed at Stirling, by Bailey *et al.* (1), during April 1951 (broken line). The similarity between the two curves is further evidence in support of the suggestion made by Eshleman and Manning (6) and also by McKinley (13) that the continuous signal received at Stirling from Cedar Rapids was due, predominantly, to the overlapping signals scattered by meteor trails.

Any detailed computation of the integrated signal strength due to meteors must make use of a relation giving the number of signals observed as a function of amplitude. Such a relation should be of the form,

$$N \propto A^{-m}$$

where N is the hourly rate of occurrence of signals having amplitudes greater than A. For back-scatter measurements, Kaiser has concluded (10) that m

has a value of unity for sporadic meteors and a somewhat lower value for some showers. The results of an experimental determination of m for forward-scattering are given in Fig. 7. The plotted points represent the results from different periods scattered throughout 1953 and early 1954. In each case, the logarithm of the relative hourly meteor signal rate is plotted as a function of

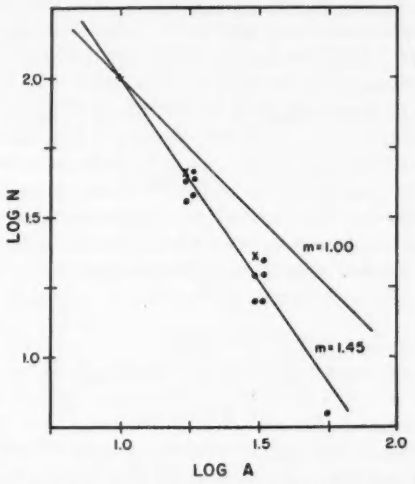


FIG. 7. Experimental relation between the logarithm of the integrated meteor signal rate N, and the logarithm of the signal amplitude, A.

the logarithm of the signal amplitude. The observed signal rate for each period was adjusted to a value of 100 for the lowest amplitude level. The points marked by crosses represent data from the period of the Perseid shower of August 1953. The remainder of the data were from periods without strong shower activity. The total number of meteor signals involved in the various determinations exceeded 20,000.

It is clear that the observed value of m is significantly higher than that derived from back-scatter measurements. One possible explanation is that the measurements were confined to the transition region where the signals are made up both of decay type signals from underdense trails and of enduring type signals from overdense trails. For signals from overdense trails, the value of m may be as great as four. Similar measurements of back-scattered signals made by Closs, Clegg, and Kaiser (3) show a transition region which is much narrower than the range of the present measurements. While the actual width of the transition region must depend somewhat upon the method of measurement, no significant curvature is detectable within the range of measurement for the data of Fig. 6. It does not seem likely, therefore, that the value obtained for m is the result of the particular range of amplitudes chosen for the measurements. Measurements over a greater range of amplitudes are required in order to verify this point.

CONCLUDING REMARKS

The foregoing results were chosen as examples of the type of measurements which can be made readily by use of the forward-scatter technique. No attempt has been made either to include a comprehensive body of data or to examine the results in detail. It is hoped to include such detailed studies in later papers some of which are now in preparation. The purpose of the present paper has been twofold: to indicate that some caution is necessary in applying the experience gained from back-scatter experiments to the forward-scatter process, and to demonstrate the relative ease with which forward-scatter measurements may be made. It is to be hoped that the present difficulties inherent in the application of back-scatter theory to forward-scattering will be resolved. In the meantime, the safest approach seems to be direct recourse to experiment. Certainly, insofar as the objective is an estimate of the utility of the meteor signals for communication, forward-scatter experiments are essential. This objective, however, need hardly be the only aim of forward-scatter experiments. It seems likely that the technique will yield new information concerning the physics of meteors.

ACKNOWLEDGMENTS

The authors are indebted to Messrs. C. Collins, J. Brown, and W. Rolfe for the construction and maintenance of equipment as well as for assistance with the recording program. Messrs. M. Costello and J. Day assisted with the analysis of the records. The operation of the experimental circuits is made possible by the continued co-operation of various members of the following organizations: The Naval Research Establishment, Halifax, N.S.; Suffield Experimental Station, Ralston, Alta.; Department of Transport, Churchill, Man.; and R.C.A.F., Winnipeg, Man.

REFERENCES

1. Bailey, D. K., Bateman, R., Berkner, L. V., Booker, H. G., Montgomery, G. F., Purcell, E. M., Salisbury, W. W., and Wiesner, J. B. Phys. Rev. 86: 141. 1952.
2. Beverage, H. H., Peterson, H. O., and Hansell, C. W. Proc. Inst. Radio Engrs. 19: 1313. 1931.
3. Closs, R. L., Clegg, J. A., and Kaiser, T. R. Phil. Mag. 44: 313. 1953.
4. Eckersley, T. L. J. Inst. Elec. Engrs. 67: 992. 1929.
5. Eshleman, Von R. Electronics Research Lab., Stanford University, Tech. Rept. No. 49. 1952.
6. Eshleman, Von R. and Manning, L. A. Proc. Inst. Radio Engrs. 42: 530. 1954.
7. Feinstein, J. J. Geophys. Research, 56: 37. 1951.
8. Herlofson, N. Arkiv Fysik, 3: 247. 1951.
9. Kaiser, T. R. and Closs, R. L. Phil. Mag. 43: 1. 1952.
10. Kaiser, T. R. Advances in Phys. 2: 495. 1953.
11. Lovell, A. C. B. and Clegg, J. A. Proc. Phys. Soc. (London), 60: 491. 1948.
12. Lovell, A. C. B. and Clegg, J. A. Radio astronomy. Chapman and Hall, Ltd., London. 1952.
13. McKinley, D. W. R. Can. J. Phys. 32: 450. 1954.
14. Villard, O. G., Peterson, A. M., Manning, L. A., and Eshleman, Von R. J. Geophys. Research, 58: 83. 1953.
15. Villard, O. G. and Peterson, A. M. QST, 37: 11. 1953.

SCATTERING OF A PLANE WAVE FROM A CIRCULAR DIELECTRIC CYLINDER AT OBLIQUE INCIDENCE[1]

By James R. Wait

ABSTRACT

A solution is given for the problem of a plane wave incident obliquely on a circular cylinder of infinite length. The electric properties of the cylinder are taken to be homogeneous and isotropic but otherwise arbitrary. It is shown that in the general case the scattered field contains a significant cross-polarized component which vanishes at normal incidence. While the solution is derived for the magnetic vector of the incident wave transverse to the axis of the cylinder, the corresponding result for the other polarization can be obtained from symmetry.

INTRODUCTION

The problem of diffraction of a plane wave at normal incidence by a homogeneous dielectric cylinder was solved many years ago by Lord Rayleigh (4). Since then his solution has been extended, rederived, and applied many times. As far as can be ascertained by this writer, the general case for oblique incidence has not been published.

It is the purpose of this paper to give a complete solution for this more general problem and to discuss some special cases which may be of interest.

THE SOLUTION

With respect to a cylindrical polar coordinate system (ρ, ϕ, z), the cylinder of dielectric constant ϵ_1 and permeability μ_1 occupies the space $\rho < a$. The direction of the incident plane wave makes an angle θ with the negative z axis and is polarized such that the electric vector is parallel to the plane $\phi = 0$. The z component of the electric field of the incident wave is then given by

$$E_z^{\,i} = E_0 \sin\theta \, e^{i\beta_2 \rho \sin\theta \cos\phi} e^{-i\beta_2 z \cos\theta} e^{i\omega t} \qquad [1]$$

where $\beta = (\epsilon_2 \mu_2)^{\frac{1}{2}}\omega$ with ϵ_2 and μ_2 being the dielectric constant and permeability of the homogeneous medium outside the cylinder. As a consequence of the assumed polarization, the z component of the magnetic field of the incident wave is zero. One might then be led to assume that the z components of the resultant magnetic fields are also zero. Such would certainly be true for normal incidence or for a perfectly conducting cylinder at oblique incidence. It can be readily shown, however, that the boundary conditions for the general case of oblique incidence on a dielectric cylinder cannot be met if the z component of the scattered magnetic field is taken to be identically zero. It is therefore necessary to express the resultant fields as a superposition of a set of T.M. (transverse magnetic) and T.E. (transverse electric) modes even though the incident wave is a purely T.M. mode.

Employing a well-known addition theorem for Bessel functions (5) the z component of the incident field can be written

[1]*Manuscript received January 28, 1955.*
Contribution from the Radio Physics Laboratory of the Defence Research Board, Ottawa, Canada.

[2] $$E_z^{\,i} = E_0 \sin\theta \sum_{n=-\infty}^{+\infty} i^n J_n(\lambda_2\rho) F_n$$

where $\lambda_2 = \beta_2 \sin\theta$ and $F_n = e^{-in\phi} e^{-i\beta_2 z\cos\theta} e^{i\omega t}$.

Since the cylinder is assumed to be of infinite length, the resultant fields must be periodic in the z direction and vary according to the factor $\exp(-i\beta_2 z\cos\theta)$. The z component of the scattered electric field can then be expressed in the form

[3] $$E_z^{\,s} = \sum_{n=-\infty}^{+\infty} a_n^{\,s} H_n^{(2)}(\lambda_2\rho) F_n$$

where the Hankel function of the second type ensures the proper behavior at infinity. The z component of the electric field inside the cylinder is written

[4] $$E_z = \sum_{n=-\infty}^{+\infty} a_n J_n(\lambda_1\rho) F_n$$

where the Bessel function of the first type is chosen to ensure that the field is finite at $\rho = 0$. Remembering that E_z must be a solution of the wave equation appropriate to the interior of the cylinder, it follows that

$$\lambda_1 = (\beta_1^2 - \beta_2^2\cos^2\theta)^{\frac{1}{2}} \qquad \text{where } \beta_1 = (\epsilon_1\mu_1)^{\frac{1}{2}}\omega.$$

The z components of the incident, secondary, and internal magnetic fields are then, respectively,

$$H_z^{\,i} = 0,$$

[5] $$H_z^{\,s} = \sum_{n=-\infty}^{+\infty} b_n^{\,s} H_n^{(2)}(\lambda_2\rho) F_n,$$

$$H_z = \sum_{n=-\infty}^{+\infty} b_n J_n(\lambda_1\rho) F_n.$$

The coefficients $a_n^{\,s}$ and $b_n^{\,s}$ specify the magnitude of the T.M. and T.E. modes respectively of the secondary field for $\rho > a$ whereas a_n and b_n pertain to the T.M. and T.E. modes of the internal field. These coefficients are to be determined by matching the tangential fields at the surface of the cylinder. The ϕ components of the fields are obtained from Maxwell's equations and are given by

$$E_\phi^{\,i} = \sum_{n=-\infty}^{+\infty} -\frac{hnE_0\sin\theta\, i^n J_n(\lambda_2\rho) F_n}{\rho\lambda_2^{\,2}},$$

$$E_\phi^{\,s} = \sum_{n=-\infty}^{+\infty} \left[-\frac{hna_n^{\,s}}{\rho\lambda_2^{\,2}} H_n^{(2)}(\lambda_2\rho) + \frac{i\mu_2\omega b_n^{\,s}}{\lambda_2} H_n^{(2)\prime}(\lambda_2\rho) \right] F_n,$$

$$E_\phi = \sum_{n=-\infty}^{+\infty} \left[-\frac{hna_n}{\rho\lambda_1^{\,2}} J_n(\lambda_1\rho) + \frac{i\mu_1\omega b_n}{\lambda_1} J_n'(\lambda_1\rho) \right] F_n,$$

[6] $$H_\phi^{\,i} = \sum_{n=-\infty}^{+\infty} \frac{-i\beta_2^{\,2} E_0\sin\theta}{\mu_2\omega\lambda_2} i^n J_n'(\lambda_2\rho) F_n,$$

$$H_\phi^{\,s} = \sum_{n=-\infty}^{+\infty} \left[-\frac{i\beta_2^{\,2} a_n^{\,s}}{\mu_2\omega\lambda_2} H_n^{(2)\prime}(\lambda_2\rho) - \frac{nhb_n^{\,s}}{\lambda_2^{\,2}\rho} H_n^{(2)}(\lambda_2\rho) \right] F_n,$$

$$H_\phi = \sum_{n=-\infty}^{+\infty} \left[-\frac{i\beta_1^{\,2} a_n}{\mu_1\omega\lambda_1} J_n'(\lambda_1\rho) - \frac{nhb_n}{\lambda_1^{\,2}\rho} J_n(\lambda_1\rho) \right] F_n,$$

where $h = \beta_2 \cos\theta$ and where the prime indicates a derivative with respect to the argument of the Bessel function. The boundary equations, written symbolically, are

$$[7] \qquad \left.\begin{aligned} H_z{}^{1}+H_z{}^{s} &= H_z \\ E_\phi{}^{1}+E_\phi{}^{s} &= E_\phi \end{aligned}\right\} \quad \text{at } \rho = a,$$

$$\left.\begin{aligned} E_z{}^{1}+E_z{}^{s} &= E_z \\ H_\phi{}^{1}+H_\phi{}^{s} &= H_\phi \end{aligned}\right\} \quad \text{at } \rho = a.$$

These equations are now solved to give

$$[8] \qquad a_n = [E_0 \sin\theta\, i^n J_n(v)+a_n{}^{s} H_n^{(2)}(v)]\frac{1}{J_n(u)},$$

$$[9] \qquad b_n = b_n{}^{s}\frac{H_n^{(2)}(v)}{J_n(u)},$$

$$[10] \qquad a_n{}^{s} = E_0 \sin\theta\, i^n\left[-\frac{J_n(v)}{H_n^{(2)}(v)}-\frac{2i\left(\frac{H_n^{(2)\prime}(v)}{vH_n^{(2)}(v)}-\frac{KJ_n'(u)}{uJ_n(u)}\right)}{\pi v^2[H_n^{(2)}(v)]^2 D}\right],$$

$$[11] \qquad b_n{}^{s} = \frac{\beta_2}{\mu_2\omega} E_0 \sin\theta\, i^n\left[\frac{2}{\pi v^2}\left(\frac{1}{u^2}-\frac{1}{v^2}\right)\frac{n\cos\theta}{[H_n^{(2)}(v)]^2 D}\right]$$

with

$$[12] \quad D = \left(\frac{H_n^{(2)\prime}(v)}{vH_n^{(2)}(v)}-\frac{KJ_n'(u)}{uJ_n(u)}\right)\left(\frac{H_n^{(2)\prime}(v)}{vH_n^{(2)}(v)}-\frac{N^2 J_n'(u)}{KuJ_n(u)}\right)-\left(\frac{1}{v^2}-\frac{1}{u^2}\right)^2 n^2\cos^2\theta,$$

$$N^2 = \frac{\beta_1{}^2}{\beta_2{}^2} = \frac{\epsilon_1\mu_1}{\epsilon_2\mu_2}, \qquad K = \frac{\mu_1}{\mu_2},$$

$$u = \lambda_1 a = (\beta_1{}^2-\beta_2{}^2\cos^2\theta)^{\frac{1}{2}} a,$$

and

$$v = \lambda_2 a = \beta_2 \sin\theta\, a.$$

This constitutes the complete solution of the general problem. The corresponding result for the case of the incident magnetic vector in the plane $\phi = 0$ is of the same form as above if E is replaced by H, H is replaced by $-E$, ϵ is replaced by μ, and μ is replaced by ϵ, throughout.

SOME SPECIAL CASES

(1) *Normal Incidence*

The coefficients for normal incidence (i.e. $\theta = 90°$) reduce to

$$[13] \qquad a_n = [E_0 i^n J_n(v)+a_n{}^{s} H_n^{(2)}(v)]\left[\frac{1}{J_n(u)}\right],$$

$$[14] \qquad a_n{}^{s} = -E_0 i^n\left[\left(\frac{N^2 J_n'(u)}{KuJ_n(u)}-\frac{J_n'(v)}{vJ_n(v)}\right)\Big/\left(\frac{N^2 J_n'(u)}{KuJ_n(u)}-\frac{H_n^{(2)\prime}(v)}{vH_n^{(2)}(v)}\right)\right]\frac{J_n(v)}{H_n^{(2)}(v)},$$

$$b_n = b_n{}^{s} = 0,$$

where $u = \beta_1 a$ and $v = \beta_2 a$.

This result corresponds to Rayleigh's (4) original solution mentioned in the Introduction.

(2) *Highly Conducting Cylinder*

When the dielectric constant of the cylinder becomes very large or "lossy" such that $|\epsilon_1/\epsilon_2| \to \infty$ it follows that

$$[15] \qquad a_n^s = -\frac{J_n(v)}{H_n^{(2)}(v)} i^n E_0 \sin\theta, \qquad b^s = 0,$$

where $v = \beta_2 a \sin\theta$. This result agrees with the solution published by Carter (1). When $v \ll 1$, the coefficients are given by

$$[16] \qquad a_0^s \simeq -i\frac{\pi}{2}\frac{E_0 \sin\theta}{\log(\frac{1}{2}v\Gamma)}$$

with $\log \Gamma = 0.5772$ and

$$[17] \qquad a_1^s = a_{-1}^s \simeq -\tfrac{1}{4}\pi v^2 E_0 \sin\theta.$$

The higher coefficients contain higher powers of v. In this case it can be seen that only the zero order mode is significant. To the same approximation that $v \ll 1$, a_0^s can be modified to account for the case when the conductivity or dielectric constant is large but finite, whence

$$[18] \qquad a_0^s \simeq -i\frac{\pi}{2} E_0 \sin\theta \left[\frac{1}{\log(\frac{1}{2}v\Gamma)+\Delta}\right]$$

where $\Delta = J_0(u)/u\,J_1(u)$ with $u \simeq \beta_1 a$ and $K = 1$.

When $|u|$ is large compared to one the correction factor is given to sufficient accuracy by $\Delta \simeq i/u$.

(3) *Highly Permeable Cylinder*

When the permeability of the cylinder becomes very large such that $K = \mu_1/\mu_2 \to \infty$ it follows that

$$[19] \qquad a_n^s = -\frac{J_n'(v)}{H_n^{(2)'}(v)} i^n E_0 \sin\theta$$

and

$$b_n^s = 0$$

where $v = \beta_2 a \sin\theta$. This particular result was also given by Carter (1). When v is very small only the first two modes are significant and they are given by

$$[20] \qquad a_0^s \simeq \tfrac{1}{4} i\pi v^2 E_0 \sin\theta$$

and

$$[21] \qquad a_1^s = a_{-1}^s \simeq \tfrac{1}{4}\pi v^2 E_0 \sin\theta.$$

(4) *Highly Dense Cylinder*

When the imaginary part of the permeability or dielectric constant of the cylinder is large but still finite it is permissible to replace $J_n(u)$ and $J_n'(u)$ by their limiting asymptotic forms so that $J_n'(u)/J_n(u) \simeq i$ for $|u| \gg 1$. The

expressions for a_n^s and b_n^s given by equations [9] to [12] are then less complicated. With this simplification it can be verified that

$$\left.\begin{aligned} E_\phi^i + E_\phi^s &= -(\mu_1\omega/\beta_1)H_z^s \\ E_z^i + E_z^s &= (\mu_1\omega/\beta_1)(H_\phi^i + H_\phi^s) \end{aligned}\right\} \quad \text{for } \rho = a, \tag{22}$$

which are the usual approximate boundary conditions appropriate for the tangential field at an interface between an insulator and a good conductor (5).

(5) *Small Dielectric Cylinders*

When the diameter of the cylinder is small enough that both u and $v \ll 1$, it follows that for $K = 1$

$$a_0^s \simeq -\tfrac{1}{4}i\pi v^2(N^2-1)\, E_0 \sin\theta, \tag{23}$$

$$a_1^s = a_{-1}^s = \frac{\pi v^2(1-N^{-2})^2\cos^2\theta\, E_0 \sin\theta}{2(1+N^{-2})-(1-N^{-2})^2\cos^2\theta}, \tag{24}$$

$$b_1^s = -b_{-1}^s = \frac{\tfrac{1}{2}i\pi v^2(\beta_2/\mu_2\omega)(1-N^{-2})\cos\theta\, E_0 \sin\theta}{2(1+N^{-2})-(1-N^{-2})^2\cos^2\theta} \tag{25}$$

where the other coefficients are of higher order in v. It should be noted that at normal incidence (i.e. $\theta = 90°$) only the coefficient a_0^s is of order v^2.

(6) *Small Permeable Cylinder*

When the diameter of the cylinder is small enough that u and $v \ll 1$ it follows that for $N^2 = K$

$$a_0^s \simeq 0,$$

$$a_1^s = a_{-1}^s \simeq \frac{\pi v^2}{4}\left[\frac{2(K-1)+K(1-K^{-1})^2\cos^2\theta}{2(K+1)-K(1-K^{-1})^2\cos^2\theta}\right] E_0 \sin\theta, \tag{26}$$

and

$$b_1^s = -b_{-1}^s \simeq \frac{\tfrac{1}{2}i\pi v^2(\beta_2/\mu_2\omega)(K-1)\cos\theta\, E_0 \sin\theta}{2(K+1)-K(1-K^{-1})^2\cos^2\theta}. \tag{27}$$

The other coefficients are again of higher order in v.

(7) *Low Contrast Case*

If the electrical properties of the cylinder differ only slightly from the exterior and if the diameter of the cylinder is large compared to the wavelength, the coefficients of order n can be considerably simplified. For example if $(N^2-1) \ll 1$, $(K-1) \ll 1$, and $v^{-2} \ll 1$ it follows that

$$a_n^s \simeq E_0 \sin\theta\, i^{n+1}(\pi/4)v(N^2-K^2)\, J_n'(v)\, J_n(v) \tag{28}$$

and

$$b_n^s = (\beta_2/\mu_2\omega)\, E_0 \sin\theta\, i^n(\pi/2)(N^2-1)\, n\cos\theta\, [J_n(v)]^2. \tag{29}$$

FAR FIELD APPROXIMATION

When the fields are observed at large distances from the cylinder it is permissible to replace the Hankel functions with their limiting asymptotic forms.

With this approximation it readily follows that the far fields, in terms of spherical coordinates, at (r, θ, ϕ) are

$$[30a] \qquad E_\theta^s \simeq -\left(\frac{2i}{\pi\beta_2 r}\right)^{\frac{1}{2}} \frac{e^{-i\beta_2 r}}{\sin^2\theta} \sum_{n=-\infty}^{+\infty} a_n^s \, i^n \cos n\phi,$$

$$[30b] \qquad H_\theta^s \simeq (\beta_2/\mu_2\omega)\, E_\theta^s,$$

$$[30c] \qquad E_\phi^s \simeq -\left(\frac{2i}{\pi\beta_2 r}\right)^{\frac{1}{2}} \frac{e^{-i\beta_2 r}}{\sin^2\theta}\left(\frac{\mu_2\omega}{\beta_2}\right) \sum_{n=-\infty}^{+\infty} b_n^s \, i^{(n+1)} \sin n\phi,$$

$$[30d] \qquad H_\theta^s \simeq -(\beta_2/\mu_2\omega) E_\phi^s$$

where $r = \rho \sin\theta + z\cos\theta$. The coefficients a_n^s and b_n^s have been determined earlier for the general case.

The special cases of the far field for normal incidence, highly conducting cylinders, and small cylinders can readily be obtained by substituting the appropriate values of a_n^s and b_n^s into equations [30*a*] to [30*d*]. The special case which is particularly simple in the far field region corresponds to the cylinder whose dielectric constant or permeability is nearly the same as its surroundings. Employing a known summation formula for Bessel functions (6) and referring to equations [28] and [29] it follows that for the low contrast case:

$$[31] \qquad E_\theta^s \simeq E_0\left(\frac{2i}{\pi\beta_2 r}\right)^{\frac{1}{2}} e^{-i\beta_2 r} \frac{i\pi v(N^2-K^2)}{4\sin\theta} \cos(\phi/2)\, J_1[2v\cos(\phi/2)]$$

and

$$[32] \qquad E_\phi^s \simeq E_0\left(\frac{2i}{\pi\beta_2 r}\right)^{\frac{1}{2}} e^{-i\beta_2 r} \frac{i\pi v(N^2-1)}{2} \cot\theta \sin(\phi/2)\, J_1[2v\cos(\phi/2)].$$

These expressions are actually equivalent to the results derived and discussed by Eshleman (2). His method consists of independently summing the fields scattered by the individual volume elements of the cylinder. Consequently his results are only valid for the low contrast case.

CONCLUDING REMARKS

The results given in this paper, while derived for a homogeneous dielectric and permeable cylinder, are applicable to a homogeneous column of ionization. This is an idealized model for a meteor trail. To translate the results to the case of the ionized column it is necessary to replace the ratio ϵ_1/ϵ_2 by the usual Sellmeyer expression for the equivalent dielectric constant of a neutral ionized region (3). In this case the ratio μ_1/μ_2 is essentially unity.

It is also worth noting that the general formulae for the scattered fields can be simply extended to the case of a semicylindrical boss situated on a perfectly conducting ground plane. The presence of the plane interface is accounted for by applying the well-known "image principle". This model is relevant to the problem of diffraction of radio waves by ridges.

Extensive numerical calculations based on equations [10] and [11] are being carried out in this laboratory. These will be reported at a later date along with some experimental data.

REFERENCES

1. CARTER, P. S. Proc. Inst. Radio Engrs. 31: 671. 1943.
2. ESHLEMAN, Von R. Mechanism of radio reflections from meteoric ionization. Stanford University, Electronic Research Lab. Tech. Rept. No. 49. July 15, 1952.
3. FEINSTEIN, J. J. Geophys. Research, 56: 37. 1951.
4. RAYLEIGH, Lord. Phil. Mag. 36: 365. 1918.
5. STRATTON, J. A. Electromagnetic theory. McGraw-Hill Book Company, Inc., New York. 1941.
6. TRICOMI, F. G., OBERHETTINGER, F., MAGNUS, W., and ERDÉLYI, A. Higher transcendental functions. Vol. 2. McGraw-Hill Book Company, Inc., New York. 1953. p. 102, formula No. 38.

THE TOPOGRAPHY OF SOLID–LIQUID INTERFACES OF METAL CRYSTALS GROWING FROM THE MELT[1]

By C. Elbaum and B. Chalmers[2]

ABSTRACT

An improved technique of separating the liquid portion of the metal from the adjacent crystal has been developed. Microscopic examination of the interfaces prepared by this method has revealed a new surface structure. It has been found that the presence or absence of the structure depends on the crystallographic orientation of the specimen. The structures have been observed in all of the metals investigated in the present work, namely lead, tin, and zinc. A detailed study of the structure has been made in the case of lead. It was observed that, when the angle between the macroscopic plane of the interface and either the (111) or the (001) plane was less than a certain critical value, the interface consisted of steps or terraces approximately 0.001 mm. high. A mechanism for the formation of those steps is proposed.

INTRODUCTION

The purpose of this research was to investigate the configuration and structure of the solid–liquid interfaces of metal crystals grown from the melt. Since freezing takes place precisely at those interfaces, a detailed knowledge of their structure during growth would be of considerable help in the attempts to elucidate both the process of solidification and the subsequent structure of the solid, as well as the phenomenon of anisotropy of the solid–liquid interfacial energies. It was, therefore, decided to investigate those interfaces as a function of crystallographic orientation and varying growth conditions. An improved technique has been developed for separating, during crystal growth, the liquid from the adjacent solid. This technique preserves the solid–liquid interface undamaged and in substantially the same state as it was during the process of solidification. A study of the structure observed on the interfaces prepared by this method is presented below.

EXPERIMENTAL TECHNIQUE

The principal material used in this research was high purity lead, supplied by Messrs. Johnson, Matthey and Company. The purity of this material is stated to be 99.996%, with the major detectable impurities, bismuth, copper, silver, cadmium, zinc, iron, arsenic.

Single crystals and bicrystals of predetermined orientation were produced from this lead by growth from the melt using the horizontal boat method (1).

In the present investigation the main object of study is the solid–liquid interface of crystals growing into their own melt. It was important, therefore, to separate the liquid from the solid during the process of growth, and to preserve the topography of the interface. In the previous studies (4, 5, 6) of

[1]*Manuscript received January 6, 1955.*
Contribution from the Department of Metallurgical Engineering, University of Toronto, Toronto 5, Ontario.
[2]*Professor of Metallurgy at the Division of Applied Science, Harvard University, Cambridge 38, Massachusetts.*

solid–liquid interfaces carried out in this laboratory, this was achieved by letting the liquid run off through one end of the trough, or through a hole in the bottom of the container when part of the melt had solidified. However, it was felt that by using this method some of the liquid might be retained by surface tension in the irregularities of the interface. It would subsequently freeze and possibly mask the fine structure which may exist on the interface during growth. The difficulty was overcome by applying to the crystal a higher acceleration than gravity. The acceleration was gradually increased until no further change in the appearance of the interface could be observed.

The mechanism used for the separation of the solid from the liquid is shown in Fig. 1. It consists of a cylindrical graphite boat attached at one end to a helicoidal spring. The boat is free to move axially in a pyrex tube, which

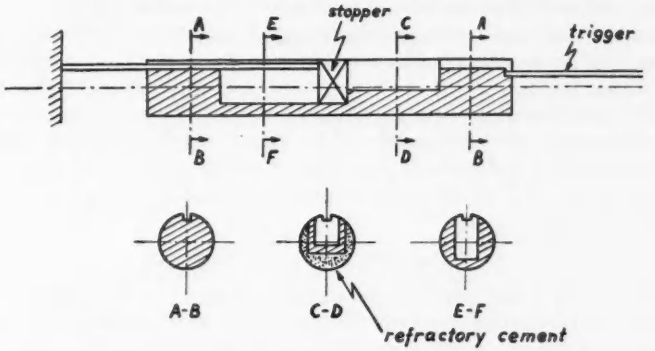


FIG. 1. Decanting mechanism.

serves as a guide for its movement. The spring is in turn attached to a small steel frame, the latter is rigidly fastened to one end of the pyrex tube. On the steel frame is also mounted a mobile steel rod, which serves as a trigger. The trough has two levels. The upper level serves for the normal operation of growth and is separated from the lower level by a graphite stopper which is fixed with respect to the pyrex tube, but slides easily along the lower level part of the trough when the boat moves along the tube. The lower level of the trough receives the liquid metal during decanting. Before the melting operation is started, the spring is put under tension. A crystal is then grown from a seed crystal of controlled orientation by the method to which reference is made above. When the crystal has grown the desired distance, the trigger is released and the spring pulls the boat away from the graphite stopper (which remains in its original position, since it is fixed with respect to the pyrex tube). The acceleration given to the boat is proportional to the extension of the spring, which can be controlled by adjusting the length of the trigger rod. In this way the crystal is pulled away from the liquid together with the boat, and the liquid runs into the lower level of the trough, now opened by the displacement of the stopper with respect to the boat.

In order to approach as closely as possible the ideal conditions of growth with unidirectional heat flow and to obtain flat solid–liquid interfaces, perpendicular to the direction of heat flow, it was necessary to reduce the lateral heat losses in the boat. This was achieved by reducing, on the outside, the thickness of the walls and bottom of the boat in the region where the crystals were grown, and replacing the removed graphite with a coating of alundum cement, which has very low heat conductivity.

The speed of growth was determined approximately by agitating the liquid metal at equal intervals of time and thus producing a small frozen ripple at the solid–liquid interface. A measure of the spacing between the ripples gives immediately the average speed of growth.

The temperature gradient along the boat could be changed by varying the amount of water flowing through a copper tube inserted tightly at the colder end of the boat. It was also necessary to vary simultaneously the temperature, or position of the furnace. The speed of growth and the temperature gradient could thus be varied.

After the specimens were grown and decanted, they were examined under the microscope and photographs of the characteristic parts were taken. The crystallographic orientations, with respect to the direction of growth, of all the crystals present in a specimen were determined from Laue back reflection X-ray photographs.

RESULTS AND OBSERVATIONS

Microscopic examination of the interface prepared by the method described above has revealed a structure not previously described in detail (3). The presence or absence of the structure depends on the crystallographic orientation of the specimen. Fig. 2 shows an example of the structure obtained on a



FIG. 2. Interface of a bicrystal, the boundary between the two crystals is indicated by arrows. ×410.

solid–liquid interface of a lead crystal. The photomicrograph shows a bicrystal, the boundary between the two crystals being indicated by arrows. It can be seen that the appearance of the interface is entirely different on either side of the boundary. The upper part of the photomicrograph shows a steplike structure; many varieties of these steps have been observed. The type of interface that appears on the lower part of the photomicrograph will hereafter be called "structureless".

The term "structureless" has been applied to all the interfaces on which no steps could be seen, within the resolving power of the light microscope.

Although the definition of a "structureless" face is quite arbitrary, it corresponds, in fact, to a real division observed in the appearance of different interfaces, as a function of the crystallographic plane which constitutes the macroscopic interface.

The poles of the planes, constituting the interfaces of the lead specimens, have been plotted on a standard (001) stereographic projection for the cubic system. It is indicated on this plot whether the interface shows a structure or not. Fig. 3 represents the plot, which shows clearly that when the plane of the

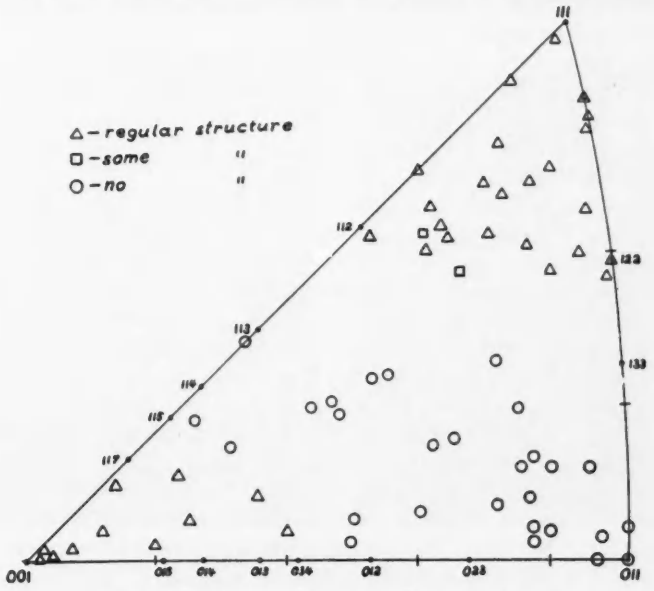


FIG. 3. The directions of growth of the lead specimens.

interface lies within a certain critical angular distance from either the {111} or the {001} planes, it exhibits the steplike structure. When the tilt of the crystallographic plane constituting the interface, with respect to either one of the above two planes, is greater than the critical angle, the interface is structureless.

In the neighborhood of the {111} plane, the type of structure is a function only of the angular distance of the interface from the {111} plane and not of the actual plane of the interface. In other words, the same angular rotation of the plane of the interface around any axis of rotation, perpendicular to the ⟨111⟩ direction, will give the same type of structure, as long as the rotation is not greater than 15°–20°. For tilts greater than that angle (which appears to be the critical angle) the structure disappears. The angular departure from the {001} plane, for which the structure is found, is limited by about the same angle (15°–20°) as in the case of the {111} plane. As in the neighborhood of the {111} plane, the type of structure is only a function of the angular distance of the interface from the {001} plane, and does not depend on the direction of rotation. For rotations of the interface of about 15°–20° around any axis normal to the ⟨001⟩ direction the same type of structure appears.

It has been mentioned above that the structure varies as a function of the angular distance of the plane of the interface from either the {001} or the {111} plane. The steplike structure on Fig. 2 corresponds to an interface tilted about 12° with respect to the {001} plane. The other part of the same photomicrograph shows a structureless face.

As the plane of the interface gradually approaches the {001} face, the steps become flatter and bigger. Finally, in the immediate vicinity of the {001} face, the steps change into wide terraces, as shown on Fig. 4. Fig. 5 shows several features of the structure observed on interfaces corresponding to tilts within 5° of the {001} plane.

A hexagonal network is frequently observed on the interface. This corresponds to the cell structures studied and described by Rutter and Chalmers (4). Its occurrence somewhat modifies, but does not obscure, the steplike structure under discussion. Figs. 6 and 7 are examples of interfaces in which both the cells and the steplike structure occur. These photographs corresponding to interfaces close to the {111} plane show that the general characteristics of such surfaces are similar to those close to the {001} plane.

The observations outlined above lead to the assumption that the steps of the interface consist of small portions of the close-packed planes {111} or {001}. These planes appear as long as the interface is not tilted beyond a certain critical angle with respect to them. This assumption has been confirmed, in so far as the geometrical relations are concerned, by the following experiment. A bicrystal was produced in which one of the {111} planes of each component crystal was inclined in the same way and by the same angle with respect to the common boundary. Microscopic examination of the solid–liquid interface after decanting revealed the usual steplike structure, symmetrically disposed with respect to the boundary. The position of the planes forming

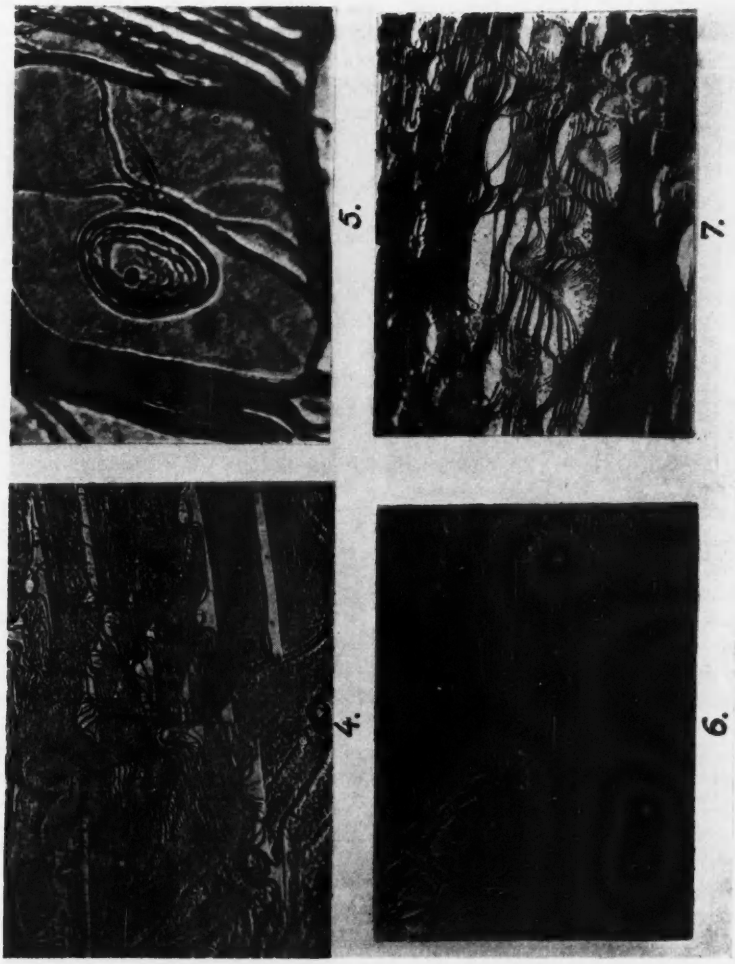


FIG. 4. Interface on which wide steps begin to appear. ×520.
FIG. 5. Large steps on an interface nearly parallel to a {001} plane. A curved line joining two points appears in the center of the convex part. ×1060.
FIG. 6. Interface of a bicrystal showing different types of steps for different crystallographic directions of growth. The grain boundary has migrated away from its original position along cell boundaries. ×176.
FIG. 7. Steps on a convex surface of a cell. ×176.

these steps, as determined from optical reflections, corresponded to the position of the (111) planes of the two crystals, as determined from Laue back reflection photographs.

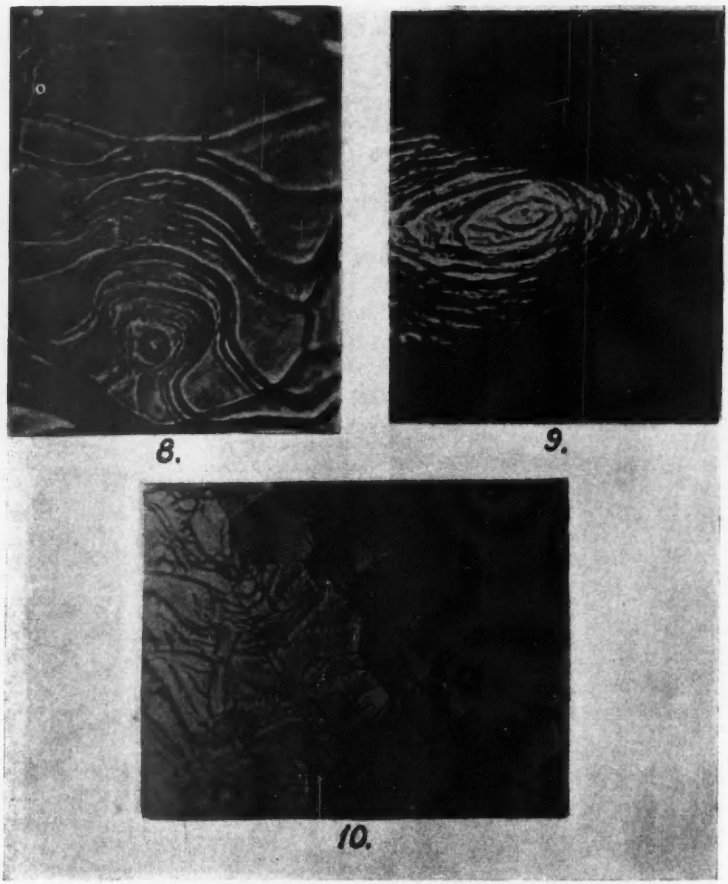


FIG. 8. Propagation of large steps on an interface nearly parallel to a {111} plane. The center of the convex part is approximately hexagonal. ×1060.
FIG. 9. A "spiral" in the center of a convex part of an interface. ×1060.
FIG. 10. Interface of a bicrystal. Pronounced migration of the grain boundary away from its original position along cell boundaries. ×176.

A very characteristic structure appears when the interface is within approximately 5° from the {111}, or {001} planes. It is shown in Figs. 5 and 8. It was determined, by means of oblique illumination, that the rounded parts of the structure in question are convex and project ahead of the general plane of the interface. The tops of the projections sometimes appear to consist of one

or two turns of a spiral, which in three dimensions would be a conical helicoid (see Fig. 9). In many other cases they consist of a curved line joining two points, surrounded by a series of closed rings of increasing diameter (see Fig. 5). The photomicrograph of Fig. 8 has been taken on an interface tilted 4° with respect to the {111} plane. It may be significant that the center of the projection exhibits a hexagonal contour.

Influence of Growth Conditions

The influence of speed of growth of the specimen on the character and dimensions of the structure was investigated. In the range of speeds from 0.2 mm./min. to 10 mm./min. no systematic variation of any kind could be observed.

The temperature gradient along the specimen (between the hottest part of the liquid and the coldest part of the solid) was varied, for different speeds of growth, from less than 10° C./cm. to approximately 40° C./cm. As in the case of speed of growth, no difference in the structure was noted.

In both cases, and for any imposed variation within the stated limits, the dependence of the structure on crystallographic orientation of the specimen remained unchanged.

The third variable investigated was the acceleration given to the solid during the decanting operation. The acceleration was varied from approximately 7000 cm./sec./sec. down to 1500 cm./sec./sec., by steps of 1000 cm./sec./sec. and 500 cm./sec./sec., without any observable effect on the character of the structure. As above, no change was observed in crystallographic dependence. It should be emphasized that the acceleration is not a variable of the growth process. The study of its variation was undertaken to examine the possibility that the structure appeared as an effect of plastic deformation of the metal, in the vicinity of the interface, during the process of accelerated decanting.

Several experiments were performed during which the specimens were quenched immediately after the decanting operation. No differences in the appearance of the structure or its crystallographic dependence were observed. Thus the possibility of the structure appearing as a result of thermal etching, which would occur after the decanting operation, has been eliminated. An additional observation that has been made is that boundaries separating the two crystals of a bicrystal do not always coincide exactly with the position of the change from structure characteristic of one crystal to that characteristic of the other. The change from one structure to the other always occurs at the boundaries of the cells when these are present, and the grain boundary, as revealed by a dark line in the specimen, frequently crosses the cells in the vicinity of the boundary (see Fig. 10).

Summary of Observations

1. During growth from the melt, the solid–liquid interface of a growing lead crystal consists, in some cases, of steps formed by portions of {111}, or {001} planes. The steps vary in width from less than 0.001 mm. to about 0.01 mm. and are usually less than 0.001 mm. high.

2. The presence, or absence, of the steps depends on the crystallographic plane, which constitutes the macroscopic interface.

The structure appears if the interface is not inclined at more than a certain critical angle from the {111} or {001} planes. The critical angle varies from 15° to 20° depending on the direction of tilt.

3. When the interface is close to a {111} or {001} plane the steps change into wide terraces, centered around small projections that stick out into the liquid. The top of these projections sometimes appears to consist of one or two turns of a spiral, which in three dimensions would be a conical helicoid. In many other cases it consists of a half-loop line joining two points, surrounded by a series of closed rings of increasing diameter.

4. When the interface is tilted beyond the critical angle, with respect to the {111}, or {001} plane, the presence of steps can not be detected by means of a light microscope.

5. The character and dimensions of the structure are not affected by changes in either the speed of growth of the crystal from 0.2 mm./min. to 10 mm./min., or the temperature gradient along the growing specimen, from less than 10° C./cm. to approximately 40° C./cm. It should be emphasized that only the over-all temperature gradient along the whole specimen has been measured. No attempt has been made to determine the actual temperature gradient in the immediate vicinity of the solid–liquid interface. It has been considered, however, throughout this work, that during the process of crystal growth, the heat flowed only in one direction, which is the direction of the crystal's long dimension. This amounts to assuming that there was no lateral heat loss through the walls of the container in which the crystals were grown. As previously stated, the walls were carefully insulated; thus the above assumption seems to be justified.

6. Similarly, the crystallographic relations, and in particular the critical angle of tilt of the interface with respect to the {111} and {001} for which the structure disappears, are not changed by the above-mentioned variations.

7. Structures similar to those appearing on solid–liquid interfaces of lead have been observed on tin and zinc.

DISCUSSION

It has been shown in the previous paragraphs that the steplike structure of solid–liquid interfaces of lead crystals grown from the melt depends on the crystallographic direction of growth.

The freezing process is, therefore, not independent of the crystallographic orientation of the mean interface. The described departure of the solid–liquid interface from the isothermal surface, for certain directions of growth, leads one to attribute to this interface a crystallographic identity.

The occurrence of steps, visible at moderate magnification, of which the major portion is parallel, or nearly so, to either the {111} or {001} planes of the lattice can be explained as follows.

It will be assumed that we can describe any surface in terms of the close packed or nearly close packed planes to which it most nearly approximates.

Thus an interface parallel to the {111} plane of a face centered cubic structure will be a close packed plane. As the surface deviates from exact parallelism, it acquires "steps" that become progressively closer together as the angle increases. This is illustrated schematically in Fig. 11 *a*, *b*, and *c*, for the close packed face. Angles between those corresponding to integral steps consist of an alternation of two step sizes (see Fig. 11*d*).

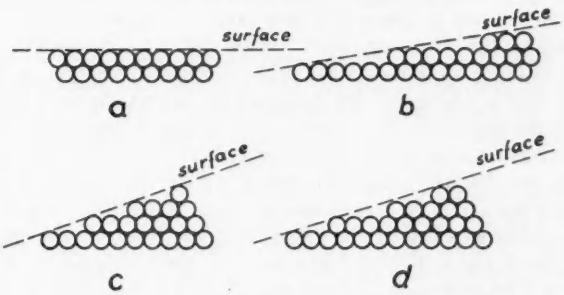


FIG. 11. Monoatomic steps on different crystallographic faces.

If we supposed that growth could only take place by the addition of atoms at points where they will be in contact with five atoms that occupy sites characteristic of the growing crystal we would expect each "step" to move steadily to the left (in Fig. 11). They would remain the same distance apart; for example in Fig. 11*b* there would always be about six atom rows between steps. Such steps would not, of course, be observable.

We must now consider the stability of a surface structure in which the steps are equally spaced, or nearly so. It will be shown that if the steps are not too close together, equal spacing is unstable, and that there will be a tendency for steps to group together in clusters. There are two distinct mechanisms which lead to the instability of equally spaced steps.

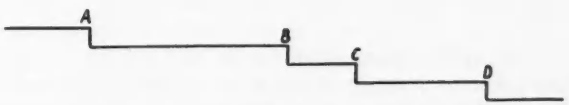


FIG. 12. Unequally spaced steps on an interface.

The rate of advance of an individual step will be controlled by the rate of dissipation of latent heat from its immediate vicinity. If, therefore, two neighboring steps *B* and *C* are rather closer together than the others (Fig. 12), we would expect them to advance more slowly than steps which are further from their neighbors, such as *A*, *D*, etc. The step *A*, therefore, will tend to catch up with *B* and *C*, forming a group of three steps which will advance even more slowly. This will continue until all the steps are included in clusters

of this type. Such clusters will occur at more or less regular intervals across the surface of the crystal resulting eventually in visible steps. The other possible mechanism leading to the formation of visible steps is as follows: it is possible that a cluster of atoms equivalent to the embryo of a new layer may form on a surface at a region not in contact with an advancing step. Let us consider a small angle, as in Fig. 13*a*, and let us suppose that such a cluster forms at the point marked *Q*. If this cluster remains in position long enough, it will join up witn the next layer *b*. Layer *b* is now larger than before, and layer *c* is smaller, as in Fig. 13*b*. The next result will be that more nucleation on layer *b* of new parts of layer *a* becomes more probable than nucleation on the other layers *a*, *c*, *d*, and *e*. There are two reasons. One is that the area of *b* is now larger, and as the probability of nucleation or embryo formation *per unit area* is constant at a given amount of supercooling, there should be more nucleation on the larger area. Secondly, parts of layer *b* will be at a lower temperature than any part of *a*, *c*, *d*, or *e*, because they will be further from any region where heat is being supplied by the release of latent heat, i.e. the edges where freezing is taking place. Hence, there is a stronger probability that *a* will extend over *b*. The process is limited only by the temperature limits within which growth can take place.

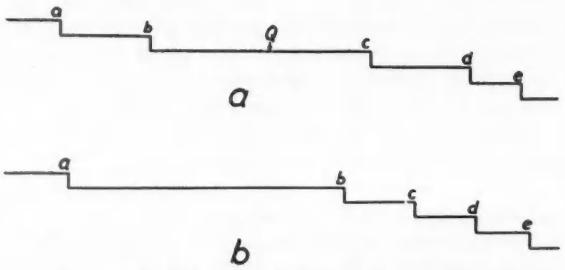


FIG. 13. Lateral propagation of steps on an interface.

The discussion so far relates to the formation of steps on a growing surface of a pure metal crystal. Let us consider a crystal of an impure metal, or an alloy, in which the solute is less soluble in the solid than in the liquid. Each advancing step generates a region of excess solute concentration which slows down the advance of the following steps. The effect of the solute is, therefore, to tend to keep the individual atomic sized steps equally spaced. Preliminary observations have shown that dilute solid solutions of this type solidify without the appearance of visible steps.

It will be noticed that we should not expect the "leading edge" of the large step to be sharp, because we do not expect the step *d*, for example, to disappear completely. It will presumably remain as a small step; thus the contour of the steps that will be present when a steady state has been reached will be as shown in Fig. 14. This is compatible with the photomicrographs shown in Figs. 4 and 7.



FIG. 14. Formation of visible steps.

Such a process would not be expected to take place when the angle is greater than about 16° (for this value of the angle, the distance between consecutive steps of the interface would be approximately four atomic diameters). At lower angles, the process becomes more probable. Hence, we expect steps of *unit* size at all angles greater than about 16°.

The position for the {001} face is qualitatively similar; quantitatively, it would seem that the critical angle should also be about 16°. The experimentally observed values of the transition angle are in both cases 15°–20°.

It is concluded that under the conditions we are considering, crystal growth takes place predominantly by edgewise growth on either {111} or {001} planes, from permanent re-entrant edges of the type envisaged by Chalmers and Martius (2); but that some nucleation of fresh layers can occur on the flat portions of the steps.

The next question is that of closed loops and superimposed layers. These occur where the solid–liquid interfaces are very close to the close-packed plane. The angle of tilt is then so small that there are very few, if any, re-entrants; especially if the surface is convex as on a cell (3), where a region may be exactly parallel to the {111} or {001} plane. Then the convex surface can only be maintained by nucleation and subsequent edge growth. Here



FIG. 15. Propagation of steps on a convex cell surface.

screw dislocations (especially in pairs) could be significant in locating the region at which new layers started. However, it is not necessary to assume the presence of a screw dislocation to explain the concentricity of the growth steps on a convex surface. The proposed mechanism is illustrated in Fig. 15: the initial convex surface is represented as a series of steps, in accordance with the scheme assumed above. Growth will take place by each step, which is a ring, growing outwards. The steps nearest to the center *A* will tend to group into large steps, and if the angle at the edge of the "dome" is large enough, there should be a structureless region. Nucleation of new layers on the flat region surrounding *A* is most likely to take place at the center *A* because this point

is furthest from the growth steps at which latent heat is being evolved. The growth of the rings does not, however, have to be symmetrical, because there will usually be a temperature gradient or a supercooling gradient across the plane region. This will cause the most probable site for nucleation to be shifted away from the center, which in turn will cause growth to be faster in one direction than the other. This may be associated with the "teardrop" effect shown on Figs. 6 and 10.

ACKNOWLEDGMENTS

This work was carried out in the Department of Metallurgical Engineering, University of Toronto. Financial assistance from the International Nickel Company of Canada is gratefully acknowledged.

REFERENCES

1. CHALMERS, B. Proc. Roy. Soc. (London), A, 175: 175. 1940.
2. CHALMERS, B. and MARTIUS, U. M. Phil. Mag. Ser. 7, 43: 686. 1952.
3. ELBAUM, C. and CHALMERS, B. J. of Metals, 5: 1081. 1953.
4. RUTTER, J. W. and CHALMERS, B. Can. J. Phys. 31: 15. 1953.
5. WEINBERG, F. and CHALMERS, B. Can. J. Phys. 29: 382. 1951.
6. WINEGARD, W. C., MAJKA, S., THALL, B. M., and CHALMERS, B. Can. J. Chem. 29: 320. 1951.

THE PULSE HEIGHT DISTRIBUTION FROM A SODIUM IODIDE SINGLE CRYSTAL SCINTILLATION COUNTER AND THE MEASUREMENT OF GAMMA RAY FLUXES[1]

By G. M. Griffiths[2]

ABSTRACT

The theory of the interaction of gamma rays with a single crystal of sodium iodide is described and a comparison made between the pulse height distributions, calculated on the basis of primary interactions only, together with the broadening due to the statistics of light production and electron multiplication, and the experimentally measured distributions. The differences are qualitatively accounted for on the basis of secondary interactions, bremsstrahlung, and wall effects. The absolute efficiency of a scintillation counter, calculated from the size and volume and energy corresponding to the bias level of the counting system, has been used to compute the intensity of gamma radiation from a standardized source of Co^{60} and from the reaction $Li^7(p, \gamma)Be^8$, the yield of which was known from previous work. Good agreement was obtained after allowance was made, experimentally, for the secondary interactions.

INTRODUCTION

The technique of gamma ray spectroscopy using scintillation counters with thallium activated sodium iodide as a scintillation phosphor, as introduced by Hofstadter (10), is well known and several reviews of the subject (1, 4, 5, 11) have appeared. The spectrum of gamma rays from radioactive materials and from nuclear reactions at low bombarding energies may be conveniently divided into three regions: low energies up to 1.0 Mev.; intermediate energies from 1.0 to 5 Mev.; and high energies, from 5 Mev. to 20 Mev. The work to be described concerns the resolution obtainable and the absolute measurement of γ-ray flux in the latter two regions of the spectrum to which less attention has hitherto been paid.

INTERACTIONS OF γ-RAYS IN SODIUM IODIDE

The cross sections for interaction of γ-rays with sodium iodide are shown in Fig. 1. Contributions from pair production in the field of atomic electrons and from the thallium impurity in the sodium iodide (from 0.1 to 0.4%) have been neglected since together they are less than 1% of the total absorption for 20 Mev. γ-rays. For the low energies the photoelectric effect, τ, gives the major contribution to the total absorption cross section, μ, while for intermediate energies the Compton effect, σ, predominates and for high energies the pair production process, κ, predominates. Each interaction process releases electrons from the sodium iodide with a characteristic energy distribution and the combination of crystal and photomultiplier produces a corresponding electrical pulse height distribution which can be analyzed by means of a differential pulse height analyzer or "kicksorter". If only primary interaction processes are considered, the photoelectric effect gives a "line" spectrum corresponding

[1]*Manuscript received September 1, 1954.*
Contribution from the Department of Physics, University of British Columbia, Vancouver, British Columbia.
[2]*Now at the Cavendish Laboratory, Cambridge, England.*

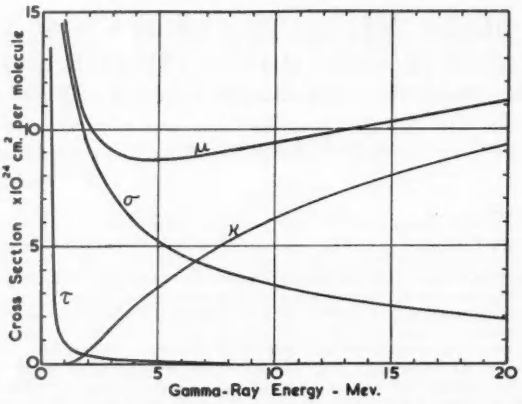


FIG. 1. Cross sections for the absorption of γ-rays in sodium iodide: τ—photoelectric, σ—Compton, κ—pair production, μ—total. The absorption coefficient in cm.$^{-1}$ equals 14.7×10^{21} times the molecular cross section.

to the full γ-ray energy $h\nu$, assuming that no X-rays escape from the crystal. The pair production process gives a second line at $h\nu - 2mc^2$ and the Compton process gives a broad distribution with a sharp upper limit according to the usual Klein–Nishina formula, which may be written in a convenient form for calculation as

$$\frac{d\sigma}{dE} = \frac{\pi r_0^2}{mc^2} \cdot \frac{1}{\alpha^2}\left\{1+\left(\frac{\alpha^2-\beta(1+\alpha)}{\alpha(\alpha-\beta)}\right)^2+\frac{\beta^2}{\alpha(\alpha-\beta)}\right\},$$

where $d\sigma/dE$ = the number of Compton electrons per target electron per Mev. with energies between E and $E+dE$,

$\alpha = h\nu/mc^2$ = the γ-ray energy in units of mc^2,

$\beta = E/mc^2$ = the electron energy in units of mc^2,

$mc^2 = 0.5108$ Mev., the electron rest energy,

$r_0 = 2.818 \times 10^{-13}$ cm., the classical electron radius, and

$\beta \leqslant 2\alpha^2/(1+2\alpha)$, the upper limit of the Compton electron distribution.

The above theoretical distributions are broadened by the finite resolution of the apparatus resulting from the statistics of the light production and photomultiplier operation and from inhomogenieties of the crystal and photocathode. At low and intermediate energies the "line" shapes are roughly Gaussian and the resolution can be represented by (15)

$$\frac{\Delta E}{E} = \frac{4}{3}\sqrt{\frac{1}{nE}+\rho^2}$$

where E = the energy of the line under consideration,

ΔE = the half width of the line at 60% of its height

= the standard deviation of the Gaussian shape,

n = a constant, which can be interpreted as the number of photoelectrons released from the photocathode per unit energy expended in the phosphor,

ρ = a constant which is dependent on sources of broadening other than the statistics.

For γ-ray energies from 0.5 to 6 Mev. and for sodium iodide crystals with diffuse reflectors of magnesium oxide powder mounted on E.M.I. 6262 photomultipliers, the constant parameters were found to have the following approximate values, $n = 1100$ photoelectrons per Mev. and $\rho = 0.026$. For high energy γ-rays the line shapes are no longer Gaussian but have more counts on the low energy side than on the high energy side for reasons that are discussed below.

SECONDARY INTERACTIONS

Experimentally observed spectra differ considerably from those expected on the basis of the primary interaction processes discussed above; the extent of the differences depends on the size of the scintillation crystal and the γ-ray energy. This can be accounted for by considering the following secondary interactions which take place in the crystals:

(*a*) At low energies in small crystals X-rays may escape following photoelectric capture of γ-rays resulting in lower energy "escape peaks" (18).

(*b*) Scattered quanta following Compton events may be captured thus moving counts from the primary Compton electron spectrum to higher energy regions of the spectrum. In particular, counts from the upper or high energy edge of the electron spectrum, corresponding to readily absorbable soft scattered quanta, are shifted to the full energy peak. This effect is readily noticeable for low energy γ-rays but for higher energies it may be obscured by effect (*c*).

(*c*) Following pair production and the absorption of the kinetic energy $h\nu - 2mc^2$ in the crystal the positron annihilates producing two 0.51 Mev. quanta, one or both of which may be captured. If one is captured in the crystal, counts are shifted from the pair peak at $h\nu - 2mc^2$ to a new peak at $h\nu - mc^2$ and, if both are captured, counts are shifted from the pair peak to the full energy peak at $h\nu$. Thus pair production events may contribute to three different peaks in the spectrum.

(*d*) For high energy γ-rays pair production releases fast electrons in the crystal and these lose part of their kinetic energy by the emission of bremsstrahlung radiation, some of which escapes from the crystal causing a loss of resolution and an asymmetric line shape.

(*e*) For high energy γ-rays the escape of electrons from the sides and ends of the crystal reduces the resolution and contributes further to an asymmetric line shape.

The importance of bremsstrahlung (*d*) and wall effect (*e*) as a function of γ-ray energy and crystal size can be estimated from the curves of Fig. 2 showing the range and percentage energy loss by radiation for electrons in sodium iodide as a function of electron energy. These curves were obtained by numerical integration of the theoretical results given in Heitler's book (9) (pp. 217 to 223). The curves show that a 10 Mev. electron in sodium iodide has a range of about 1.6 cm. so that an appreciable number of such

electrons formed uniformly throughout a moderate sized crystal escape, producing a tail on the low energy side of the spectrum. Also a 10 Mev. electron in sodium iodide loses approximately 20% of its energy in the form of radiation and, by considering the bremsstrahlung spectrum given by Heitler (9) (p. 170) and the absorption coefficient of γ-rays in sodium iodide

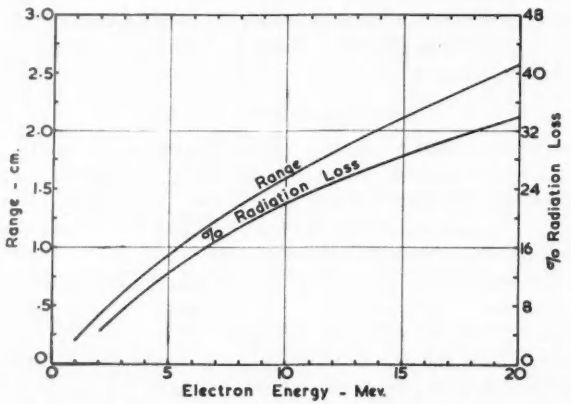


FIG. 2. Range, left-hand scale, and percentage energy loss by bremsstrahlung, right-hand scale, for electrons in sodium iodide.

(Fig. 1), it can be seen that in crystals with dimensions of the order of two inches as much as 60% of the bremsstrahlung radiation finally escapes from the crystal.

The influence of these secondary events on the resulting spectrum shape has been thoroughly discussed for the low energy region by Maeder, Muller, and Wintersteiger (14) and by Liden and Starfelt (12). An attempt has been made by Campbell and Boyle (3) to compute the shape at higher energies using a Monte Carlo method.

SINGLE CRYSTAL RESULTS

Fig. 3 shows the theoretical electron energy distribution produced in sodium iodide by 2.62 and 6.6 Mev. γ-rays. These curves were calculated assuming primary interaction processes and using the resolution function and parameters given above. κ indicates the contribution from pair production, τ that from the photoelectric effect and marks the "edge" of the broad Compton spectrum. Fig. 4 shows experimental spectra obtained using a sodium iodide crystal 1.75 in. in diameter and 2.0 in. long mounted on an E.M.I. 6262 photomultiplier with a diffuse magnesium oxide powder reflector. The left-hand curve was produced by the 2.62 Mev. γ-rays of RdTh and the right-hand curve was produced by the γ-rays from the $D(p, \gamma)He^3$ reaction with 1.0 Mev. protons incident on a thin heavy ice target. A comparison of Figs. 3 and 4 shows clearly the effects of some of the secondary interactions mentioned

above. The figures at the peaks indicate the energies of the three pairs resulting from escape of both, one, or neither of the annihilation quanta. The lower portion of the 2.62 Mev. spectrum, not shown in Fig. 4, is entirely obscured by other γ-rays from the RdTh. Evidence for the reduced Compton edge is clearly shown. In the 6.5 Mev. spectrum only the three pair peaks are resolved

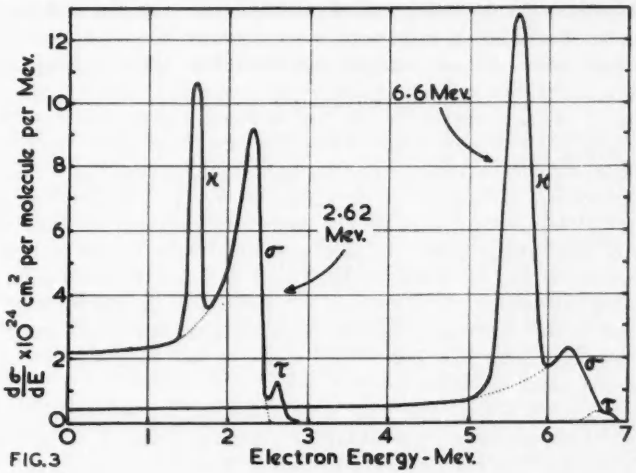


FIG. 3

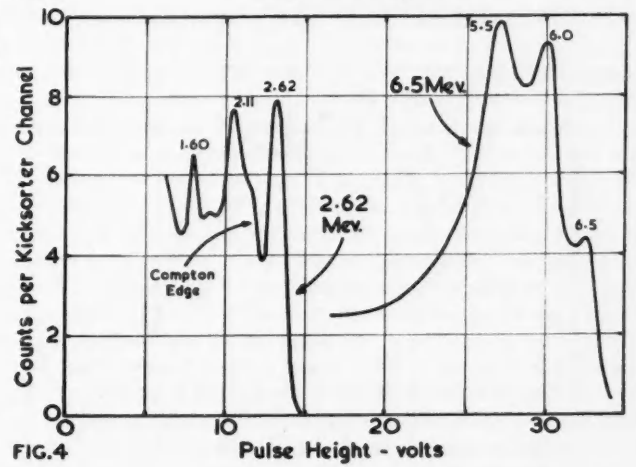


FIG. 4

FIG. 3. Theoretical electron spectra following primary interactions of 2.62 and 6.6 Mev. γ-rays in sodium iodide.

FIG. 4. Experimental single crystal scintillation counter spectra for 2.62 and 6.5 Mev. γ-rays. Arbitrary vertical scales, representing the number of counts per kicksorter channel, are given on all curves showing experimental spectra as these curves are generally composites of several runs.

and in this case the full energy peak is smaller relative to the other two peaks than in the RdTh case because there is less contribution to it from the Compton and photoelectric effects and, further, the 6.5 Mev. γ-rays were uncollimated whereas the 2.62 Mev. γ-rays were collimated into a beam about 1 cm. in diameter passing through the center of the crystal. The collimation has the result that most pair annihilations take place near the center of the crystal thus increasing the probability that both annihilation quanta will be captured. When the 2.62 Mev. γ-rays were not collimated the 2.62 and 1.60 Mev. peaks were nearly the same height and lower than the 2.11 Mev. peak. The 6.5 Mev. curve does not fall as low on the low energy side as expected from the theory owing partly to the effect of scattered radiation and partly to the bremsstrahlung and wall effects. The latter effects are much more serious at still higher energies, as indicated by the right-hand curve of Fig. 6, which shows the high energy portion of the spectrum from the 20.4 Mev. γ-rays of the $T(p, \gamma)He^4$ reaction incident on the same large sodium iodide crystal. The shape of this spectrum will be discussed more fully in the section on flux measurements. On the basis of the theory with primary interactions only, and using the resolution function given above with the parameters obtained from low and intermediate energy measurements, one would expect for 20 Mev. γ-rays a large pair line with a width at half height of about 1 Mev. plus a very small Compton tail.

The three peaks resulting from pair production by intermediate and high energy γ-rays are sometimes useful for positive identification of γ-rays and for making accurate energy comparisons. Fig. 5 shows the results of a measurement on the Doppler shift of the 6.5 Mev. γ-rays produced by the $D(p, \gamma)He^3$

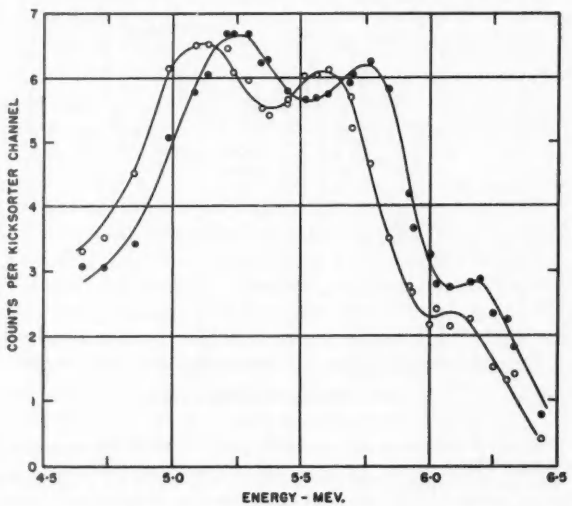


FIG. 5. $D(p, \gamma)He^3$ γ-ray spectra showing the Doppler shift.

reaction. Owing to the motion of the excited He^3 nuclei the energy of the emitted γ-rays is a function of the angle between the proton beam direction and the direction of motion of the γ-rays. For 1 Mev. incident protons the calculated shift in energy from 45° to 135° is 134 kev., assuming that the half life for the γ-ray emission is short compared to the slowing down time of the He^3 nuclei in the heavy ice target. The experimental value obtained from Fig. 5 is 130 ± 10 kev. The accuracy obtainable in such measurement is increased by having three peaks for each γ-ray energy. However, in the case of complex spectra the three peaks may introduce ambiguities.

γ-RAY FLUX MEASUREMENTS

In the past, measurements of the absolute intensities of γ-rays were difficult owing to the low intrinsic efficiency of the detectors and the difficulty of excluding the effects of scattered radiation (2, 7, 13). However, owing to the high efficiency, the energy resolution, and the well defined sensitive volume of the scintillation counter, considerable improvement is now possible. The absolute γ-ray efficiency of a scintillation counter can be calculated knowing the volume and density of the phosphor and the energy corresponding to the bias level of the associated electronic counting system, since both the cross section per molecule and the shape of the spectrum, after allowance is made (by experiment) for the secondary interactions, are known.

In order to determine the usefulness of the method, measurements have been made on the γ-rays of Co^{60} and the γ-rays from the $Li^7(p, \gamma)Be^8$ reaction. In each case the γ-ray intensity was known from previous work and so could be compared with the intensity by the scintillation counter method.

(*a*) *Co^{60}—1.17 and 1.33 Mev. γ-Rays*

For this measurement a small Co^{60} source was used which had been previously calibrated by a coincidence technique using two anthracene scintillation counters (8). Since the two cascade γ-rays of Co^{60} have almost the same energy it was not necessary to know the counter efficiencies in order to find the source strength. The source was found to give $(4.38\pm0.08)\times10^4$ disintegrations per second. This source was placed 25 cm. from the crystal (1 in. long by 1 in. in diameter) of a scintillation counter with the scaler discriminator set at a voltage equivalent to 0.65 Mev. energy loss in the crystal. This latter setting was determined by comparing the scaler reading with the number of counts in the spectrum as observed on the kicksorter, the energy scale of the kicksorter being defined by the positions of the peaks in the spectrum. The particular scaler bias used was chosen to include most of the pulses produced by direct interactions of the γ-rays in the crystal while excluding most of the pulses due to scattered quanta. From the counting rate obtained, the solid angle of the counter, and theoretical estimates of the absorption cross section and the number of Compton pulses below 0.65 Mev. which were not counted, the source strength was estimated to be $(4.42\pm0.20)\times10^4$ disintegrations per second in good agreement with the above value. The apparatus is essentially simple once a kicksorter is available. It is suggested that greater attention to details would result in better accuracy than given by the above error which

is based on estimates of the errors resulting from an unknown number of transfers of pulses across the 0.65 Mev. bias due to secondary interactions following Compton scattering and from an unknown amount of scattering in the crystal holder. Backscattered quanta from the photomultiplier were almost entirely of energies below the 0.65 Mev. bias level. The reproducibility of results taken with the source at different distances, and the statistical counting errors were both smaller than the error quoted above.

(*b*) *$Li^7(p, \gamma)Be^8$—17.6 and 14.8 Mev. γ-Rays*

For these high energies, flux measurements are difficult owing to the large distortion of the spectrum produced by bremsstrahlung and wall effects. It is impossible to choose a bias level past which there is not a large transfer of pulses due to these effects. However, an attempt has been made to estimate γ-ray intensities from the above reaction by making certain empirical assumptions concerning the shape of the spectrum in those lower energy regions where the true shape is obscured by scattered and bremsstrahlung radiation produced both inside and outside the crystal.

The $Li^7(p, \gamma)Be^8$ reaction gives two γ-rays: a sharp line with an energy about 17.6 Mev. and a broad line (± 1 Mev.) with a mean energy of 14.8 Mev. (17). For 0.5 Mev. protons the angular distribution of the γ-rays is isotropic (16) and, at the resonance proton energy of 441 kev., the ratio of the number of 14 Mev. to 17 Mev. γ-rays is 0.5 (6). The ratio increases with increasing proton energy and is 1.5 for a thick metal target and 1.15 Mev. protons (17). The excitation function and yield have been measured by Fowler and Lauritsen (6) who give the yield as 2.6×10^{-8} γ-rays per proton for 0.85 Mev. protons on a thick metal target.

For the present measurements an evaporated lithium metal target 250 kev. thick was bombarded with 550 kev. protons and a counter with a cylindrical sodium iodide crystal 2.0 in. long by 1.75 in. diameter, placed 67.5 cm. from the target, was used to record the spectrum shown by the left-hand full line curve in Fig. 6. In order to separate this spectrum into its two components the spectrum of the 20.4 Mev. γ-rays from the $T(p, \gamma)He^4$ reaction was plotted, as shown by the right-hand curve in Fig. 6, and this was used as a guide to the shape of the "sharp" 17.6 Mev. component which was then subtracted from the left-hand curve giving the shape of the 14.8 Mev. component.

It was necessary to extrapolate all the curves to zero pulse height in order to estimate the fraction of the counts in each component lying above the bias level, so that this fraction could be combined with the total cross section for each γ-ray energy to obtain the counter efficiency for each component. The extrapolation to zero pulse height for the 20.4 Mev. curve, as shown in Fig. 6, is based on the fact that below about 15 Mev. a portion of the experimentally observed counts is due to scattered and bremsstrahlung quanta, as proved by placing a lead block near the counter and observing an increase in the counting rate below 15 Mev.

In order to establish a low energy point on the "true" curve through which to extrapolate, an approximate estimate was made of the percentage of the total number of 'genuine' counts per unit energy interval at 2 Mev.

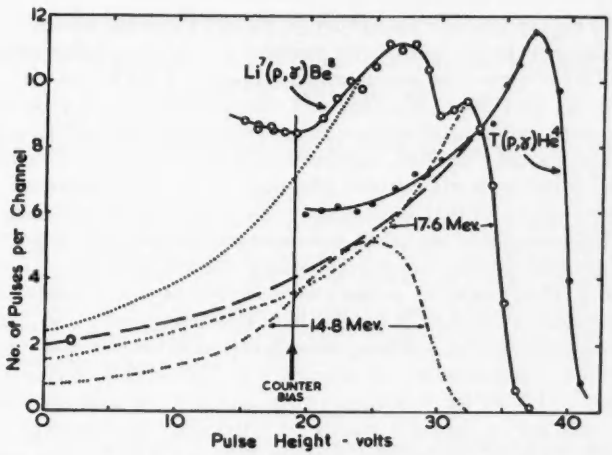


FIG. 6. γ-Ray spectra from the reactions $Li^7(p, \gamma)Be^8$, left-hand full curve, and $T(p, \gamma)He^4$, right-hand full curve. The broken lines show extrapolations of the curves to zero pulse height and the separation of the $Li^7(p, \gamma)Be^8$ spectrum into its two components.

Events, which arise within the crystal, but which leave only 2 Mev. energy in the crystal, may be classified under three headings: close-to-the-wall events in which electrons are formed in the crystal near the edges, particularly near the face farthest away from the incident beam, amounting to $1.0\, dE\%$; Compton events where an 18 Mev. scattered quantum escapes from the crystal, $0.36\, dE\%$; and those events in which an electron, or electron pair, formed in the crystal emits 18 Mev. of energy as bremsstrahlung all of which escapes from the crystal, amounting to less than $0.02\ dE\%$. Thus only about $1\frac{1}{2}\%$ of the total number of 'genuine' counts are expected to appear in a 1 Mev. band at 2.0 Mev. The numerical estimates were made using the relevant formulae from Heitler's book and the expression given earlier in this paper for the differential cross section for the Compton effect. It was assumed that most of the relevant 18 Mev. Compton scattered quanta escaped from the crystal and that most of the electrons produced in the crystal moved in the forward direction parallel to the cylindrical axis, so that the major contribution from the wall effect arises from the region of the far face of the crystal. Again, only the two extreme cases for pair production (83% of the absorption at 20 Mev.) were considered: firstly, in which the electrons have the same energy and, secondly, in which one electron takes all or nearly all the energy.

An exact calculation of the fraction of pairs which between them emit all but 2 Mev. of their energy as radiation, when averaged over the energy distribution of the pairs, the energy distribution of the bremsstrahlung quanta, and the probability for their reabsorption, would be most complex; hence the choice of 2 Mev. at which to make an approximate estimation, for at this energy the bremsstrahlung effect is quite small and does not affect the result significantly. Moreover, it should be noted that the error in the total area

under the high energy spectrum is five or six times less than the error involved in the approximate estimate of the height of the tail at this low energy.

The 17.6 Mev. spectrum was extrapolated to zero pulse height with the same shape as the 20.4 Mev. spectrum and the complete $Li^7(p, \gamma)Be^8$ spectrum was drawn in, rather arbitrarily, with a similar shape, the difference between the two giving the 14.8 Mev. spectrum as shown. The "broad" character of the latter γ-ray is clearly evident. The ratio of the areas under the 14.8 and 17.6 Mev. spectra of 0.55 indicates a γ-ray ratio of 0.58 when the different absorption coefficients are taken into account, in good agreement with the results of other workers when bombarding energy and target thickness are considered. The fraction of pulses above the 10 Mev. bias level obtained by graphical integration is 0.70 for the 17.6 Mev. component and 0.59 for the 14.8 Mev. component. Combining these figures with the theoretical efficiencies calculated by assuming that all primary interactions were counted, 0.557 for 17.6 Mev. and 0.538 for 14.8 Mev. γ-rays, and with the geometry factors and ratio of number of recorded counts to integrated beam current on to the target, the yield of the reaction is found to be 1.9×10^{-8} γ-rays per proton. In view of the arbitrariness of the extrapolation the estimated error for this result is $\pm20\%$. The yield for the present conditions, as estimated from thick target excitation function and yield measurement at 850 kev. given by Fowler and Lauritsen (6), is 2.1×10^{-8} γ-rays per proton. For these high energies greater accuracy could certainly be achieved with the single crystal scintillation method by using a considerably larger crystal.

ACKNOWLEDGMENTS

It is a pleasure to acknowledge the receipt of National Research Council of Canada and Ontario Research Council Fellowships during the period when this work was performed and further to acknowledge the help of my wife who carried out most of the numerical computations involved. Also, I am particularly indebted to Dr. J. B. Warren whose interest and helpful discussions were an invaluable guide to the progress of this work.

REFERENCES

1. Birks, J. B. Scintillation counters. Pergamon Press, London. 1953.
2. Bradt, H., Gugelot, P., Huber, O., Medicus, H., Preiswerk, P., and Scherrer, P. Helv. Phys. Acta, 19: 77. 1946.
3. Campbell, J. G. and Boyle, A. J. F. Australian J. Phys. 7: 171. 1953.
4. Curran, S. C. Luminescence and the scintillation counter. Butterworths Scientific Publications, London. 1953.
5. Curran, S. C. Advances in Phys. (Phil. Mag. Quarterly Suppl.), 2: 411. 1953.
6. Fowler, W. and Lauritsen, C. Phys. Rev. 76: 314. 1949.
7. Fowler, W., Lauritsen, C., and Lauritsen, T. Revs. Mod. Phys. 20: 236. 1948.
8. Griffiths, G. Phys. Rev. 83: 852. 1951.
9. Heitler, W. The quantum theory of radiation. 2nd ed. Oxford University Press, London. 1947.
10. Hofstadter, R. Phys. Rev. 74: 100. 1948.
11. Jordan, W. Annual review of nuclear science. Vol. 1. Annual Reviews, Inc., Stanford, California. 1952. p. 207.
12. Lidén, K. and Starfelt, N. Arkiv Fysik, 7: 427. 1954.
13. McDaniel, B., Walker, R., and Stearns, M. Phys. Rev. 80: 807. 1950.
14. Maeder, D., Muller, R., and Wintersteiger, V. Helv. Phys. Acta, 27: 1. 1954.
15. Roberts, P. Proc. Phys. Soc. (London), A, 66: 192. 1953.
16. Stearns, M. and McDaniel, B. Phys. Rev. 82: 450. 1951.
17. Walker, R. and McDaniel, B. Phys. Rev. 74: 315. 1948.
18. West, H., Meyerhof, W., and Hofstadter, R. Phys. Rev. 81: 141. 1950.

THE PULSE HEIGHT DISTRIBUTION FROM BORON TRIFLUORIDE PROPORTIONAL COUNTERS IRRADIATED WITH 4.87-MEV. NEUTRONS[1]

By D. B. James,[2] W. Kubelka,[3] S. A. Heiberg,[4] and J. B. Warren

ABSTRACT

Two boron trifluoride proportional counters, one containing normal isotopic boron and the other containing boron enriched to 96% B^{10}, have been irradiated with 4.87-Mev. neutrons from the reaction $D(d, n)He^3$. In addition to the reactions $B^{10}(n, \alpha)Li^7$ and $B^{10}(n, \alpha)Li^{7*}$ with Q-values of 2.79 Mev. and 2.31 Mev. respectively, two other reactions have been observed. These are (i) $F^{19}(n, \alpha)N^{16*}$ with a Q-value of -1.77 ± 0.15 Mev. and (ii) either $B^{10}(n, p)Be^{10}$ or, much more probably, $B^{10}(n, t)Be^8$ with a Q-value of 0.35 ± 0.20 Mev. Owing to the presence of these two reactions, the analysis of complex fast-neutron spectra by the use of such counters is not feasible.

INTRODUCTION

While boron trifluoride counters have been used extensively for the detection of neutrons, no attempt has been made to use them as neutron spectrometers. We have irradiated two proportional counters, one containing normal isotopic boron and the other containing boron enriched in B^{10}, with 4.87-Mev. neutrons to determine whether or not such counters might be used to measure fast neutron energies. It was thought possible that, if no reaction other than $B^{10}(n, \alpha)Li^7,Li^{7*}$ played any significant role, then the efficiency and resolution of a counter filled with 60 cm. of boron trifluoride might be adequate for it to be used as a fast-neutron detector and energy spectrometer.

The reaction $B^{10}(n, \alpha)Li^7,Li^{7*}$ has been studied by many workers (1). The branching ratio for the formation of lithium in the ground state and in the first excited state has been measured as a function of the neutron energy from thermal energies up to 4 Mev. The ratio rises monotonically from 0.06 at thermal energies (2, 3, 5, 9) to 2.3 at E_n 1.9 Mev., and falls to 0.8 at 2.6 Mev. (8). The Q-value of the reaction $B^{10}(n, \alpha)Li^7$ is 2.79 Mev., and it branches to the first excited state of Li^7 at 478 kev. (1).

EXPERIMENTAL

The counters used in the experiment were supplied by Atomic Energy of Canada, Ltd., and were designed for use as long counters (6). They consisted of copper cathodes, 1 in. in diameter, with tungsten wire anodes, the active length being restricted to 33 cm. by means of grounded guard rings. One counter was filled with normal boron trifluoride (19% B^{10}, 81% B^{11}) and the other with boron trifluoride enriched in B^{10} (96% B^{10}, 4% B^{11}), at a pressure of about 60 cm. of mercury.

[1]*Manuscript received December 20, 1954.*
Contribution from the Department of Physics, University of British Columbia, Vancouver, British Columbia.
[2]*Bell Telephone Laboratories, Murray Hill, New Jersey, U.S.A.*
[3]*Canadian Westinghouse Company, Toronto, Ontario.*
[4]*Defence Research Board, Suffield, Ralston, Alberta.*

The counters were operated at a potential of 1850 volts, with a gas amplification of approximately 30.

In Fig. 1 the target and counter assembly is shown. The counters were housed in 1/16-in.-thick brass tubes and wrapped in 0.040-in. cadmium sheet to reduce the number of events due to scattered slow neutrons.

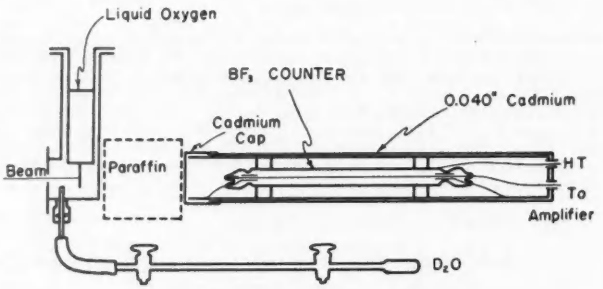


FIG. 1. Target and counter assembly.

The neutrons from the $D(d, n)He^3$ reaction, which has a Q-value of 3.26 Mev. (11), were generated by allowing 1.67-Mev. deuterons accelerated by the U.B.C. Van de Graaff generator to impinge on a heavy-ice target about 30 kev. thick. The target was prepared using the dispenser shown in Fig. 1. First the tap nearest to the heavy-water container was opened, allowing the vapor from the water to reach equilibrium pressure (17 mm. of mercury at 20°C.). The tap was then closed and the second tap opened, allowing 5 cc. of heavy-water vapor to be ejected through a very small hole onto a copper target plate, cooled by liquid oxygen. The process was repeated until the required target thickness was obtained.

The target thickness produced in this manner was standardized experimentally by the measurement of the shift of the 873.5-kev. $F^{19}(p, \alpha\gamma)O^{16}$ resonance with a similar heavy-ice film laid down on a calcium fluoride target. The target thickness for 900 kev. deuterons was then calculated and found to be 4 kev. $\pm 20\%$ for every 5 cc. of heavy-water vapor.

The pulses from the counter were amplified and analyzed with a 30-channel "kicksorter".

RESULTS

A 6-cm. paraffin moderator was placed between the target and the counter, and the cadmium cap was removed from the end of the counter to admit slow neutrons. The resultant slow-neutron pulse-height distribution, obtained with the B^{10}-enriched counter, is shown in Fig. 2. Two groups only can be seen. The first, corresponding to the reaction $B^{10}(n, \alpha)Li^{7*}$ for thermal neutrons (Q = 2.31 Mev.), was used to establish the energy calibration of the counter. The second and smaller group corresponds to the ground state transition (Q = 2.79 Mev.).

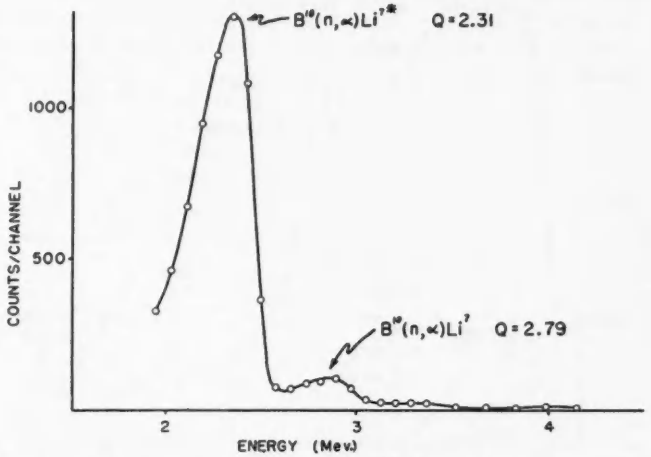


FIG. 2. Pulse-height distribution from the enriched boron trifluoride counter irradiated with slow neutrons.

The cadmium cap was replaced and the paraffin removed. The two counters were then irradiated in turn with 4.87-Mev. monoenergetic neutrons from the $D(d, n)He^3$ reaction using 1.67-Mev. deuterons. The neutron flux was monitored by another enriched counter embedded in paraffin in the manner described by Hanson *et al.* (6). The resultant pulse-height distributions are shown in Fig. 3 and Fig. 4. Six groups were observed:

(1) at 2.31 Mev. corresponding to the reaction $B^{10}(n, \alpha)Li^{7*}$ with slow neutrons (Fig. 3 and Fig. 4);

(2) at 2.79 Mev. corresponding to the reaction $B^{10}(n, \alpha)Li^7$ with slow neutrons (Fig. 3);

(3) at 7.2 Mev. corresponding to the reaction $B^{10}(n, \alpha)Li^{7*}$ with 4.87-Mev. neutrons (Fig. 3);

(4) at 7.7 Mev. corresponding to the reaction $B^{10}(n, \alpha)Li^7$ with 4.87-Mev. neutrons (Fig. 3);

(5) at 3.10 Mev. corresponding to a reaction with a Q-value of -1.77 Mev., induced by 4.87-Mev. neutrons (Fig. 3 and Fig. 4);

(6) at 5.22 Mev. corresponding to a reaction with a Q-value of 0.35 Mev., induced by 4.87-Mev. neutrons (Fig. 3 and Fig. 4).

The reacting nuclei from which groups (5) and (6) arose were identified from the relative yields of these reactions in the enriched and unenriched counters. The ratios of the abundances of B^{10}, B^{11}, and F^{19} in the two counters were 96: 19, 4: 81, and 1: 1 respectively. A comparison between these ratios and the observed yields of groups (5) and (6) in the two counters led to the assignment of group (5) to a reaction involving F^{19} and group (6) to a reaction involving B^{10}.

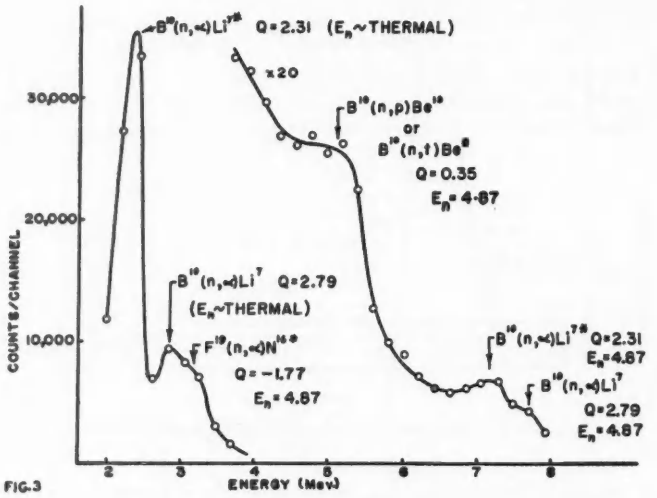


FIG. 3

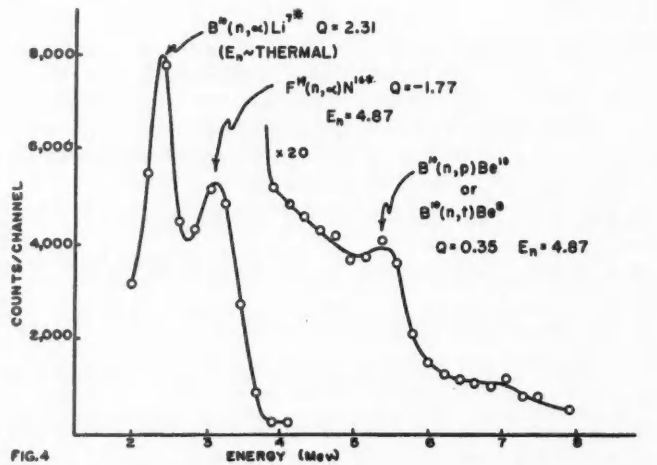


FIG. 4

FIG. 3. Pulse-height distribution from the enriched boron trifluoride counter irradiated with 4.87-Mev. neutrons.

FIG. 4. Pulse-height distribution from the unenriched boron trifluoride counter irradiated with 4.87-Mev. neutrons.

To determine the Q-value of group (5) more accurately, the region of the distributions from 2.5 Mev. to 4.0 Mev. was repeated with the kicksorter set at 80 kev. per channel, using the unenriched counter. The contribution of the two slow neutron groups, (1) and (2), was subtracted, using the data obtained by slow-neutron bombardment as for Fig. 2, and normalizing the amplitudes

of the $B^{10}(n, \alpha)Li^{7*}$ slow-neutron peak before subtraction. The resultant spectrum is shown in Fig. 5. A Q-value of -1.77 ± 0.15 Mev. was obtained from these data. The reaction responsible for this group is most probably $F^{19}(n, \alpha)N^{16}$, $Q_m = -1.4$ Mev. (1), since other neutron-induced reactions with F^{19} have much larger negative Q-values.

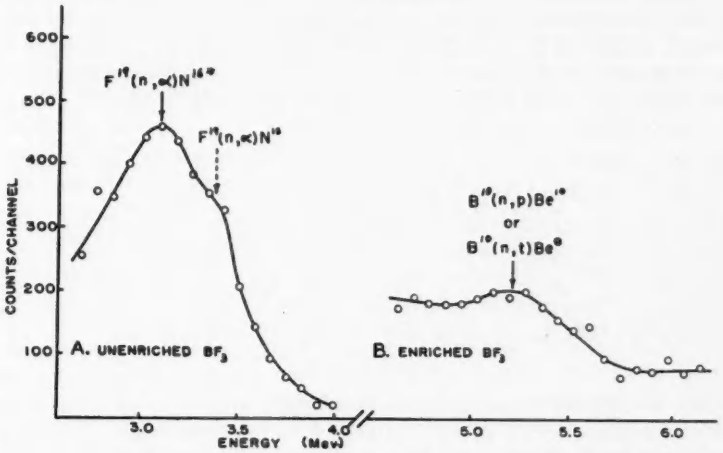


FIG. 5. *A*. Pulse-height distribution from the enriched boron trifluoride counter in the energy region 2.5 Mev. to 4.0 Mev. with the slow neutron contribution subtracted, showing the $F^{19}(n, \alpha)N^{16*}$ group, $Q = -1.77\pm0.15$ Mev.

B. Pulse-height distribution from the enriched counter in the energy region 5 Mev. to 6 Mev., showing the group corresponding to the $B^{10}(n, p)Be^{10}$ or $B^{10}(n, t)Be^{8}$ reactions, $Q = +0.35\pm0.20$ Mev.

If the Q-value of -1.4 Mev. derived from the masses is correct, it would indicate that, at a neutron energy of 4.87 Mev., most of the transitions go to an excited state of N^{16} about 340 kev. above the ground state. An excited state at 0.3 Mev. has been reported (12),* based on a study of the $N^{15}(d, p)N^{16}$ reaction. There is slight evidence of a group at $0.34\pm.12$ Mev. above the main group, which could correspond to the ground-state transition. The yield for this group is about 4% of that for the main F^{19} peak. If it is assumed to be due to the ground-state transition, the mass of N^{16} may be determined from the Q-value. The previous experimentally-determined values of this mass have shown large discrepancies (1). The Q-value of -1.43 ± 0.15 Mev. gives a value of 10.3 ± 0.2 Mev. for the $N^{16}-O^{16}$ mass difference, in good agreement with the value $N^{16}-O^{16} = 10.3\pm0.5$ Mev. adopted by Ajzenberg and Lauritsen on the basis of all the previous data bearing on the mass of N^{16}.

It should be noted that, if the reaction $B^{10}(n, \alpha)Li^{7*}$ proceeded via the 4.61 Mev. level in Li^7, then a group should appear in the counter giving an energy

**The reviewer informs us that according to Ajzenberg and Lauritsen, Boston University Progress Report No. 4, Appendix B, Sept. 30, 1954, there are three levels in N^{16} at excitations of 0.391, 0.295, and 0.115 Mev.*

release of 3.04 Mev. corresponding to a Q of -1.83 Mev. Such a group would tend to be obscured by the $B^{10}(n, \alpha)Li^7$ group arising from thermal neutrons and the fluorine reaction, and would probably not be recognized unless the cross section for such a transition was of the order of one-third of the cross section for the $F(n, \alpha)N^{16*}$ reaction.

A similar expanded pulse-height distribution in the region from 5 Mev. to 6 Mev. was obtained using the enriched counter. This spectrum is also shown in Fig. 5. It gives a Q-value of 0.35 ± 0.20 Mev. for the B^{10} reaction. In the case of this group, however, the reaction is not uniquely identified, since there are two reactions which could fit the experimental Q-value:

(i) $B^{10}(n, p)Be^{10}$, $Q_m = 0.226$ Mev. (1, 4);

(ii) $B^{10}(n, t)Be^8$,
$Be^8 \rightarrow 2\alpha$, Total $Q_m = 0.33$ Mev. (1, 7, 10).

However, it is unlikely that the products of the $B^{10}(n, p)Be^{10}$ reaction could expend 5.22 Mev. energy in the chamber in view of the fact that the range of the protons will be several times the diameter of the counter and comparable to its length. Other neutron-induced reactions in B^{10} yielding charged particles have Q-values that do not agree with the position of this group.

CONCLUSIONS

When boron trifluoride counters are bombarded with neutrons in the energy region of 5 Mev., several groups are present in the pulse-height distribution which have yields of the same order of magnitude as that of the group from the $B^{10}(n, \alpha)Li^7$ reaction. This makes the spectrum too complicated to be of use for the measurement of fast-neutron energies if several neutron-energy groups are present. The group at 5.22 Mev. is due probably to the reaction $B^{10}(n, t)Be^8$. The group at 3.10 Mev. is due to the reaction $F^{19}(n, \alpha)N^{16*}$, and has a Q-value of -1.77 ± 0.15 Mev.

ACKNOWLEDGMENTS

We are indebted to Mr. Fowler of Atomic Energy of Canada Ltd. for furnishing the three counters used. We are grateful to Atomic Energy of Canada Ltd. for financial assistance which made this work possible.

REFERENCES

1. Ajzenberg, F. and Lauritsen, T. Revs. Mod. Phys. 24: 321. 1952.
2. Bichsel, H., Halg, W., Huber, P., and Stebler, A. Phys. Rev. 81: 456. 1951.
3. Cuer, P. and Lonchamp, J. Compt. rend. 232: 1824. 1951.
4. Eggler, C., Hughes, D. J., and Huddleston, C. Phys. Rev. 74: 1239. 1948.
5. Hanna, G. C. Phys. Rev. 80: 530. 1950.
6. Hanson, A. O. and McKibben, J. L. Phys. Rev. 72: 673. 1947.
7. Perkin, J. L. Phys. Rev. 81: 892. 1951.
8. Petree, B., Johnston, C. H., and Miller, D. W. Phys. Rev. 83: 1148. 1951.
9. Rhodes, J., Franzen, W., and Stephens, W. E. Phys. Rev. 87: 141. 1952.
10. Ribe, F. L. and Seagrave, J. D. Phys. Rev. 94: 934. 1954.
11. Tollestrup, A. V., Jenkins, F. A., Fowler, W. A., and Lauritsen, C. C. Phys. Rev. 76: 181. 1949.
12. Wyly, L. Phys. Rev. 76: 316. 1949.

FERROMAGNETIC DOMAIN PATTERNS ON SINGLE CRYSTALS AND BICRYSTALS OF NICKEL[1]

By Ursula M. Martius[2] and K. V. Gow[3]

ABSTRACT

Ferromagnetic domain patterns were studied on the (110), (112), and (001) planes of single crystals of nickel. The crystals were grown from seeds of predetermined orientation and no mechanical cutting was required prior to the observation of the domain patterns. The results are compared with data in the literature, existing discrepancies are pointed out and interpreted. The influence of grain boundaries on the domain patterns is shown in experiments with bicrystals.

INTRODUCTION

The first basic ferromagnetic domain patterns in pure nickel were observed in 1951, simultaneously and independently, by Martius, Gow, and Chalmers (8), and Yamamoto and Iwata (12). Earlier investigations (1, 7, 5) yielded only "maze" patterns, which are characteristic of strained surfaces and not representative of the basic domain structure of the crystal. Domain patterns on nickel are very sensitive to strains because the magnetostriction of nickel is large and the anisotropy energy is small. The strains introduced by cutting a single crystal, in order to expose magnetically interesting surfaces, are very difficult to remove and they may influence the observed domain patterns. To overcome this difficulty the crystals for the present investigation were grown from seeds of predetermined orientation. The orientations chosen were such as to make either (110) or (112) or (133) or (001) the plane of the top surface. No mechanical treatment prior to the observation of the domain pattern was then required. It is the purpose of this paper to describe and interpret the observed domain patterns and to compare them with data published recently by Yamamoto and Iwata (13), who used randomly grown nickel crystals and careful cutting, annealing, and polishing techniques to investigate patterns on (110), (112), (001), and (111). Discrepancies between the results of the two investigations are pointed out and the reasons for them are stated.

In addition, bicrystals of known orientation were investigated and some experimental evidence of the effect of grain boundaries on the domain structure of nickel is presented.

The experimental work reported in this paper was carried out in 1951 in the course of an investigation of the effect of crystal boundaries on the domain structure.

EXPERIMENTAL PROCEDURE

The method of preparation of single crystals and bicrystals of nickel with predetermined crystallographic orientation has been described elsewhere in

[1]*Manuscript received January 31, 1955.*
Contribution from the Ontario Research Foundation and the Department of Metallurgical Engineering, University of Toronto, Toronto, Ontario.
[2]*Ontario Research Foundation, 43 Queen's Park, Toronto 5, Ontario.*
[3]*Department of Metallurgy, University of Toronto, Toronto, Ontario.*

detail (4). Fig. 1(*a*) shows a plane view of a bicrystal; Fig. 1(*b*) its cross section. The single crystals were of similar dimensions. The crystals were grown into the melt while surrounded by an argon atmosphere. Subsequently they were given a brief electropolish to remove traces of oxide from the surface. The electrolyte was composed of 390 ml. of concentrated sulphuric acid and 290

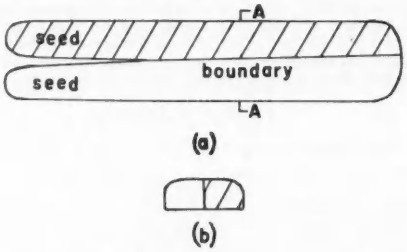


FIG. 1. (*a*) Plan of a bicrystal.
(*b*) Cross section through A–A of a bicrystal. $\frac{1}{2}\times$.

ml. of distilled water. A current density of 39 amperes per square decimeter was used. The specimen was wrapped in electroplating tape, an area of about 1 to 2 cm.^{2} on the top surface being left exposed for polishing.

The domain structure was investigated by means of the ferromagnetic colloid technique (11). The liquid used* contained a colloidal suspension of magnetite with a particle size of the order of one micron. Powder patterns were formed by placing a droplet of the colloidal suspension on the electropolished surface and then placing a thin microscope cover glass on the drop so that a thin layer of the colloidal suspension was spread over the crystal by the cover glass. The domain pattern could be observed immediately or the cover glass could be removed and the suspension allowed to dry. Both liquid and dry patterns were investigated.

The powder pattern was examined under an ordinary metallographic microscope. The surface illumination technique proved to be a critical factor in revealing clearly the domain structure. Dark field illumination was obtained by careful adjustment of a separate microscope lamp so that the light beam struck the specimen obliquely. Vertical illumination was quite unsatisfactory and Ultrapak dark field vertical illumination was also less satisfactory than the type of oblique illumination used.

The crystallographic orientations of the surfaces under investigation were determined by Laue back-reflection X-ray photographs and plotted in stereographic projections. The plane of the projection is the top surface of the crystal, i.e. the surface on which the domain photograph was taken. The direction of the specimen axis (denoted by DE), the (011) pole closest to the pole of the top surface, and the (111) poles are marked in the projections. These data completely describe the orientation of the crystal under observation

*A gift of the Bell Telephone Laboratories.

and give the angles which the octahedral ⟨111⟩ form with the top surface and the side faces of the crystal as well as with the possible plane of the Bloch walls. (On the stereographic projection the basic circle is the trace of the plane of the top surface and the line *DE* is the trace of the planes of the long side faces of the crystal.)

The presentation of crystallographic orientations on a stereographic projection is used in preference to the more common method of indicating the direction of easy magnetization in or close to the surface by means of arrows on the photographs. Because only on the basis of a stereographic projection is it possible to visualize the orientation of the whole crystal and the three-dimensional domain arrangement. It is considered well worth while to go through the slightly more time consuming process of reading a stereographic projection in order to avoid the danger of serious misinterpretation which lies in the "two-dimensional" approach.

In nickel, the ⟨111⟩ are the directions of easy magnetization along which the ferromagnetic domains are magnetized. A Bloch wall separates domains of different magnetization and 70°32′, 109°28′, and 180° walls can occur. It is known from the study of magnetic domains that the normal component of the magnetization is continuous across the Bloch wall (9) and this condition specifies the type of crystallographic plane that can be a Bloch wall. In nickel only {*ohl*} and {*hhl*} type planes occur, since only their normals form equal angles with the magnetization vector on either side of the wall and thus fulfill the above conditions.

In Table I the Bloch wall energies for the most prominent walls in nickel are compiled from the extensive calculations of Lilley (6).

γ denotes the wall energy per unit area.

γ_0 is a unit for the wall energy per unit area and can be estimated for nickel to be approximately 0.14 ergs/cm.^{2}

TABLE I

REDUCED ENERGIES γ/γ_0 OF DOMAIN BOUNDARIES IN NICKEL

Type of boundary	Direction of normal to boundary			
	[001]	[110]	[111]	[112]
70.53°	0.5443	0.4611	—	—
109.47°	1.0887	1.3680	1.2903	—
180°	—	2.19	—	2.27

In our investigations the type of domain boundary was determined both from the crystallographic orientation of the trace of the Bloch wall on the surface under observation and from the behavior of the walls under liquid colloid in a weak magnetic field in the plane of the surface.

EXPERIMENTAL RESULTS

In growing the single crystals and bicrystals for these experiments the following orientation relationships were chosen:

(1) Crystals with two octahedral directions as close to the plane of the top surface as possible and no octahedral directions in or close to the plane of the long side faces. Crystals of this orientation will yield the most straightforward domain structures, corresponding to most theoretical models.

(2) Crystals with increasing deviation of the two directions of easy magnetization from the plane of the top surface; however, the deviation was still smaller than the angle of the other octahedral directions with the planes of the side faces.

(3) Crystals with one or two octahedral directions in or close to the planes of the long side faces.

Fig. 2 shows a typical example of a domain pattern of a crystal with two directions of easy magnetization close to the plane of the top surface. Both the $[1\bar{1}1]$ and $[\bar{1}\bar{1}1]$ form angles of 2° with the plane of the top surface. The crystal consists of large slablike domains with 180° walls, parallel to $(2\bar{1}1)$ planes, between them. The "free magnetic charges" on the top surface, which result from the fact that the directions of easy magnetization are not exactly in the plane of the surface, are reduced by the formation of a "tree pattern". Fig. 9 shows a pattern of the same orientation over a larger area and it can be noted there that the "branches" attain only a certain size and tend to subdivide or to form secondary branches rather than to grow larger. It is also typical that the "35° branches" are fewer in number and individually larger than the "55° branches". This behavior has been observed often on "tree patterns" of nickel and can be explained by the relatively small wall energy of nickel (compared to iron or cobalt).

A greater deviation of the directions of easy magnetization from the plane of the top surface increases the above-mentioned tendency for divisions within the "branches" of the tree patterns. This is shown in Figs. 3 and 4 where the $[1\bar{1}1]$ and $[\bar{1}\bar{1}1]$ directions of the specimen form angles of 2° and 5° respectively with the plane of the top surface, as can be seen from the stereographic projection. The crystallographic directions of the spikes and of their subdomains in Figs. 3 and 4 are the same as in Fig. 2 and the type of domain pattern is the same too. We have to picture the whole crystal as built up of slablike basic domains (their 180° walls, which are $(2\bar{1}1)$ planes, can be seen on the original photographs but did not come out on the sections printed in Fig. 3), with a tree-type domain pattern on the top surface. Some type of closed-flux configuration will exist on the long side faces of the crystal, where the two closest $\langle 111 \rangle$ directions are 18° and 23° respectively off the plane of the side faces. In the domain pattern shown in Fig. 5 the $[1\bar{1}1]$ and $[\bar{1}\bar{1}1]$ directions of the crystal are each 10° off the plane of the top surface. The basic domains are clearly visible in Fig. 5 as light and dark strips, the domain walls are $(0\bar{1}1)$ planes. The enlargement of the pattern in Fig. 6 shows the very fine surface structure which can be interpreted as resulting from the "free magnetic charges" on the surface. The fact that the $[1\bar{1}1]$ and $[\bar{1}\bar{1}1]$ directions form approximately equal angles with the plane of the surface can explain the symmetry of the surface pattern. The $[\bar{1}11]$ and [111] are 20° and 50° respectively off the plane of the long side faces.

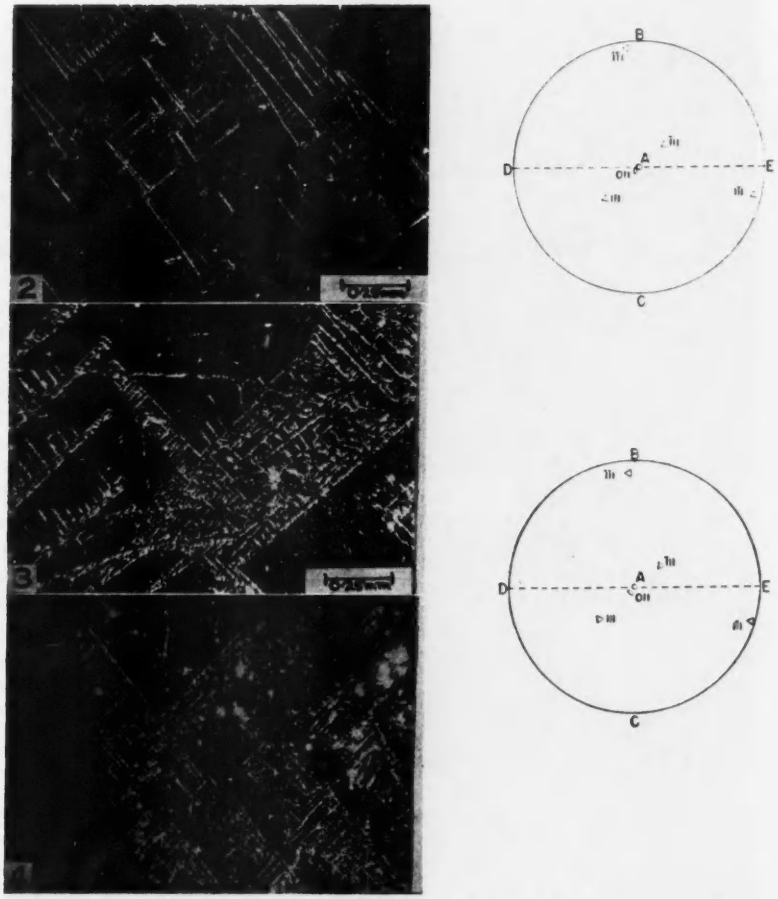


FIG. 2. Domain pattern on a nickel crystal with (011) tilted about 2° from the plane of the surface.

FIG. 3. Domain pattern on a nickel crystal with (011) tilted about 5° from the plane of the surface.

FIG. 4. Domain pattern near location at which Fig. 3 was observed; same scale as Fig. 3.

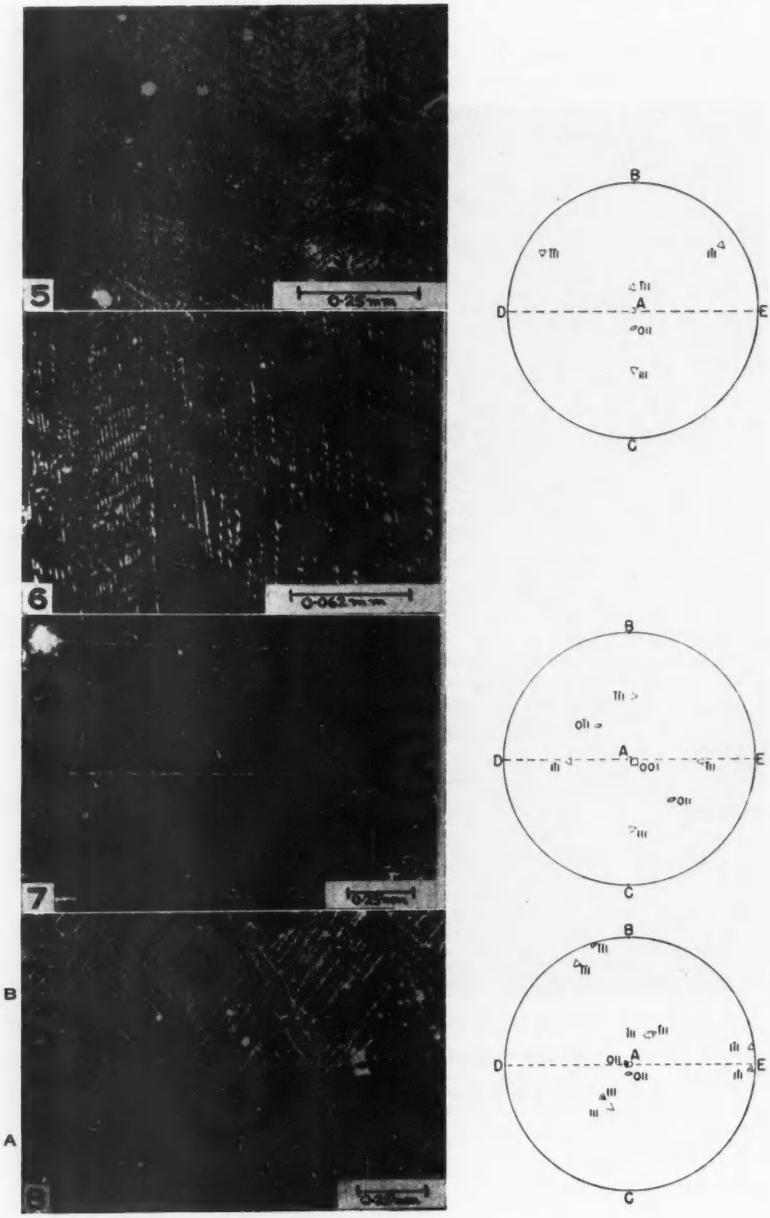

5
0·25 mm
6
7
B
A
B
D
E
A
C
B
D
E
A
C
B
D
E
A
C

Fig. 7 illustrates the case of a crystal in which two directions of easy magnetization are very close (within 1°) to the plane of the long side face. The plane of the surface is close to (001) and the crystal is built up of basic slablike domains, aligned parallel to the long side faces with ($\bar{1}\bar{1}0$) domain walls between them. The traces of these domain walls on the plane of the top surface can be seen on Fig. 7; a fine irregular surface structure can be seen between the basic domain walls.

The domain patterns shown in Fig. 5, Fig. 6, and Fig. 7 are different from the domain patterns Yamamoto and Iwata (13) have published for crystal surfaces of the same orientation. This discrepancy can be in our opinion explained by the following consideration: In order to understand and interpret ferromagnetic domain patterns it is necessary to realize that any domain pattern observed on a given surface is evidence of the ferromagnetic domain structure of the *whole* crystal. This structure represents the domain configuration in which the total free energy of the crystal is a minimum. One factor which enters strongly into this energy balance is the magnetostatic energy of the domain arrangement. The domain arrangement will always be such that the "free magnetic charges" on the crystal surfaces will be as small as possible. *All* free surfaces of the crystal contribute and the pattern under observation may be influenced or determined by the magnetostatic contributions of surfaces of the crystal other than the one under observation. Consequently it is often not enough to base the interpretation of a domain pattern only on the crystallographic orientation of the surface under observation as was done in (13). Especially in the case of surfaces which do not have one or two directions of easy magnetization in or close to the plane of the surface will the observed domain structure strongly depend on the crystallographic orientation of the other free surfaces. Fig. 7, for instance, should be regarded not as the prototype of a domain pattern on a (001) plane of a nickel crystal—there is no *one* such pattern—but as the evidence of the domain configuration of a nickel crystal of the above-given dimensions and of a crystallographic orientation as illustrated in its stereographic projection.

THE INFLUENCE OF GRAIN BOUNDARIES ON DOMAIN PATTERN OF NICKEL CRYSTALS

The preceding paragraphs showed the influence of the dimensions and the external surfaces of a crystal on the domain pattern observed on the top surface. We can also ask to what extent grain boundaries, i.e. internal surfaces, will affect the domain configuration. This depends, of course, on the relative orientation of the grains concerned. If possible, the domain structure will tend to be continuous across a grain boundary, or, if the difference in crystallographic orientation results in "free magnetic charges" at the grain boundary, these might be reduced through the formation of "spikes" while the basic

FIG. 5. Domain patterns on nickel crystal with (011) tilted about 10° from surface.
FIG. 6. Enlargement of domain patterns shown in Fig. 5.
FIG. 7. Domain pattern on a nickel crystal with surface close to (001).
FIG. 8. Domain patterns near a grain boundary of a nickel bicrystal.

domain arrangement in neighboring domains may remain similar (2, 3, 10). Here again the domain structure of a given grain will depend on the "free magnetic charges" on *all* the boundaries.

In addition to the effect of the difference in crystallographic orientation there may be an effect of internal stresses on the domain pattern, an effect similar to the effect of external stress on ferromagnetic domain configurations. In a future communication one of us will deal with the effect of stresses on domain pattern of nickel; in the following paragraphs we are concerned only with the effects of internal surfaces.

Fig. 8 shows the domain pattern along a grain boundary of a bicrystal of nickel at a point at which a small stray crystal had nucleated. The photograph shows the pattern along the boundary between the stray crystal (*B*) and crystal *A* of the bicrystal. The orientations of both these crystals are shown in the stereographic projection in Fig. 8. Data of the stray crystal are denoted by dots in the projection. The (011) plane of crystal *A* is close to the plane of the top surface, while the (011) plane of the stray crystal is tilted by nearly 10° around the specimen axis. The $[\bar{1}\bar{1}1]$ direction of the stray crystal is rotated by 10° about the specimen axis, and tilted "up" by 5°. The $[1\bar{1}1]$ direction of the stray crystal is only 2° off the plane of the surface. On the basis of the orientation of the stray crystal alone one would expect to find a configuration consisting of domains magnetized along $[1\bar{1}1]$, since this is the direction of easy magnetization closest to the plane of the top surface. This would mean that the normal of the domain walls would be $[\bar{2}\bar{1}1]$. However, the domain photograph in Fig. 8 shows that the domain structure of the stray crystal (upper part of the photograph) tends to continue the pattern of crystal *A* (lower part of the photograph) consisting of domains magnetized along $[\bar{1}\bar{1}1]$ with the $[2\bar{1}1]$ normal to the domain boundary. The stray crystal shows a substructure which reduces the free magnetic charges resulting from the change in crystallographic orientation. It should be noted that the substructure reaches across the grain boundary into crystal *A*. One may have to take into account that the stray crystal may be shallow, with crystal *A* continuing underneath at a certain depth. This would increase the tendency of the stray crystal to fit as closely as possible into the domain configuration of crystal *A*, which consequently is the really determining factor of the domain structure of the stray crystal.

Fig. 9 shows another example of the influence of the internal surfaces. It shows again a bicrystal, but in this case a stray crystal that was growing along the bicrystal boundary is being encroached upon by the two main crystals. *ABC* is on the bicrystal boundary, *SSS* is the boundary between the crystals of the bicrystal and the stray. Crystal *A* has the same orientation as the crystal pictured in Fig. 2. Crystal *B* is rotated by 3° around the pole of the plane of the top surface with respect to crystal *A*, and it is tilted by 2° about the specimen axis. The stray crystal is situated between these two crystals (along only a part of the bicrystal boundary). Its boundary *SSS*, shown in Fig. 9, separates regions that are rotated around the specimen axis by 1–2° with respect to each other. These orientation differences were deter-

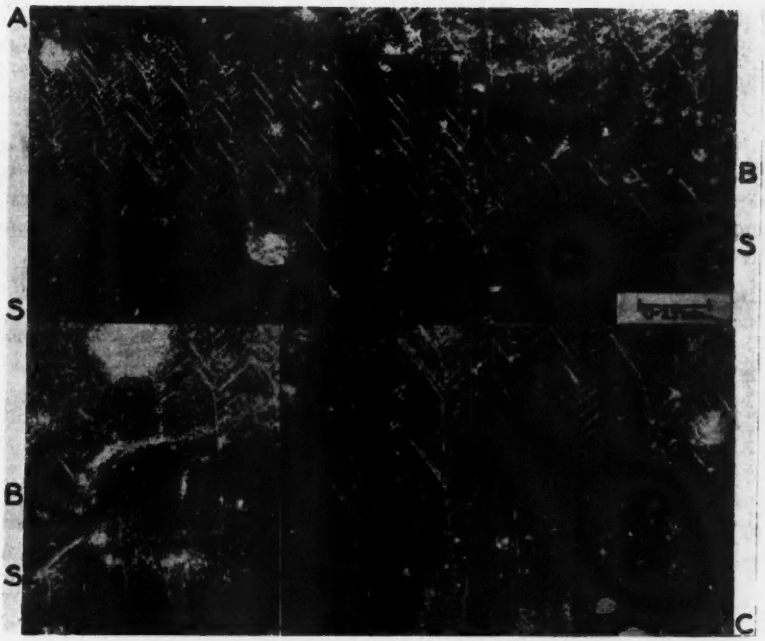


FIG. 9. Domain patterns along a grain boundary of a nickel bicrystal. Orientation similar to crystal of Fig. 2.

mined carefully by taking Laue back-reflection pictures across the whole width of the crystal. No other changes in orientation were detected on this bicrystal.

Although the domain structure is continuous across the grain boundary, the domain picture along *ABC* (or *SSS*) shows a marked change in domain spacing. In spite of the fact that there is only a small difference in orientation between crystal *A* and the stray crystal, the domain spacing varies by more than a factor of three between a point at the bicrystal boundary beyond the stray and a point on the well-developed stray. Further along into both these regions the domain width remains practically constant.

The following explanation for this change is offered. For any given crystal the observed domain width will be the resultant of the energy gained by reducing the magnetostatic energy of the configuration through the formation of domains and of the energy expended as domain wall energy. The observed decrease in domain spacing must mean that on the interfaces between the stray and the bicrystal additional "free magnetic charges" occur, which are reduced by closer spacing of the domains. Unfortunately, we know nothing about the area and crystallographic direction of these interfaces, although one can estimate the "charges" producing this change in spacing.

These two examples, chosen from a large number of similar observations, will serve to illustrate the influence of internal surfaces on the domain structure of nickel.

ACKNOWLEDGMENTS

The experimental work reported here was carried out at the Department of Metallurgical Engineering, University of Toronto. The authors would like to thank Professor Bruce Chalmers and Professor L. M. Pidgeon for their interest, and the Defence Research Board of Canada and the National Research Council of Canada for financial assistance.

REFERENCES

1. BITTER, F. Phys. Rev. 38: 1903. 1931; 41: 507. 1932.
2. DIJKSTRA, L. J. Relation of magnetic properties to microstructure. *In* ASTM Seminar on Relation of Properties to Microstructure. 1954. p. 209.
3. DIJKSTRA, L. J. and MARTIUS, U. M. Revs. Mod. Phys. 25: 146. 1953.
4. GOW, K. V. and CHALMERS, B. Brit. J. Appl. Phys. 2: 300. 1951.
5. KAYA, S. and SEKIYA, I. Z. Physik, 96: 53. 1935.
6. LILLEY, B. A. Phil. Mag. 41: 792. 1950.
7. MCKEEHAN, L. W. and ELMORE, W. C. Phys. Rev. 46: 529. 1934.
8. MARTIUS, U. M., GOW, K. V., and CHALMERS, B. Phys. Rev. 82: 106. 1951.
9. NÉEL, L. Cahiers phys. 25: 1. 1944.
10. SHOCKLEY, W. J. phys. radium, 12: 321. 1951.
11. WILLIAMS, H. J., BOZORTH, R. M. and SHOCKLEY, W. Phys. Rev. 75: 155. 1949.
12. YAMAMOTO, M. and IWATA, T. Phys. Rev. 81: 887. 1951.
13. YAMAMOTO, M. and IWATA, T. Science Repts. Research Insts. Tôhoku Univ. Ser. A, 5: 432. 1953.

THE RESOLUTION OF FOUR-DIMENSIONAL VECTOR FIELDS AND TENSOR FIELDS, AND ITS APPLICATION TO ELECTRODYNAMICS[1]

By N. L. Balazs

ABSTRACT

We generalize Helmholtz's theorem and apply it to four-dimensional vector fields and tensor fields. For vector fields the generalization is straightforward. Antisymmetric tensor fields of rank two exhibit a beautiful symmetry between the irrotational part of the tensor and the dual of the solenoidal component. The physical applications show that in Maxwell's theory the irrotational part of the four-potential field has no physical meaning and the Lorentz condition makes it identically zero. In Dirac's new electrodynamics an algebraic condition is imposed on the four-potential. Hence in this theory the irrotational part is not zero, and the algebraic condition establishes a relation between the sources and vortices of the four-potential field. If we apply the resolution to the electromagnetic field tensor we can see that the free charges are responsible for the sources, and the magnetic poles, if they exist, for the vortices, provided we use the customary association between the components of the electromagnetic field tensor and the components of the electric and magnetic fields.

I. INTRODUCTION

It is well known that a three-dimensional vector field (subject to certain analytical conditions) can be represented uniquely and completely as the sum of an irrotational and a solenoidal field.

In this note we generalize this theorem and apply it to vector fields and *tensor fields* defined in four-dimensional Euclidean and Minkowski spaces. Most of the results could immediately be extended to n-dimensional spaces. However, from a physical viewpoint this is of slight importance.

First we discuss the Euclidean case. Then we pass to Minkowski spaces. This is achieved by taking a complex unit vector in the four-dimensional space.

We will apply the results so obtained to the four-potential field and to the electromagnetic field tensor satisfying Maxwell's equations. Finally we show that in Dirac's new electrodynamics the condition imposed on the four-potential field can be interpreted as a relation between the sources and vortices of the field.

II. MATHEMATICAL DEVELOPMENT

1. *Euclidean Space*

1.1. *Vector Fields*

Our object of interest is a four-dimensional Euclidean space and a vector field V_i in it ($i = 1, 2, 3, 4$). V_i is defined everywhere. At infinity V_i and its first derivatives vanish sufficiently fast so that their integrals over infinitely distant hypersurfaces should vanish.

Our aim is to resolve V_i into two parts, $V_i = V_i^1 + V_i^2$. Here V_i is irrotational, $V_{i,k}^1 - V_{k,i}^1 = 0$, (no vortices only sources and sinks); V_i^2 is solenoidal,

[1]*Manuscript received November 22, 1954.*
Contribution from the Department of Physics, University of Alabama, University, Alabama.

$V^2_{i,i} = 0$, (no sources and sinks only vortices); the comma denotes partial derivatives; summation is implied on repeated indices.

To accomplish this we have to answer three questions:

(1) How can we find V^1_i, V^2_i, knowing V_i?

(2) Is the decomposition really complete? (This means that V_i *is* actually and only the sum of V^1_i, V^2_i now found; hence it does not contain parts which are not described either by V^1_i or V^2_i.)

(3) Is the decomposition unique?

Our plan will be as follows:

First we construct V^1_i. Then we find $V_i - V^1_i$ in terms of V_i and its derivatives, and show that this vector is solenoidal. Hence it can be identified with V^2_i. This way we have not only constructed V^2_i, but have also demonstrated that V_i *is* the sum of V^1_i and V^2_i. This answers questions (1) and (2). Finally we show that the decomposition is unique up to a vectorial constant.

Construction of V^1_i

Put

$$V^1_i = -\Phi_{,i} + \text{constant}. \tag{1}$$

Then

$$V^1_{i,k} - V^1_{k,i} = 0, \text{ and } V_{i,i} = -\Phi_{,ii}. \tag{2}$$

This equation can be solved immediately for Φ, if V_i is given, using the four-dimensional form of Green's theorem. The solution is:

$$\Phi = \frac{1}{(2\pi)^2}\int \frac{V_{i,i}}{R^2}\, d^4\xi, \tag{3}$$

$$R^2 = (x_k - \xi_k)(x_k - \xi_k), \qquad d^4\xi = d\xi_1 d\xi_2 d\xi_3 d\xi_4,$$

provided V_i satisfies the conditions mentioned above. The integration extends over the whole four-space.

Construction of V^2_i, *and demonstration of completeness*

Put $v_k = V_k - V^1_k = V_k + \Phi_{,k}$. Φ is the solution of $V_{k,k} = -\Phi_{,kk}$. Then V_i satisfies the differential equation:

$$v_{k,ss} = V_{k,ss} + \Phi_{,ssk} = V_{k,ss} - V_{s,sk} = -(V_{s,k} - V_{k,s})_{,s}. \tag{4}$$

The solution is given by

$$v_k = \frac{1}{(2\pi)^2}\int \frac{(V_{s,k} - V_{k,s})_{,s}}{R^2}\, d^4\xi. \tag{5}$$

This can also be written as $v_k = t_{ks,s}$ where

$$t_{ks} = \frac{1}{(2\pi)^2}\int \frac{V_{s,k} - V_{k,s}}{R^2}\, d^4\xi = -t_{sk}.$$

For

$$t_{k,ss} = \frac{1}{(2\pi)^2}\int (V_{s,k} - V_{k,s})\frac{\partial}{\partial x_s}\left(\frac{1}{R^2}\right) d^4\xi = -\frac{1}{(2\pi)^2}\int (V_{s,k} - V_{k,s})\frac{\partial}{\partial \xi_s}\left(\frac{1}{R^2}\right) d^4\xi$$

$$= \frac{1}{(2\pi)^2}\int \frac{(V_{s,k} - V_{k,s})_{,s}}{R^2}\, d^4\xi.$$

It is evident that $v_{k,k} = 0$; hence it is a solenoidal vector. So, if we identify it with V_i^2, we have decomposed V_i completely into an irrotational part V_i^1, and a solenoidal part V_i^2. V_i^1 is the gradient of the scalar Φ; V_i^2 is the tensor divergence of the antisymmetric tensor t_{ik}.

Proof of uniqueness.—A moment's contemplation shows that the decomposition is unique, up to a vectorial constant. For, suppose there is another resolution $\bar{V}_i^1$, $\bar{V}_i^2$. The vector $Z_i = \bar{V}_i^1 - V_i^1$, being the difference of two irrotational vectors, is irrotational. It is, however, solenoidal as well. For, $Z_{i,i} = \bar{V}_{i,i}^1 - V_{i,i}^1 = V_{i,i} - V_{i,i} = 0$. Similarly $\bar{V}_i^2 - V_i^2$ is irrotational and solenoidal. Hence, both must be constant vectors.

1.2 *Tensor Fields*

Every tensor can be split into a symmetric and antisymmetric part, and their properties can be discussed separately. We will see later that the symmetric tensors do not lend themselves to a resolution, primarily because no useful definition can be given for the operation curl as applied to them. For this reason, we confine our interest to antisymmetric tensors. Then, in four dimensions the following possibilities arise:

A totally antisymmetric tensor of rank four; this has only one independent component, so we are not interested in it. A totally antisymmetric tensor of rank three t_{ikl}; its dual $(e_{iklm}t_{klm})/3!$ is a vector, consequently everything we have said applies to it immediately (e_{iklm} is the four-dimensional permutation symbol). An antisymmetric tensor of rank two, h_{ik}. We will be concerned with the latter.

It is not immediately evident how we should define an irrotational tensor field. However, we may observe that if Stokes' theorem in four dimensions is applied to an antisymmetric tensor of rank two the cyclic divergence is the operation corresponding to the operation curl in Stokes' theorem if the latter is applied to three-dimensional vector fields. In three dimensions Stokes' theorem can be and is used to define the vortex vector and the operation curl. We do the same here too, and *define* an irrotational antisymmetric tensor field h_{ik}^1 by the condition $e_{iklm}h_{lm,k}^1 = 0$. By introducing the tensor $\hat{h}_{ik}^1 = \frac{1}{2}e_{iklm}h_{lm}^1$, the dual of h_{lm}^1, we can write this condition in the elegant form $\hat{h}_{ik,k}^1 = 0$. (This shows why we cannot discuss symmetric tensors. In Stokes' theorem the integrand, if it is a tensor, is always antisymmetric, since the volume and surface elements are antisymmetric tensors and upon contraction the symmetric part of the integrand would vanish.)

The solenoidal part $h_{ik,k}^2$ is subjected to the condition $h_{ik,k}^2 = 0$.

Now we proceed in exactly the same manner as in 1.1. h_{ik} satisfies the same analytical conditions as V_i did.

Construction of h_{ik}^1

Put $h_{ik}^1 = a_{k,i} - a_{i,k}$.

Then $\hat{h}_{ik,k}^1 = 0$, and $h_{ik,k} = h_{ik,k}^1 = a_{k,ki} - a_{i,kk}$.

Put $a_{k,k} = 0$.

Then $a_{i,kk} = -h_{ik,k}$.

The solution is:

$$a_i = \frac{1}{(2\pi)^2}\int \frac{h_{ik,k}}{R^2}\, d^4\xi.$$

(It is easy to verify that $a_{i,i}$ *is* actually zero.)

Construction of h^2_{ik} *and demonstration of completeness*

Put $\eta_{ik} = h_{ik} - h^1_{ik}$, where $h^1_{ik} = a_{k,i} - a_{i,k}$, and $h_{ik,k} = -a_{i,kk}$. Then η_{ik} satisfies the differential equation:

$$\eta_{ip,ss} = h_{ik,ss} - a_{k,ssi} + a_{i,ssk} = h_{ik,ss} + h_{ks,si} - h_{is,sk} = (h_{ik,s} + h_{ks,i} + h_{si,k})_{,s}.$$

The solution is

$$\eta_{ik} = -\frac{1}{(2\pi)^2}\int \frac{(h_{ik,s} + h_{ks,i} + h_{si,k})_{,s}}{R^2}\, d^4\xi.$$

It is easily seen that $\eta_{ik,k} = 0$; hence the tensor defined by it is solenoidal. Consequently if we identify it with h^2_{ik} we have decomposed h_{ik} completely into an irrotational part h^1_{ik}, and a solenoidal part h^2_{ik}.

For future application in physics, and for reasons of symmetry, we mention that h^2_{ik} can be put in the form $\hat{h}^2_{ik} = b_{k,i} - b_{i,k}$, where

$$b_k = \frac{1}{(2\pi)^2}\int \frac{\hat{h}_{ks,s}}{R^2}\, d^4\xi; \qquad b_{k,k} = 0.$$

This result can easily be verified using well-known properties of the contracted products of permutation symbols.

Hence we have the symmetrical scheme:

$$h_{ik} = h^1_{ik} + h^2_{ik}$$

$h^1_{ik} = a_{k,i} - a_{i,k}$	$\hat{h}^2_{ik} = b_{k,i} - b_{i,k}$
$a_{k,k} = 0$	$b_{k,k} = 0$
$a_k = \frac{1}{(2\pi)^2}\int \frac{h_{ks,s}}{R^2}\, d^4\xi$	$b_k = \frac{1}{(2\pi)^2}\int \frac{\hat{h}_{k,ss}}{R^2}\, d^4\xi$

Proof of uniqueness.—It runs exactly the same way as for vector fields, and demonstrates the uniqueness up to a tensorial constant.

2. *Minkowski Space*

For physical purposes the generalization embracing Minkowski spaces is of great importance since this corresponds to the space–time continuum of the special theory of relativity.

After Herglotz (2) and Sommerfeld (3) we do this in the following manner. If one of the coordinates is allowed to take complex values the above analysis will not change. (If the signature is $(+, +, +, -)$ this coordinate will of course be x_4.) If this complex variable is *real*, our space is Euclidean and the differential equations [2] and [4] are elliptic. If, on the other hand, we take it as purely imaginary, the space is Minkowskian and the differential equations are of the hyperbolic type. Notwithstanding—and this is the brilliant idea of Herglotz and Sommerfeld—the solutions given embrace both type of solutions, provided we introduce a complex ξ_4 plane to perform the integration with

respect to ξ_4 taking proper care of the singularities of the integrand in this complex ξ_4 plane. (Of course afterwards we have to verify that the solution so obtained is an analytic function of the complex x_4 variable.)

Take as the vector field V_i the four-potential field A_i which satisfies Maxwell's equations.

The irrotational part is given by

$$A_i^1 = \frac{1}{(2\pi)^2} \int \frac{A_{j,j}}{R^2} d^4\xi,$$

while the solenoidal part is

$$A_i^2 = \frac{1}{(2\pi)^2} \int \frac{j_i}{R^2} d^4\xi,$$

on account of Maxwell's equations

$$F_{ik,k} = (A_{k,i} - A_{i,k})_{,k} = j_i$$

is the four current density. The implications will be discussed shortly.

Let us turn now to the tensor field h_{ik}.

Take $h_{ik} = F_{ik}$, where F_{ik} is the electromagnetic field tensor satisfying Maxwell's equations.

The *irrotational part and only* this part is given by the conventional four-potential, since F_{ik}^1 can be derived from

$$F_{ik}^1 = A_{k,i} - A_{i,k}, \qquad A_i = \frac{1}{(2\pi)^2} \int \frac{j_i}{R^2} d^4\xi,$$

($j_i = F_{ik,k}$ on account of Maxwell's equations).

What about the solenoidal part F_{ik}^2? Since we know that the four-potential characterizes the electromagnetic field completely (if the latter satisfies Maxwell's equations), the solenoidal part of F_{ik} must be zero. Indeed

$$\hat{F}_{ik}^2 = B_{k,i} - B_{i,k}, \qquad B_i = \frac{1}{(2\pi)^2} \int \frac{\hat{F}_{ik,k}}{R^2} d^4\xi.$$

But $\hat{F}_{ik,k} = 0$ according to Maxwell's equations.

If on the other hand we would suppose the existence of free magnetic poles (thus $\hat{F}_{ik,k} = p_i$ where p_i is the pole current density) B_i would correspond to a magnetic four-potential or anti-four-potential using a word coined once by Professor M. Born. It is worth while to mention that it is the *dual* of F_{ik} which is the curl of the anti-four-potential B_i.

Consequently we can draw this conclusion: the free charges are responsible for the sources (and sinks) of the electromagnetic field, while the (missing) magnetic poles would create its vortices: (by renaming the components of the field tensor this conclusion could be reversed saying thus: charges are responsible for the vortices, poles for sources).

It is remarkable that the electromagnetic field created by the charges is completely separated from the field produced by the poles.

The fact that this separation is Lorentz invariant is not surprising (though worth pointing out). Would it not be so, some observers would believe a field was created by a charge, while others would think it is due to a pole. This

would have grave consequences as regards the permanence of charges and poles.

What is surprising is the conclusion that the two fields correspond to the irrotational and solenoidal parts respectively. Even this is, however, understandable. Above, we have mentioned the reasons why the splitting of the electromagnetic field into parts due to poles and charges should be Lorentz invariant. Now, if we were able to prove that the resolution of the same field into irrotational and solenoidal parts is the *only* Lorentz invariant resolution relating to the derivatives of the field (a rather plausible conjecture), we would show why the two fields of different physical origins are bound to correspond to the irrotational and solenoidal parts.

Let us return now to the four-potential field and investigate briefly the relation between the four-potential field and the electromagnetic field.

We observe first that the *solenoidal* part of the A_i field is responsible for the irrotational part of the electromagnetic field F_{ik} (on account of the fact that the electromagnetic field tensor is the *curl* of the four-potential). We might say that one field's vortex is another field's source.

It is common knowledge that this relation between F_{ik} and A_i is such that an infinite number of A_i fields correspond to the same F_{ik}. These A_i fields are connected with each other by gauge transformations. Since the difference of any two such A_i fields is the gradient of a scalar, we see that the gauge transformations change the irrotational part of the A_i field; it sinks and sources. If, then, the sources and sinks in the A_i field have no effect on the F_{ik} field, why not eliminate them? Indeed this is done, and the Lorentz condition usually imposed on the A_i field, $A_{i,i} = 0$, does nothing else but put the irrotational part of A_i equal to zero. Then the vector field will be purely solenoidal, and actually the expression for the solenoidal part gives nothing else but the advanced and retarded potentials (3).

On the other hand in Dirac's new electrodynamics (1) the seemingly simpler algebraic condition $A_iA_i = \text{const.}$ takes the place of the Lorentz condition. In this theory then, the A_i field will *not* be entirely solenoidal, and so it will *not* be given completely by the advanced and retarded potentials. Moreover, the above condition can be looked upon as a relation between A_i^1 and A_i^2 which establishes a relation between the sources (and sinks) and vortices of this field. The deeper meaning of this relationship will require further investigation.

ACKNOWLEDGMENT

I should like to express my thanks to Professor Carl Eckart for reading the manuscript and giving valuable suggestions. My thanks are also due to the Scripps Institution of Oceanography for their hospitality and to the Research Committee of the University of Alabama for their grant to pursue this research.

REFERENCES

1. DIRAC, P. A. M. Proc. Roy. Soc. (London), A, 209: 291. 1951.
2. HERGLOTZ, G. Göttinger Nachr. Math.-naturw. Kl., 549. 1904.
3. SOMMERFELD, A. Ann. Phys. 33: 665. 1910.

LONG DISTANCE V.H.F. FIELDS

I. PARTIAL REFLECTION FROM A STANDARD ATMOSPHERE[1]

By F. H. Northover[2]

ABSTRACT

Reliable propagation of V.H.F. waves and microwaves from high power transmitters to distances of several hundred miles beyond optical range has been demonstrated by an ever increasing number of experiments during the last ten years. The fields which have been observed have consistently been many times greater than the field strengths predicted by the "effective radius" theory. The present paper will be published in two parts. In Part I the theory that the phenomenon can be explained solely in terms of "partial internal reflection" from elementary layers of a dielectric distribution where the rate of decrease of $(\mu-1)$ with height is everywhere continuous and of the same order of magnitude as in a "standard" atmosphere is carefully examined and found to be untenable. In Part II, the case where the distribution contains "sharp layers" (i.e., local regions where $(\mu-1)$ changes relatively rapidly with height) is examined and it is found that these could cause the phenomenon. However, in view of the other characteristics of the observed field, it is concluded that the effect in question is probably more usually due to scattering of the electromagnetic waves from atmospheric turbulence.

1. INTRODUCTION

Reliable propagation of V.H.F. waves and microwaves from high power transmitters to distances of several hundred miles beyond optical range has been demonstrated by an ever increasing number of experiments during the last ten years (e.g. Megaw (9), 1950). Taken collectively, these experiments demonstrate conclusively that the fields, though weak, are very much stronger than had been predicted by standard "effective radius" theory. Four explanations have been offered in recent years: the extra field may arise from

(*a*) scattering by local atmospheric inhomogeneities,

(*b*) the deviation of the earth's surface from the smooth sphere of theory,

(*c*) the effect of molecular scattering by the dielectric comprising the earth's atmosphere (this is sometimes called "partial internal reflection"),

(*d*) partial reflection from high level subsidence inversions.

The great probable importance to radio technology of these weak fields well beyond the horizon can be said to come from their omnipresence at all times and places, and in all frequency bands, for systems employing sufficiently high power and antenna gain.

We proceed to comment in detail upon these theories.

(*a*) *Scattering from Atmospheric Turbulence*

Some years ago (9), considerable effort was made in England to estimate the intensity and scale of atmospheric turbulence from observations on the twinkling of stars. More recently, however, a new device has been developed which makes it possible to investigate, with much greater precision, the

[1]*Manuscript received December 15, 1954.*

The work reported in the present paper was carried out in the laboratories of the National Research Council in consultation with N.R.C. staff during the summer months of 1954.

[2]*Department of Mathematics, Memorial University of Newfoundland, St. John's, Newfoundland.*

scale on which turbulence is present. The new instrument, which is called the "microwave refractometer", has been made airborne, and it is now possible to see, at least statistically, whether the turbulence is sufficient in intensity and scale to explain the radio observations. Measurements at lower levels ($h < 5000$ ft.) made by Crain, Deam, and Gerhardt (5, 1953) seem to show that this is the case (at any rate for the radio ranges at which turbulence below 5000 ft. is likely to be of importance). Higher up, the chief feature seems to be the almost persistent occurrence of very sharp elevated layers (Crain and Gerhardt (6); Crain (4)) which are sufficient to account for the phenomenon on meter wavelengths (Northover (10, 12)) but not on centimeter wavelengths.* However, recent observations have shown that the turbulent fluctuations occur up to heights of the order of 25,000 to 30,000 ft., although they are not, as a rule, nearly so intense there as the fluctuations encountered lower down. It was also found that frequent local maxima occur—these are, presumably, associated with the elevated layers.

It would, therefore, appear quite possible that turbulence could account for the observed long distance fields also. Unfortunately, it does not appear possible to settle this question by *direct* means owing to a certain difficulty which arises if attempts are made to apply the Booker–Gordon scattering theory in its present form to the problem of the long distance fields. This difficulty appears, to this writer, to lie in the fact that the scattered energy from a considerable part of the turbulence normally present (i.e. that in the lower levels of the troposphere) can, at long range, only reach the receiver by diffraction around the earth's curve. Allowance for this would be difficult (especially when the scattering elements were themselves in the diffraction field of the transmitter), and will not be attempted in the present paper.

(*b*) *Diffraction around Rough Edges*

This, of course, would only be applicable to experiments over rough terrain. For example, a high mountain ridge obstructing a radio path can cause *less*† loss of signal at suitable regions in its rear owing to the fact that there are four paths for diffraction around a mountain ridge obstacle when ground reflection is taken into account. This phenomenon would, however, obviously not explain the long distance fields which have been observed over sea paths.

(*c*) "*Partial Reflection*"

The most recent suggestion for the explanation of the phenomenon has resulted from various attempts to calculate more carefully the effects of the earth's tropospheric envelope itself. It is suggested that the use of a four-thirds earth radius to correct for air refraction (and thereafter forgetting about the air) by no means accurately allows for the total effect of the atmosphere in helping to guide the weak waves around the earth's curve, when the question of long distance fields is being considered. As is well known, the "effective radius" solution arises from an application of the W.K.B. type of

*See Part II of the present work.
†Less, that is, than the loss over a similar path around a smooth earth.

asymptotic approximation to the differential equation which gives the height gain function, μ (the refractive index) being supposed to be a single analytic function of the height. Attempted refinements of this solution have led to the notion that an inhomogeneous medium has built into it a reflection coefficient per unit thickness (Bremmer (2)) that operates on plane progressive* waves trying to pass through, especially at oblique incidence. It appears that the W.K.B. first approximation neglects this "reflective" effect of the inhomogeneous medium, and considers only the refractive effect of the inhomogeneity. Since the field at long distance estimated on an "effective radius" basis falls very far short of the fields which are actually observed, it has been suggested that the "partial reflection", which the first approximate form of the W.K.B. solution neglects, might perhaps be sufficient in itself to account for these long distance fields, even when the refractive index decreases steadily and smoothly with a lapse rate everywhere of the order of that in a "standard atmosphere" (Carroll (3)). This suggestion has given rise to some controversy and the aim of Part I of this paper is to settle this point.

Let δ_0 be the surface value of the dielectric constant *less* unity, and let $x = 2\pi R/\lambda$, R being the earth's radius and λ the wavelength. Then effective radius type modes† exist when $x^{2/3}\delta_0 \gg 1$ provided that the lapse rate of μ is everywhere less than $\frac{1}{R}\left(1 - \frac{1}{x^{2/3}\delta_0}\right) \backsim \frac{1}{R}$ and that the lapse rate changes only slowly with height. By obtaining perturbation formulae about the "effective radius" solution and also about the airless earth solution (the latter is given by $x^{2/3}\delta_0 \ll 1$),‡ or by obtaining the solution in terms of a height integral, it can be shown that the curvilinear attenuation of the principal wave when all modes are leaky lies always between the Watson airless earth value and the "effective radius" value. Modes of this type are, therefore, quite inadequate to explain the effect in question as they give far too small a value for the distant fields owing to the high rate at which they are attenuated as we proceed into the diffraction region.

It is therefore evident that we need to discover a solution which takes account of contributions to the received field when there are strong (but *not* discontinuous) local changes in $(\mu-1)$ and $d\mu/dh$ aloft. Quite recently, Carroll (3) has taken a step towards this ideal by his careful analysis of the "Bilinear" refractivity profile; i.e., that profile in which $(\mu-1)$ decreases linearly with height at a rate equal to the surface value of the lapse rate in the "standard" atmosphere until it reaches the value zero, thereafter remaining zero. For this model he finds that the modes which give significant contributions to the field are much more numerous than those of the "effective radius" theory. As the mode number increases, the attenuation rate passes through a minimum

*$(\mu-1)$ *is supposed to vary so slowly through the medium that the waves passing through a region whose dimensions are of the order of several wavelengths can be considered as practically plane.*

†*Modes equivalent to those appropriate to propagation around an airless earth having the "effective" radius.*

‡*Thesis, London, (11), 1952. See also present paper, §4, and Part II, Appendix 5.*

after which it again increases.* For $\delta_0 = 7.26 \times 10^{-4}$ the modes of minimum attenuation are found to have attenuation rates of 0.10 db./km. and 0.15 db./km. at 50 and 3000 Mc./sec. respectively. These rates are actually quite similar to the average attenuation rates observed to occur well beyond the horizon. It is further found that Carroll's mode sums (carried to a sufficient number) agree well with the effective radius field strength curve for distances up to about 25 miles beyond the horizon. Beyond this distance they agree quite well with the experimental values which were obtained by Megaw.

These results are very interesting but it seems (at least to this writer) that the discontinuity in $d\mu/dh$ inherent in Carroll's model renders it unrealistic, especially in view of the large height† at which this discontinuity occurs. In practice, the lapse rate of μ never becomes *actually* discontinuous although it and $(\mu-1)$ are sometimes capable of such rapid local variation that the effect of a local $d\mu/dh$ discontinuity is produced, *especially on the longer wavelengths.* This sort of phenomenon is, in practice, associated with the occurrence of thin elevated inversion layers (high level subsidence inversions). The height integral of §4, which expresses‡ the total amount of partial reflection from a μ-distribution, vanishes identically in the case of a linear model. The energy reflected in Carroll's model must, therefore, be sent back entirely at the discontinuity of $d\mu/dh$ aloft.† In practice (as shown by this height integral) partial reflection takes place at all heights, being particularly intense in those regions where $d\mu/dh$ is changing relatively rapidly. It therefore seems worth while to examine carefully the problem presented by a distribution with continuously varying lapse rate of μ:

(i) when $R(d\mu/dh)$ is everywhere small (the "standard atmosphere" type of profile),

(ii) when $R(d\mu/dh)$ and its derivative become large in narrow local height bands (elevated layers).

(*d*) *Effect of Sharp Elevated Layers* (*High Level Inversions*)

The writer has examined in detail the effect of one such layer (10) and, more recently (12), the effect when several such layers act together. On meter wavelengths they are definitely capable of producing appreciable fields at long distance, because they act effectively as dielectric $(\mu-1)$ discontinuities at such wavelengths, the full "Fresnel" reflection being produced. On centimetric waves the reflection they produce, although naturally weaker, is (as will appear in Part II) still many decibels above "effective radius" level. Even this reflection, however, sometimes proves to be insufficient to give fields ap-

*This is exactly paralleled by the behavior of the mode eigenvalues in the writer's previous paper (10) on the field under a high level subsidence inversion and seems to be a fundamental characteristic of refractivity profiles which have rapid local changes in $d\mu/dh$ aloft. Assumption that $d\mu/dh$ is (effectively) discontinuous at some level requires the application of boundary conditions at the discontinuity, the satisfaction of which is the mathematical expression of the local reflection which occurs there and (in the case of linear refractivity variation) nowhere else.

†In fact this model is essentially equivalent to a single sharp elevated layer positioned at the $d\mu/dh$ discontinuity (see Part II).

‡It is logical to give it this interpretation (although we are not concerned with ray theory in this paper) because this integral vanishes identically in the case where there cannot possibly be any "partial reflection", namely, the Watson airless earth case.

proaching the order of magnitude of those observed by Megaw in the far diffraction region. The fundamental reason for this seems to be that, even on wavelengths which are too short to enable the layer to behave like a *dielectric discontinuity* (and so produce Fresnel reflection), the wavelength may still be sufficiently long for it to behave like a $d\mu/dh$ discontinuity.

2. THE EXPRESSION FOR THE FIELD

2.1. It can be shown* from Maxwell's equations that the field excited by a horizontal electric dipole in the direction of optimum propagation† and radiating into a non-homogeneous atmosphere is given, to a high order of approximation, by vector expressions of the form

$$\mathbf{E} = -\frac{ip}{\kappa C}\operatorname{curl}\mathbf{\Lambda}, \qquad \mathbf{H} = \operatorname{curl}\left(\frac{1}{\kappa}\operatorname{curl}\mathbf{\Lambda}\right), \tag{1}$$

in which $p/2\pi$ is the frequency, κ the dielctric constant, C the velocity of light, and $\mathbf{\Lambda}$ the radial vector

$$\{r\kappa\Pi(r,\theta);\,0;\,0\}.$$

Here (r, θ) are the axially symmetric spherical polar coordinates whose center is at the earth's center and whose initial line ($\theta = 0$) is along the line joining the earth's center to the dipole position; and $\Pi(r, \theta)$ is a function which satisfies the partial differential equation

$$\frac{1}{r}\frac{\partial^2}{\partial r^2}\left(r\frac{\partial\Pi}{\partial\theta}\right)+\frac{1}{r^2}\frac{\partial}{\partial\theta}\left\{\frac{1}{\sin\theta}\frac{\partial}{\partial\theta}\left(\sin\theta\frac{\partial\Pi}{\partial\theta}\right)\right\}+\frac{\kappa p^2}{C^2}\frac{\partial\Pi}{\partial\theta}=0. \tag{2}$$

It follows from this that Π can be expanded into a series of the form

$$\sum_{(n)}\frac{\Omega_n(r)}{r}P_n(\cos\theta) \tag{3}$$

where $P_n(\cos\theta)$ is the Legendre function of order n, and $\Omega_n(r)$ satisfies the equation

$$\frac{d^2\Omega_n}{dr^2}+\left\{\frac{p^2}{C^2}\kappa-\frac{n(n+1)}{r^2}\right\}\Omega_n=0, \tag{4}$$

i.e.

$$\frac{d^2\Omega_n}{d\xi^2}+\left\{\kappa-\frac{n(n+1)}{\xi^2}\right\}\Omega_n=0, \tag{5}$$

where

$$\xi = 2\pi r/\lambda. \tag{5A}$$

Let Π_0 be the contribution of the horizontal dipole to the field function Π; then the writer has shown (11) that

*Thesis; cf. also Bremmer's book "Terrestrial Radio Waves" (1).
†I.e. in a plane through the dipole center perpendicular to its axis.

$$\Pi_0 = -\frac{i\beta}{br}\sum_0^\infty (2n+1)\, u_n(b)\, U_n(\xi)\, .\, P_n(\cos\theta) \qquad (\xi < b),$$

[6] $$= -\frac{i\beta}{br}\sum_0^\infty (2n+1)\, u_n(\xi)\, U_n(b)\, .\, P_n(\cos\theta) \qquad (\xi > b)$$

where

[6A] $$b = 2\pi(R+H)/\lambda,$$

H being the height of the dipole and R the radius of the earth. Also, $U_n(\xi)$ and $v_n(\xi)$ denote those solutions of [5] which reduce respectively to $\zeta_n(\xi)$ and* $\eta_n(\xi)$ when $\kappa(\xi)$ becomes identically equal to unity (case of airless earth). The function $U_n(\xi)$ is defined by

[7] $$2U_n(\xi) = u_n(\xi)+v_n(\xi)$$

and β is defined by†

[8] $$\beta = \frac{\lambda^2}{4\pi^2 R}\left(\frac{3\Gamma}{C\kappa_d^{3/2}}\right)^{\frac{1}{3}}$$

where Γ, the radiated power, is equal to the mean value of $(C/4\pi)\iint \mathbf{E}\wedge\mathbf{H}.d\mathbf{S}$ taken over a closed surface surrounding the dipole, κ_d being the value of κ at the dipole position.

2.2. *The Series for* Π

Let Π' represent the "disturbance" field, that is to say, the field function which has to be added to Π_0 in order to produce the actual field Π; then, by [3], we must take Π' in the form

[9] $$\Pi' = -\frac{i\beta}{br}\sum_0^\infty (2n+1)\, A_n u_n(\xi)\, .\, P_n(\cos\theta)$$

where the A's must be chosen to satisfy the surface condition. For meter wave propagation over moist land and microwave and meter wave propagation over sea, the earth's surface can be considered a good conductor.† The surface condition can in this case be shown to be (11)

[10] $$\Pi_0+\Pi' = 0.$$

Hence

[11] $$A_n = -u_n(b)\, U_n(x)/u_n(x)$$

where

[11A] $$x = 2\pi R/\lambda,$$

so that the total field function Π below the level of the dipole position is

[12] $$\Pi(\xi) = -\frac{i\beta}{br}\sum_{n=1}^\infty (2n+1)\frac{u_n(b)}{u_n(x)}\{u_n(x)v_n(\xi)-v_n(x)u_n(\xi)\}P_n(\cos\theta).$$

It can be shown (11) that this series converges like $\sum \frac{1}{\sqrt{n}}\left(\frac{\xi}{b}\right)^n$. Since, however, ξ/b is very nearly unity, this convergence is extremely slow and the first

*$\zeta_n(\xi) = (\frac{1}{2}\pi\xi)^{\frac{1}{2}}H^{(2)}_{n+\frac{1}{2}}(\xi)$; $\eta_n(\xi) = (\frac{1}{2}\pi\xi)^{\frac{1}{2}}H^{(1)}_{n+\frac{1}{2}}(\xi)$.

†*Cf. References (10) and (11).*

few terms tell us nothing about the behavior of the field function which the series represents. Following a procedure similar to that adopted by Watson (13) we can obtain a series equivalent to [12] but converging much more rapidly at sufficient distances from the transmitter, by integrating

$$sP_{s-\frac{1}{2}}(-\cos\theta)\,.\,\Pi_{s-\frac{1}{2}}(\xi)\sec s\pi,$$

in which

$$\Pi_n(\xi) = \frac{u_n(b)}{u_n(x)}\{u_n(x)v_n(\xi)-v_n(x)u_n(\xi)\},$$

with respect to s, around an infinite semicircle bounded on the left by the imaginary s-axis.

The result of this integration is zero, for the writer has shown (11) that the contribution from the imaginary axis and from the curved part of the contour both tend to zero as the radius of the semicircle tends to infinity. Hence the above series can be expressed directly as the sum of the residues which occur at the zeros $\nu_1, \nu_2, \nu_3, \ldots$ of $u_{s-\frac{1}{2}}(x)$, quâ function of s.

These zeros are supposed to be arranged in order of numerically increasing* imaginary part. The new series for the field is thus

$$\Pi(\xi) = \frac{2\pi i\beta}{br}\sum_{\nu_i}\frac{\nu u_{\nu-\frac{1}{2}}(b)}{\{\partial u_{s-\frac{1}{2}}(x)/\partial s\}_{(s=\nu)}} \times\{u_{\nu-\frac{1}{2}}(x)v_{\nu-\frac{1}{2}}(\xi)-v_{\nu-\frac{1}{2}}(x)u_{\nu-\frac{1}{2}}(\xi)\}P_{\nu-\frac{1}{2}}(-\cos\theta)\}$$

$$[13]\qquad = \frac{4\pi\beta}{br}\sum_{\nu_i}\frac{\nu P_{\nu-\frac{1}{2}}(-\cos\theta)\sec\nu\pi}{u_{\nu-\frac{1}{2}}(x)\{\partial u_{s-\frac{1}{2}}(x)/\partial s\}_{(s=\nu)}}u_{\nu-\frac{1}{2}}(b)u_{\nu-\frac{1}{2}}(\xi)$$

since

$$[14]\qquad u_{\nu-\frac{1}{2}}(x) = 0$$

and, from the identical relation

$$[15]\qquad u_{s-\frac{1}{2}}(\xi)v_{s-\frac{1}{2}}'(\xi)-u_{s-\frac{1}{2}}'(\xi)v_{s-\frac{1}{2}}(\xi) = 2i,$$

we obtain

$$[15A]\qquad v_{\nu-\frac{1}{2}}(x) = -2i/u_{\nu-\frac{1}{2}}'(x).$$

It is interesting to note that the form of this result shows that the "reciprocity theorem", valid when the atmosphere is homogeneous, holds also when the refractive index varies with height.

3. THE FUNCTION $u_{s-\frac{1}{2}}(\xi)$: SOLUTION BY VARIATION OF PARAMETERS

3.1. The equation satisfied by this function is

$$[16]\qquad \frac{d^2\Omega}{d\xi^2}+\left(\kappa-\frac{s^2-\frac{1}{4}}{\xi^2}\right)\Omega = 0.$$

In the troposphere, $\kappa\ (=\mu^2)$ is always very nearly unity ($\kappa-1 = O(10^{-4})$ or less), and $-R(d\mu/dh)$ (which we shall denote by "m") is nearly always less than unity.†

* $\mathcal{I}(\nu_k) < 0$; *see Part II, Appendix 1.*

†*The exceptions can occur within an "elevated layer" and also near the surface when a "surface duct" is present.*

It will appear subsequently that $|(\nu-x)/x|$ is small of order $x^{-2/3}$. Since we are dealing with tropospheric effects δ becomes very small compared with its surface value at heights where $(\xi-x)/x$ is still $\ll 1$, and this makes $u_{s-\frac{1}{2}}(\xi) \sim \zeta_{s-\frac{1}{2}}(\xi)$ at heights where $(\xi-x)/x$ is still $\ll 1$.

We are, therefore, only interested in this particular solution of the above equation at heights for which $(\xi-x)/x \ll 1$.

Writing, therefore,

$$\begin{aligned} \nu &= x(1+\epsilon), \\ \xi &= x(1+\rho), \\ \kappa &= 1+\delta, \end{aligned} \tag{17}$$

the equation satisfied by $u_{s-\frac{1}{2}}(\xi)$ is, effectively,

$$\phi''+x^2\{2(\rho-\epsilon)+\delta\}\phi = 0 \tag{18}$$

where the dash denotes differentiation with respect to ρ.

Form of Solution near the Surface

Near the surface, the equation [18] is (neglecting terms of order $x^{-2/3}$, which are insignificant)

$$\phi''+x^2\{2(1-m_0)\rho+\delta_0-2\epsilon\}\,\phi = 0 \tag{19}*$$

so that, near the surface, $u_{s-\frac{1}{2}}(\xi)$ approximates to a certain linear combination of the functions

$$z_0^{\frac{1}{2}}H_{\frac{1}{3}}^{(1)}(\tfrac{2}{3}\sqrt{2}.xz_0^{3/2}), \qquad z_0^{\frac{1}{2}}H_{\frac{1}{3}}^{(2)}(\tfrac{2}{3}\sqrt{2}.xz_0^{3/2}) \tag{20}$$

wherein

$$z_0 = \{(1-m_0)\rho+\tfrac{1}{2}\delta_0-\epsilon\}/(1-m_0)^{2/3}. \tag{20A}$$

Solution at Large Heights

At such heights, equation [18] approximates to

$$\phi''+x^2.2(\rho-\epsilon)\phi = 0 \tag{21}$$

and so, since it is known that

$$\begin{aligned} u_{s-\frac{1}{2}}(\xi) &\sim \zeta_{s-\frac{1}{2}}(\xi) \\ &= (\tfrac{1}{2}\pi\xi)^{\frac{1}{2}}H_s^{(2)}(\xi) \end{aligned} \tag{22}$$

at large heights, we have (10, 11) at large heights

$$u_{s-\frac{1}{2}}(\xi) \sim (\tfrac{1}{2}\pi x)^{\frac{1}{2}}e^{-i\pi/6}.z_1^{\frac{1}{2}}H_{\frac{1}{3}}^{(2)}(\tfrac{2}{3}\sqrt{2}.xz_1^{3/2}) \tag{23}$$

where

$$z_1 = \rho-\epsilon. \tag{23A}$$

The characteristic values (or "eigenvalues") over which the summation [13] runs are given by equation [14]. In order to solve the propagation problem, therefore, we need to know just what linear combination of the functions [20] will approximate to $u_{s-\frac{1}{2}}(\xi)$ near the surface, it being known that, at large heights,

$$u_{s-\frac{1}{2}}(\xi) \sim (\tfrac{1}{2}\pi x)^{\frac{1}{2}}e^{-i\pi/6}.z_1^{\frac{1}{2}}.H_{\frac{1}{3}}^{(2)}(\tfrac{2}{3}\sqrt{2}.xz_1^{3/2}).$$

**The subscript zero refers to surface values.*

Standard "effective radius" theory results from solving equation [18] approximately by means of the W.K.B. (or Jeffrey's) type of asymptotic approximation; this shows that the correct form for $u_{s-\frac{1}{2}}(\xi)$ near the surface is

[24] $$(\tfrac{1}{3}\pi x)^{\frac{1}{2}}e^{-i\pi/6}z_0^{\frac{1}{2}}H_{\frac{1}{3}}^{(2)}(\tfrac{2}{3}\sqrt{2}.xz_0^{3/2}).$$

Putting $\rho = 0$ in this, and equating the result to zero, we obtain the eigenvalues of the "*effective radius*" type of solution as roots of the resulting equation in s (it is really an equation in ϵ). It has, however, to be borne in mind that [24] is no more than a *first* approximation being (effectively) the W.K.B. solution. Since this type of solution neglects the effect of "internal partial reflection", we must try to obtain a more general type of solution which will make allowances for this. This will be the subject of the section which follows.

3.2. *Method of Variation of Parameters*

In order that this method may achieve the closest possible approximation to $u_{s-\frac{1}{2}}(\xi)$ we must choose the best possible first approximation. Jeffrey's (W.K.B.) approximation is good only for values of ρ which are not too near a zero of $2(\rho-\epsilon)+\delta$ and for which also "m" is changing only relatively slowly with height. Since, however, we wish eventually to apply our solution to cases where sharp elevated layers are present, the last requirement (and perhaps even the first) will not everywhere be satisfied. Accordingly, we need a first approximation to $u_{s-\frac{1}{2}}(\xi)$ which does not suffer from the above limitations, approximates closely to the W.K.B. solution where this type of approximation is valid, and, finally, approximates to the correct forms [20] or [23], as appropriate, both near the earth's surface and at large heights. The approximation which we need in order to begin our analysis is therefore of Langer's type (8).* Accordingly, we take for our first approximation to $u_{\nu-\frac{1}{2}}(\xi)$ the solution

$$u_{\nu-\frac{1}{2}}(\xi) \simeq \left(\frac{\pi x}{3}\right)^{\frac{1}{2}} e^{-i\pi/6}\left(\frac{3W}{2Q}\right)^{\frac{1}{2}} H_{\frac{1}{3}}^{(2)}(W),$$

i.e.

[25] $$u_{\nu-\frac{1}{2}}(\xi) \simeq \left(\frac{\pi x}{2}\right)^{\frac{1}{2}} e^{-i\pi/6}\left(\frac{W}{Q}\right)^{\frac{1}{2}} . H_{\frac{1}{3}}^{(2)}(W),$$

where

$$W = x\sqrt{2}\int_{\beta}^{\rho}(\rho_1-\epsilon+\tfrac{1}{2}\delta)^{\frac{1}{2}}d\rho_1,$$

$$Q = x\sqrt{2}(\rho-\epsilon+\tfrac{1}{2}\delta)^{\frac{1}{2}},$$

so that $Q = W'$ and the fundamental equation is written

[26] $$\Omega''+Q^2\Omega = 0,$$

i.e.

$$\Omega''+(W')^2\Omega = 0.$$

Here, β is the zero of $\rho-\epsilon+\frac{1}{2}\delta$ which has a negative imaginary part.

*See also Part II, Appendix 2.

It is easily verified that this approximation reduces to the W.K.B. approximation when $|W| \gg 1$, and approximates to the correct forms ([20] and [23], as appropriate) near the surface and at large heights. Employment of this first approximation will, as a matter of fact, lead to the "effective radius" solution.

We propose now to improve upon this solution by means of the method of variation of parameters.

Write now

$$u_{\nu-\frac{1}{2}}(\xi) = A\psi_1+B\psi_2$$

[27] $$= \psi \text{ say},$$

where A and B are functions of height and

[28] $$\psi_1 = \left(\frac{\pi x}{2}\right)^{\frac{1}{2}} e^{-i\pi/6}\left(\frac{W}{Q}\right)^{\frac{1}{2}} H_{\frac{1}{3}}^{(2)}(W),$$

$$\psi_2 = \left(\frac{\pi x}{2}\right)^{\frac{1}{2}} e^{i\pi/6}\left(\frac{W}{Q}\right)^{\frac{1}{2}} H_{\frac{1}{3}}^{(1)}(W).$$

Then we know that,* if $x^{2/3}\rho$ is made large, B becomes very small and A approaches unity.

In accordance with the principle of variation of parameters, make

[29] $$A'\psi_1+B'\psi_2 = 0.$$

Then

[30] $$\psi'' = A''\psi_1+B''\psi_2+2(A'\psi_1+B'\psi_2)+A\psi_1''+B\psi_2'',$$
$$0 = A''\psi_1+B''\psi_2+A'\psi_1'+B'\psi_2'.$$

Therefore

[31] $$A\{\psi_1''+x^2[2(\rho-\epsilon)+\delta]\psi_1\}+B\{\psi_2''+x^2[2(\rho-\epsilon)+\delta]\psi_2\}$$
$$+A'\psi_1'+B'\psi_2' = 0.$$

It is shown in Part II, Appendix 2, that the quantities

$$\psi_1''+x^2.2\{(\rho-\epsilon)+\delta\}\psi_1, \qquad \psi_2''+x^2\{2(\rho-\epsilon)+\delta\}\psi_2$$

are respectively equal to

[32] $$\left(\frac{3}{4}\frac{Q'^2}{Q^2}-\frac{5}{36}\frac{Q^2}{W^2}-\frac{1}{2}\frac{Q''}{Q}\right)\psi_1,$$
$$\left(\frac{3}{4}\frac{Q'^2}{Q^2}-\frac{5}{36}\frac{Q^2}{W^2}-\frac{1}{2}\frac{Q''}{Q}\right)\psi_2.$$

Now let

[33] $$\psi_1/\psi_2 = F,$$

Cf. [23].

then, by [29],

[34] $$A'\psi_1'+B'\psi_2' = -(B'\psi_2^2/\psi_1)\,F'.$$

Hence

[35] $$-B'\frac{\psi_2^2}{\psi_1}F'+\left(\frac{3}{4}\frac{Q'^2}{Q^2}-\frac{5}{36}\frac{Q^2}{W^2}-\frac{1}{2}\frac{Q''}{Q}\right)(A\psi_1+B\psi_2) = 0.$$

Further, let

[36] $$C = B/A$$

and

[37] $$\Omega = F+C.$$

Then

[38] $$B' = \left(\frac{3}{4}\frac{Q'^2}{Q^2}-\frac{5}{36}\frac{Q^2}{W^2}-\frac{1}{2}\frac{Q''}{Q}\right)AF\frac{\Omega}{F'}.$$

A!so

$$C' = \frac{B'}{A}-\frac{BA'}{A^2}$$

$$= \frac{B'}{A}\left(1+\frac{C}{F}\right)$$

[39] $$= \frac{B'\Omega}{AF}.$$

Therefore

[40] $$C' = \left(\frac{3}{4}\frac{Q'^2}{Q^2}-\frac{5}{36}\frac{Q^2}{W^2}-\frac{1}{2}\frac{Q''}{Q}\right)\frac{\Omega^2}{F'}.$$

Hence the equation satisfied by Ω is

[41] $$\Omega' = F'+\left(\frac{3}{4}\frac{Q'^2}{Q^2}-\frac{5}{36}\frac{Q^2}{W^2}-\frac{1}{2}\frac{Q''}{Q}\right)\frac{\Omega^2}{F'}$$

where F, Q, and W are as already defined, and the dash denotes differentiation with respect to ρ.

Since the vanishing of $u_{s-\frac{1}{2}}(\xi)$ at the earth's surface implies, and is implied by, the vanishing there of $\Omega(\rho)$, it is clear that equation [41] contains the solution of our problem; for, having regard to the requirement on $\Omega(\rho)$ that $\Omega(\rho) \sim F(\rho)$ at great heights, $\Omega(\rho)$ is determined by equation [41]. We now proceed to apply this equation to the investigation of the two kinds of refractivity profile situation described at the close of §1.

4. REFRACTIVITY PROFILE WITH $d\mu/dh$ CONTINUOUS AND CHANGING ONLY SLOWLY WITH HEIGHT AT ALL HEIGHTS

We have

$$Q = x\sqrt{2(\rho-\epsilon+\tfrac{1}{2}\delta)^{\frac{1}{2}}},$$

$$W = \frac{2}{3}\sqrt{2}\,\frac{(\rho-\epsilon+\frac{1}{2}\delta)^{3/2}}{1-m} - \frac{2}{3}\sqrt{2}.x\int_\beta^\rho \frac{m'}{(1-m)^2}(\rho-\epsilon+\tfrac{1}{2}\delta)^{3/2}d\rho$$

$$= \frac{2}{3}\sqrt{2}.x\left\{\frac{(\rho-\epsilon+\frac{1}{2}\delta)^{3/2}}{1-m} - \frac{2}{5}\frac{m'}{(1-m)^3}(\rho-\epsilon+\tfrac{1}{2}\delta)^{5/2} + \frac{2}{5}\int_\beta^\rho \frac{d}{d\rho}\left\{\frac{m'}{(1-m)^3}\right\}(\rho_1-\epsilon+\tfrac{1}{2}\delta)^{5/2}d\rho_1\right\}$$

$$= \frac{2}{3}\sqrt{2}.x\left\{\frac{(\rho-\epsilon+\frac{1}{2}\delta)^{3/2}}{1-m} - \frac{2}{5}\left[\frac{m'}{(1-m)^3}(\rho-\epsilon+\tfrac{1}{2}\delta)^{5/2} - \frac{2}{7}(\rho-\epsilon+\tfrac{1}{2}\delta)^{7/2}\left\{\frac{m''}{(1-m)^4}+\frac{3m'^2}{(1-m)^5}\right\}\right] + \frac{8}{315}\left\{\frac{m'''}{(1-m)^5}+\frac{10m'm''}{(1-m)^6}+\frac{15m'^3}{(1-m)^7}\right\}(\rho-\epsilon+\tfrac{1}{2}\delta)^{9/2}\ldots\right\}$$

$$= \frac{2}{3}\sqrt{2}.x\left\{\frac{(\rho-\epsilon+\frac{1}{2}\delta)^{3/2}}{1-m} - \frac{2}{5}\frac{m'}{(1-m)^3}(\rho-\epsilon+\tfrac{1}{2}\delta)^{5/2} + \frac{4}{35}\left[\frac{m''}{(1-m)^4}+\frac{3m'^2}{(1-m)^5}\right](\rho-\epsilon+\tfrac{1}{2}\delta)^{7/2}\right\}+\ldots$$

provided

$$\frac{8}{315}\frac{m'''}{(1-m)^5}|\rho-\epsilon+\tfrac{1}{2}\delta|^3,\quad \frac{40}{63}\frac{m'm''}{(1-m)^6}|\rho-\epsilon+\tfrac{1}{2}\delta|^3,$$

$$\frac{8}{21}\frac{m'^3}{(1-m)^7}|\rho-\epsilon+\tfrac{1}{2}\delta|^3$$

are all $\ll 1$. Then

$$\frac{3}{4}\frac{Q'^2}{Q^2}-\frac{1}{2}\frac{Q''}{Q}-\frac{5}{36}\frac{Q^2}{W^2}$$

$$\simeq \frac{3}{16}\frac{(1-m)^2}{(\rho-\epsilon+\frac{1}{2}\delta)^2}+\frac{1}{8}\frac{(1-m)^2}{(\rho-\epsilon+\frac{1}{2}\delta)^2}\left\{1+\frac{2m'}{(1-m)^2}(\rho-\epsilon+\tfrac{1}{2}\delta)\right\} - \frac{5}{16}\frac{(1-m)^2}{(\rho-\epsilon+\frac{1}{2}\delta)^2}\left\{1-\frac{2}{5}\frac{m'}{(1-m)^2}(\rho-\epsilon+\tfrac{1}{2}\delta) + \frac{4}{35}\left[\frac{m''}{(1-m)^3}+\frac{3m'^2}{(1-m)^4}\right](\rho-\epsilon+\tfrac{1}{2}\delta)^2\right\}^{-2}$$

$$\simeq \frac{1}{7}\left\{\frac{2m''}{(1-m)^3}+\frac{9m'^2}{5(1-m)^4}\right\}$$

(the first order terms—i.e., those in m'—vanish identically).

We shall now find it convenient to transfer the independent variable ρ to a "natural" one P by means of the relation

[44] $$P = x^{2/3}\rho.$$

(We call P a "natural" variable because, in terms of it, the equation [18] for $u_{s,-\frac{1}{3}}(\xi)$ becomes

$$\phi_{PP}+\{2(P-E)+Z(P)\}\,\phi = 0 \tag{45}$$

where

$$E = x^{2/3}\epsilon, \qquad Z(P) = x^{2/3}\delta, \tag{45A}$$

and a suffix P denotes differentiation with respect to P. The large "x" has now disappeared from equation [18] and $u_{s-\frac{1}{3}}(\xi)$ is now a function of the single argument P.)

The equation giving Ω now becomes

$$\Omega_P = F_P+\frac{1}{7}\left\{\frac{2m_{PP}}{(1-m)^3}+\frac{9m_P{}^2}{5(1-m)^4}\right\}\frac{\Omega^2}{F_P}$$

$$= F_P\left\{1+\frac{1}{7}\left(\frac{2m_{PP}}{(1-m)^3}+\frac{9m_P{}^2}{5(1-m)^4}\right)\frac{\Omega^2}{F_P{}^2}\right\}. \tag{46}$$

Now (see Appendix 3, Part II)

$$F_P = -2ix^{1/3}/\psi_2{}^2, \tag{47}$$

$$\Omega_P = F_P\left\{1-\frac{1}{28x^{2/3}}\left(\frac{2m_{PP}}{(1-m)^3}+\frac{9m_P{}^2}{5(1-m)^4}\right)\Omega^2\psi_2{}^4\right\}. \tag{48}$$

Let the profile law be $\chi(z)$, where

$$\chi(0) = 1, \qquad \chi'(0) = -1,^* \tag{49}$$

and χ, χ' steadily decrease to zero as $z \to \infty$. Then

$$\delta = \delta_0\chi(2m_0\rho/\delta_0), \tag{50}$$

$$m = -\tfrac{1}{2}d\delta/d\rho$$

$$= -m_0\chi'(2m_0P/Z_0), \tag{51}$$

where

$$Z_0 = x^{2/3}\delta_0. \tag{51A}$$

Now, by [29] and [38],

$$A' = -\left(\frac{3}{4}\frac{Q'^2}{Q^2}-\frac{5}{36}\frac{Q^2}{W^2}-\frac{1}{2}\frac{Q''}{Q}\right)\frac{A\Omega}{F'}; \tag{52}$$

therefore

$$A_P \simeq -\frac{1}{7}\left(\frac{2m_{PP}}{(1-m)^3}+\frac{9m_P{}^2}{5(1-m)^4}\right)\frac{A\Omega}{F_P}$$

$$= \frac{1}{14ix^{\frac{1}{3}}}\left(\frac{2m_{PP}}{(1-m)^3}+\frac{9m_P{}^2}{5(1-m)^4}\right)\psi\psi_2. \tag{53}$$

The function on the right is a continuous function having no singularities for any positive value of P. This we are able to assert because, by [28], ψ_2 is non-singular for all positive values of P. Also, ψ is continuous and non-singular for all positive values of P because the differential equation which it satisfies is a non-singular equation for all positive values of P.

When P is large and positive

$$\psi \sim \psi_1$$

*The dash now denotes d/dz.

so that then

$$\psi\psi_2 \sim \psi_1\psi_2$$

[54] $$\sim x^{1/3}/(2P)^{\frac{1}{4}}$$

by [28]. Hence

[55] $$A_P = \frac{m_0^3}{iZ_0^2} h\left(\frac{m_0 P}{Z_0}\right) g(P)$$

where $h(z)$ is a positive continuous function which tends to zero as $z \to +\infty$, and $g(z)$ is a complex continuous function of z which $\sim z^{-\frac{1}{4}}$ when z is large and positive.

Integrating [55], we get

[56] $$A = 1 - \frac{m_0^3}{iZ_0^2} \int_P^\infty h\left(\frac{m_0 P_1}{Z_0}\right) g(P_1) \, . \, dP_1$$

since $A \sim 1$ as $P \to +\infty$; provided the integral converges. This is certainly the case for the exponential profile as $h(m_0P_1/Z_0)$ then contains a factor $\exp(-m_0P_1/Z_0)$. We shall restrict the present discussion to profiles which make the integral in [56] converge.

Since m_0/Z_0 is always exceedingly small compared with unity in the cases that arise in this paper, it is possible for P_1 to be large enough to make $g(P_1) \sim P_1^{-\frac{1}{4}}$ with m_0P_1/Z_0 still $\ll 1$.

Hence the integral is of order

$$\left(\frac{Z_0}{m_0}\right)^{\frac{1}{4}} \int_{m_0P/Z_0}^\infty h(\zeta) \, . \, \zeta^{-\frac{1}{4}} \, . \, d\zeta,$$

i.e. is at most of order

$$\left(\frac{Z_0}{m_0}\right)^{\frac{1}{4}}.$$

Hence $A - 1$ is at most of order $m_0^{5/2}/Z_0^{3/2}$.

Now we have, by [46],

[57] $$\Omega_P = F_P - \frac{1}{14ix^{1/3}} \left(\frac{2m_{PP}}{(1-m)^3} + \frac{9m_P^2}{5(1-m)^4}\right)\left(\frac{\psi}{A}\right)^2$$

and so, since A is so close to unity,

[58] $$\Omega = F + \frac{m_0^3}{ix^{1/3}Z_0^2} \int_P^\infty h\left(\frac{m_0 P_1}{Z_0}\right) \{\psi(P_1)\}^2 \, . \, dP_1.$$

As before, to estimate the order of magnitude of this integral, we can take P of order unity but large enough to make

$$\{\psi(P)\}^2 \sim \{\psi_1(P_1)\}^2,$$

i.e., by [42],

$$\sim \frac{xi}{Q} e^{-2iW}$$

$$\sim \frac{ix^{\frac{1}{2}}}{\{2(P-E)+Z\}^{\frac{1}{4}}} \exp[-\tfrac{4}{3}\sqrt{2}.i(P-E+\tfrac{1}{2}Z)^{3/2}/(1-m)]$$

[59] $$\sim \frac{ix^{\frac{1}{2}}}{(2P)^{\frac{1}{4}}} \exp(-\tfrac{4}{3}\sqrt{2}.iP^{3/2})$$

when $P \to +\infty$.

The curve C on which $(P-E+\frac{1}{2}Z)^{3/2}$ is real and positive when $\mathscr{R}(P) \to +\infty$ is evidently asymptotic to the line $\mathscr{I}(P) = \mathscr{I}(E)$. On deforming all the contour of integration for P_1 in [58] into the contour defined by $\mathscr{R}(P_1) = P, 0 < |\mathscr{I}(P_1)| < |X|$, where $P+iX$ is on C, and C itself; then $|\psi(P_1)|$ becomes equal to $x^{1/6}/|2(P-E)+Z|^{1/4}$ on C, and

[60] $$\left| \int_{P+iX}^{\infty(C)} h\left(\frac{m_0 P_1}{Z_0}\right) \{\psi(P_1)\}^2 . dP_1 \right| < x^{\frac{1}{2}} \int_0^{\infty} h\left(\frac{m_0 P_1}{Z_0}\right) |2(P_1-E)+Z|^{-1/4} ds$$

where s is the arc length along C from $P+iX$ to the point P_1. Let $\phi = \arg(dP_1)$ at P_1; then $ds = e^{-i\phi} . dP_1$ and ϕ is small since $\mathscr{R}(P_1) \geqslant \mathscr{R}(P) > 1$. By the requirements on h the integral on the right of [60] converges (e.g. for an exponential profile h has the factor $\exp(-2m_0 P_1/Z_0)$); hence (writing $P_1 = Z_0\zeta/m_0$) it is at most of order Z_0/m_0, i.e., there exists a number k, independent of Z_0/m_0, such that the integral in question is less than $k\, Z_0/m_0$. Hence

[61] $$\Omega(P) - F(P) = O(m_0^2/Z_0)$$

at most, and this gives

$$F(0) = O(m^2/Z_0)$$
$$\ll 1.$$

Since

[62] $$F(0) = e^{-\frac{1}{2}ix} \frac{H_{\frac{1}{3}}^{(2)}\{\frac{2}{3}\sqrt{2}.x(-\epsilon+\frac{1}{2}\delta_0)^{3/2}/(1-m_0)\}}{H_{\frac{1}{3}}^{(1)}\{\frac{2}{3}\sqrt{2}.x(-\epsilon+\frac{1}{2}\delta_0)^{3/2}/(1-m_0)\}}$$

it follows* that, if the profile is of the type considered and $m_0^2/Z_0 \ll 1$, the eigenvalues always approximate closely to the "effective radius" values.

It is interesting to note that this result applies to a quite general class of profiles of the type described by the section heading, of which the exponential profile is a special case.

REFERENCES

1. BREMMER, H. Terrestrial radio waves. Elsevier Publishing Co., Inc., New York. 1949.
2. BREMMER, H. Symposium on the theory of electromagnetic waves, June 6–8, 1950. Interscience Publishers, Inc., New York. 1950. p. 169.
3. CARROLL, T. J. Proc. Conf. Radio Meteorol., Univ. of Texas, Nov. 9–12, 1953, paper I–6. Mass. Inst. Technol. Tech. Rept. No. 38. Feb. 12, 1954.

**Appendix 4, Part II.*

4. CRAIN, C. M. Refractometer measured tropospheric index of refraction profiles. Vol. 1, Rept. 6–02; Vol. II, Rept. 6–03, Elec. Eng. Research Lab., Univ. of Texas. 1953.
5. CRAIN, C. M., DEAM, A. P., and GERHARDT, J. R. Proc. Inst. Radio Engrs. 41 (No. 2): 284. 1953.
6. CRAIN, C. M., GERHARDT, J. R., and WILLIAMS, C. E. Trans. Inst. Radio Engrs. Professional Group on Antennas and Propagation. 1953.
7. GORDON, W. E. Proc. Conf. Radio Meteorol., Univ. of Texas, Nov. 9–12, 1953, paper IV–1.
8. LANGER, R. E. Phys. Rev. 51: 669. 1937.
9. MEGAW, E. C. S. Nature, 166: 1100. 1950. Proc. Inst. Elec. Engrs. (London), Pt. III, 100: 1. 1953.
10. NORTHOVER, F. H. J. Atm. and Terrest. Phys. 2 (No. 2): 106. 1952.
11. NORTHOVER, F. H. Thesis, London University., 1952. (It is hoped eventually to publish some of this.)
12. NORTHOVER, F. H. Proc. Conf. Radio Meteorol., Univ. of Texas, Nov. 9–12, 1953, paper II–2.
13. WATSON, G. N. Proc. Roy. Soc. (London), A, 95: 83, 546. 1919.

NOTES

A NOTE ON BLACK BODY RADIATION

By A. M. Crooker and W. L. Ross*

The black body radiation formula of Planck has been discussed (1) and tabulated (3) by many authors. This note draws attention to a pertinent paper by Czerny (2) and shows how one of his suggestions can be applied and extended.

The Planck law is $J_\lambda = c_1 \lambda^{-5} [\exp(c_2/\lambda T) - 1]^{-1}$, where J_λ is the rate of emission of radiant energy into a hemisphere, say in ergs/cm.^{3} sec., and $c_1 = 2\pi hc^2 = 3.7413 \times 10^{-5}$ ergs cm.^{2}/sec. and $c_2 = hc/k = 1.43884$ cm. °K.

To obtain the radiant power $J_\lambda \, . \, d\lambda$ in the spectral region $d\lambda$, one multiplies this by $d\lambda$ and, if the unpolarized radiant flux into unit solid angle perpendicular to the surface is required, this product is divided by π. Czerny has emphasized two remarks concerning Planck's law. Firstly, if $d\lambda$ depends on λ, as in practice it may do, then, exclusive of the bracket, $J_\lambda \, . \, d\lambda$ is not proportional to λ^{-5} but to λ^{-4} if $d\lambda$ is proportional to λ, and to λ^{-3} if $d\lambda$ is proportional to λ^2, etc. The first assumes constant resolving power, $\lambda/d\lambda$, while the second assumes a constant wave number band pass,† $|d\nu| = d\lambda/\lambda^2$. For this reason, Czerny studies the general radiation function $F(\lambda, T) = \lambda^{-m} [\exp(c_2/\lambda T) - 1]^{-1}$, where m may be 2, 3, 4, 5, etc. Of course, if one works with a quantum detector rather than a "heat" detector, then m is reduced by 1 owing to the fact that each quantum carries energy $E = hc/\lambda$.

Secondly, Czerny draws attention to the fact that the form of J_λ depends strongly on T as well as on λ. He asserts that if log F is plotted against log λ, then the form of the curve does not change, that is the curve at higher temperature can be obtained by a rigid displacement of the lower temperature curve. Czerny calls this fact the generalized "Wien Displacement Law".

We include a short demonstration of this fact.

If we write

$$[1a] \qquad F(\lambda, T) = \lambda^{-m} [\exp(c_2/\lambda T) - 1]^{-1},$$

then

$$\ln F = -m \ln \lambda - \ln[\exp(c_2/\lambda T) - 1]$$

$$[1] \quad \text{or} \qquad y = -mx - \ln[\exp(c_2/Te^x) - 1]$$

where we have written

$$y = \ln F; \qquad x = \ln \lambda \quad \text{so } \lambda = e^x.$$

If we change T by dT, let y change by dy and x by dx,

*Holder of a National Research Council Fellowship, National Research Council of Canada.

†Strong (J. Opt. Soc. Amer. 39: 320, 1949) has emphasized that for "constant wave number resolving power", $d\nu$ = const., the power transmitted by a spectrometer can be written as independent of λ in the Rayleigh–Jeans region. If one agrees to say that the Rayleigh–Jeans law holds when it predicts a radiant power less than x% greater than actual, then this occurs when $\lambda T \geqslant 1.438$ cm.°K./0.02x (for $x < 10$%).

[2] then $$y+dy = -m(x+dx)-\ln[\exp\{c_2/(T+dT)e^{x+dx}\}-1].$$

Now [1] and [2] are identical if

[3a] $$dy = -mdx$$

and
$$\begin{aligned} e^xT &= e^{x+dx}(T+dT) \\ &= e^x(T+dT)\,.\,(1+dx) \\ &= e^x(T+Tdx+dT), \end{aligned}$$

[3b] i.e., $$dx = -dT/T.$$

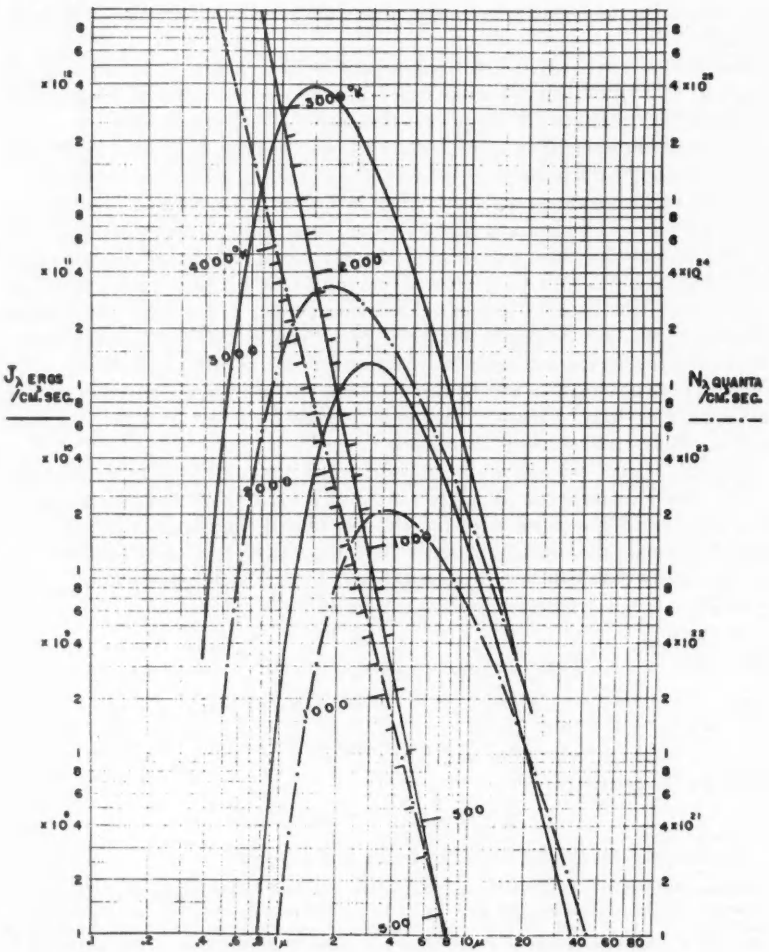


FIG. 1. Hemispherical radiation rates.

Thus if

[3] $$dy/m = -dx = dT/T$$

then [1] and [2] are identical. The first equation in [3] means that the form of the relation between log F and log λ is independent of T. Thus, if one plots log F against log λ at any temperature, one can obtain log F as a function of log λ at another temperature by displacing this curve along the line of slope $-m$ in accordance with equations [3], namely

$$-\Delta x = -(x_2 - x_1) = \ln(T_2/T_1).$$

We have found it convenient to draw a graph of [1] on log–log paper. In Fig. 1 this is done for the values $m = 5$, with full line, and $m = 4$, with broken line, for two temperatures $T = 1000°$ and 2000°K. The curves at $T = 1000°$K. were carefully drawn from the values given in the W.P.A. tables (3), corrected for changes in the radiation constants c_1 and c_2. Appropriate temperature axes, with slopes -5 and -4, were drawn through points 10 db. directly below the maxima. The actual position of these temperature axes is arbitrary, since the slope is defined in [3]. Our choice of drawing these through the point 10 db. down from the maximum permits the radiation rates to be read off for arbitrary values of the emissivity ϵ ($0.1 < \epsilon < 1.0$). The logarithmic temperature scale on the temperature axis is then defined by equation [3].

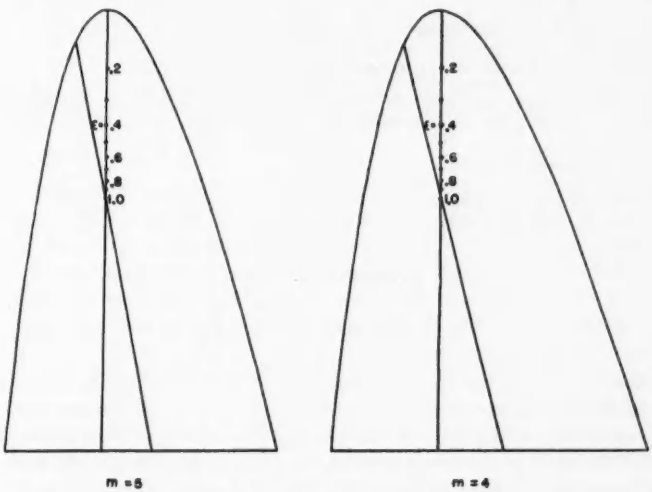


FIG. 2. Details of templates.

We have used these graphs to prepare two templates in thin lucite as in Fig. 2. Each template has etched on its surface the two straight lines x = constant through the maximum, and the T axis described above. The emissivity values from 0.1 to 1.0 are arranged in a logarithmic scale to allow the radiation

rate to be read at any arbitrary emissivity in this range, by moving the template down so that the required emissivity value is superposed on the required temperature. For many purposes, this device permits sufficiently accurate ($\approx 2\%$) numerical values to be read directly. We read the radiant power values ($m = 5$) on the left-hand ordinate and quantum flow rates ($m = 4$) on the right-hand ordinate. The appropriate factors, respectively $2\pi hc^2$ and $2\pi c$, have been included in [1*a*] to give the hemispherical fluxes per cm.^{2} sec. directly when multiplied by $d\lambda$. The reader can easily construct a similar pair of graphs for $m = 3$ or 2, or extend these graphs to different temperature regions as required.

The radiation constants are now well enough known that further changes are unlikely to affect J_λ by more than $\backsim 1\%$. From Planck's law, we write

$$\frac{dJ_\lambda}{J_\lambda} = \frac{dc_1}{c_1} - \left[\frac{\exp(c_2/\lambda T)}{\exp(c_2/\lambda T) - 1}\,\frac{c_2}{\lambda T}\right]\frac{dc_2}{c_2}.$$

The bracketed expression is called K in Fowle's I.C.T. article, Vol. 5, p. 242, and may be safely approximated by $c_2/\lambda T$ in the above equation, except in the Rayleigh–Jeans region.

It is a pleasure to acknowledge the interest of Dr. D. Derry, who has checked the derivations. We wish also to thank the Defence Research Board of Canada for support and permission to publish this note.

1. Benford, F. J. Opt. Soc. Amer. 29: 92. 1939.
Worthing, A. G. J. Opt. Soc. Amer. 29: 97, 101. 1939.
2. Czerny, M. and Röder, H. Ergeb. exakt. Naturw. 16: 70. 1938.
3. W.P.A. Misc. Phys. Tables, Natl. Bur. Standards (U.S.), 1941, p. 12.
Radiation Slide Rule, Gen. Elect. Co. (See Canada, A. H. Gen. Elec. Rev. 51: 50. 1948.)
Makowski, M. W. Rev. Sci. Instr. 20: 876. 1949.

Received November 17, 1954.
Physics Department,
University of British Columbia,
Vancouver, British Columbia.

NUCLEAR INTERACTION OF K MESONS*

By A. Husain† and E. Pickup

We have recently (5) made an analysis, by means of scattering ($p\beta$) and grain counting measurements, of shower tracks from stars formed in Ilford G5 emulsions during a high altitude balloon flight; a mass spectrum of the particles identified showed peaks corresponding to π mesons, protons, deuterons, and K mesons with a mass 925 m_e $\pm 8\%$. In an extension of this work, now in progress, further K mesons have been identified, and the main purpose of this report is to discuss some interesting features of these.

The present measurements were made in one of a batch of 600μ, stripped G5 emulsions exposed in a "Skyhook" balloon flight for 16 hr. at 95,000 ft.,

*Issued as N.R.C. No. 3566.
†National Research Laboratories Postdoctorate Fellow.

and Fig. 1 shows the results obtained so far. The emulsion was processed in the usual way, ionization measured by blob counting, and $p\beta$ by the usual multiple scattering method. The electron plateau blob density, which has not yet been

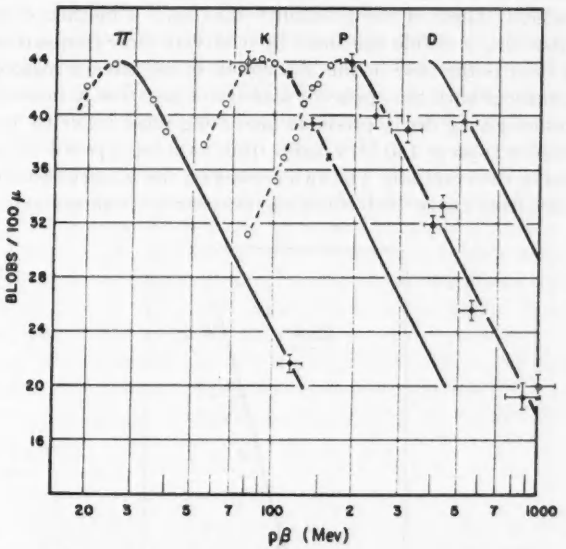


FIG. 1. Variation of $p\beta$ with ionization for shower tracks. The errors shown are standard errors, taken as $(75/n)\%$ for blob counting and $(75/N)\%$ for scattering ($p\beta$), where n = number of blobs and N = number of independent cells.

precisely determined, was 17 ± 1 blobs per 100μ. The blob counting results are corrected for variation of development with depth in the emulsion. In Fig. 1 the best line is drawn through the proton points, the π meson and deuteron curves being drawn parallel to this, assuming the known mass values. The K meson curve is drawn parallel to the others passing through the point at $p\beta$ = 140 Mev., which corresponds to a mass of 950 m_e. The curves show the effect of saturation under the conditions of microscopy and blob counting used here, and the open circles on the π, K, and P curves represent, in each case, measurements along a single track coming to rest in the emulsion. For these $p\beta$ was obtained from the measured residual range, using the tables of Fay, Gottstein, and Hain (3), although $p\beta$ was also verified by scattering.*

The K meson starting at $p\beta$ = 100 Mev. and coming to rest was emitted in a star of type $13+1p$, had a residual range of 16.5 mm., and was unique in that it did not give any detectable decay product or absorption star. There is a small chance that a minimum ionization particle, which was not recognized, was emitted. Fry, Schneps, and Swami (4) have also reported two cases of

**The masses of this proton and K meson were also determined using the "constant sagitta" method of measuring scattering, and this gave values of $2100\pm370\ m_e$ and $1080\pm190\ m_e$ respectively.*

K mesons coming to rest with no associated tracks. It seems likely that these events represent the nuclear absorption of negative K mesons with the emission of neutrons, π^0 or θ^0 mesons, or Λ^0 particles. There could be a very short nuclear recoil with a range $\lesssim$ one grain diameter which would not be recognized in the emulsion. There is the possibility that such a method of absorption, without producing a visible star, may be relatively more frequent for negative K mesons than is the case in the absorption of negative π mesons, and this may be connected with the apparent scarcity of negative K mesons compared with K mesons giving decay products (assuming these latter to be positive).

The K meson at $p\beta = 140$ Mev. came from a star of type $4+0n$, but did not come to rest in the emulsion. The two crosses on the K curve on either side of this point are from range–blob counting measurements on sections at the two

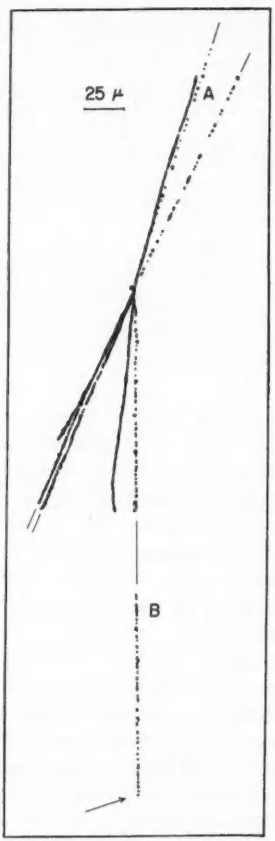


FIG. 2. Photomicroscopic tracing of star. *A* is identified as proton, $p\beta = 1$ Bev. *B*, which disappears in flight in emulsion, is identified as K meson with mass = $920 \pm 170\ m_e$.

ends of the track, the mean range being taken as that corresponding to the measured value of $p\beta$ at 140 Mev. The K meson at $p\beta = 80$ Mev. is the track B in the star illustrated in Fig. 2. Although this track was very short (2.3 mm.) an identification was attempted since the track stopped ionizing abruptly as shown by the arrow in Fig. 2. Blob counts and scattering measurements gave a combined standard error of 18% in the mass value. In this star it was also possible to identify track A, and this is the proton with $p\beta = 1$ Bev. in Fig. 1. Assuming B to be a K meson as identified, the arrow indicates what seems to be an interaction in flight with hydrogen or a heavier nucleus. Again there could be an unrecognized nuclear recoil with a range one grain diameter, although no radioactive decay electron could be seen, such as might be expected from a residual isotope. The possibilities are a neutron star or probably a reaction of the type $K^-(p, n)\ \pi^0$ or θ^0, or the production of a Λ^0 particle. Because of the lifetime, associated heavy mesons or hyperons are unlikely to be detected in an emulsion, although cases of γ ray showers (π^0 decay) (2), and a Λ^0 particle (1) associated with a K meson stopping in a metal plate have been observed in cloud chamber work.

It is also of interest to note that the present K mesons, as well as those in our earlier work (5) and those in the work of Fowler and Perkins (6), are all of relatively low energies, although in our work they have all come from fairly low energy stars.

1. Barker, K. H. Duke Univ. Conf. II, 52. 1954.
2. Bridge, H. S. Duke Univ. Conf. II, 51. 1954.
3. Fay, H., Gottstein, K., and Hain, K. Suppl. del Nuovo cimento, 11, No. 2: 234. 1954.
4. Fry, W. F., Schneps, J., and Swami, M. S. University of Wisconsin preprint.
5. Husain, A. and Pickup, E. Phys. Rev. In press. 1955.
6. Powell, C. F. Suppl. del Nuovo cimento, 11, No. 2: 165. 1954.

Received January 18, 1955.
Division of Physics,
National Research Council,
Ottawa, Canada.

THE PHYSICAL SOCIETY

MEMBERSHIP of the Society is open to all who are interested in Physics.

FELLOWS pay an Entrance fee of £1 1*s*. ($3.00) and an Annual Subscription of £2 2*s*. (~~$~~6.00).

STUDENTS: A candidate for Studentship must be between the ages of 18 and 26, and pays an Annual Subscription of 7*s*. 6*d*. ($1.10).

MEETINGS: Fellows and Students may attend all Meetings of the Society including the annual Exhibition of Scientific Instruments and Apparatus.

PUBLICATIONS include the *Proceedings of the Physical Society*, published monthly in two sections, and *Reports on Progress in Physics*, published annually. Volume XVII, 1954, is now available (price 50*s*. ($7.15)). Members are entitled to receive many of the Publications at a reduced rate.

Further information can be obtained from:

THE PHYSICAL SOCIETY

1, LOWTHER GARDENS, PRINCE CONSORT ROAD

LONDON, S.W.7, ENGLAND

CANADIAN JOURNAL OF PHYSICS

Notes to Contributors

Manuscripts

(i) ***General.*** Manuscripts, in English or French, should be typewritten, double spaced, on paper 8½×11 in. **The original and one copy are to be submitted.** Tables and captions for the figures should be placed at the end of the manuscript. Every sheet of the manuscript should be numbered.

Style, arrangement, spelling, and abbreviations should conform to the usage of this journal. Names of all simple compounds, rather than their formulas, should be used in the text. Greek letters or unusual signs should be written plainly or explained by marginal notes. Superscripts and subscripts must be legible and carefully placed.

Manuscripts should be carefully checked before they are submitted; authors will be charged for changes made in the proof that are considered excessive.

(ii) ***Abstract.*** An abstract of not more than about 200 words, indicating the scope of the work and the principal findings, is required, except in Notes.

(iii) ***References.*** References should be listed **alphabetically by authors' names,** numbered, and typed after the text. The form of the citations should be that used in this journal; in references to papers in periodicals, titles should not be given and only initial page numbers are required. All citations should be checked with the original articles and each one referred to in the text by the key number.

(iv) ***Tables.*** Tables should be numbered in roman numerals and each table referred to in the text. Titles should always be given but should be brief; column headings should be brief and descriptive matter in the tables confined to a minimum. Vertical rules should be used only when they are essential. Numerous small tables should be avoided.

Illustrations

(i) ***General.*** All figures (including each figure of the plates) should be numbered consecutively from 1 up, in arabic numerals, and each figure referred to in the text. The author's name, title of the paper, and figure number should be written in the lower left corner of the sheets on which the illustrations appear. Captions should not be written on the illustrations (see Manuscripts (i)).

(ii) ***Line Drawings.*** Drawings should be carefully made with India ink on white drawing paper, blue tracing linen, or co-ordinate paper ruled in blue only; any co-ordinate lines that are to appear in the reproduction should be ruled in black ink. Paper ruled in green, yellow, or red should not be used unless it is desired to have all the co-ordinate lines show. All lines should be of sufficient thickness to reproduce well. Decimal points, periods, and stippled dots should be solid black circles large enough to be reduced if necessary. Letters and numerals should be neatly made, preferably with a stencil (**do NOT use typewriting**) and be of such size that the smallest lettering will be not less than 1 mm. high when reproduced in a cut 3 in. wide.

Many drawings are made too large; originals should not be more than 2 or 3 times the size of the desired reproduction. In large drawings or groups of drawings the ratio of height to width should conform to that of a journal page but the height should be adjusted to make allowance for the caption.

The original drawings and one set of clear copies (e.g. small photographs) are to be submitted.

(iii) ***Photographs.*** Prints should be made on glossy paper, with strong contrasts. They should be trimmed so that essential features only are shown and mounted carefully, with rubber cement, on white cardboard with no space or only a **very** small space (less than 1 mm.) between them. In mounting, full use of the space available should be made (to reduce the number of cuts required) and the ratio of height to width should correspond to that of a journal page (4¾×7½ in.); however, allowance must be made for the captions. Photographs or groups of photographs should not be more than 2 or 3 times the size of the desired reproduction.

Photographs are to be submitted in duplicate; if they are to be reproduced in groups one set should be mounted, the duplicate set unmounted.

Reprints

A total of 50 reprints of each paper, without covers, are supplied free. Additional reprints, with or without covers, may be purchased.

Charges for reprints are based on the number of printed pages, which may be calculated approximately by multiplying by 0.6 the number of manuscript pages (double-spaced typewritten sheets, 8½×11 in.) and including the space occupied by illustrations. An additional charge is made for illustrations that appear as coated inserts. The cost per page is given on the reprint requisition which accompanies the galley.

Any reprints required in addition to those requested on the author's reprint requisition form must be ordered officially as soon as the paper has been accepted for publication.

Contents

Page

A Suggested Method for Studying the Mechanism of Energy Transfer in Collisions—*Ta-You Wu* - - - - - - - - - - - - 151

Nuclear Magnetic Resonance Spectrum of B^{11} in Kernite—*H. H. Waterman and G. M. Volkoff* - - - - - - - - - - - - 156

Forward-scattering of Radio Waves by Meteor Trails—*P. A. Forsyth and E. L. Vogan* - - - - - - - - - - - - - - - - - - 176

Scattering of a Plane Wave from a Circular Dielectric Cylinder at Oblique Incidence—*James R. Wait* - - - - - - - - - - 189

The Topography of Solid-Liquid Interfaces of Metal Crystals Growing from the Melt—*C. Elbaum and B. Chalmers* - - - 196

The Pulse Height Distribution from a Sodium Iodide Single Crystal Scintillation Counter and the Measurement of Gamma Ray Fluxes—*G. M. Griffiths* - - - - - - - - - - - - - - - 209

The Pulse Height Distribution from Boron Trifluoride Proportional Counters Irradiated with 4.87-Mev. Neutrons—*D. B. James, W. Kubelka, S. A. Heiberg, and J. B. Warren* - - - - - - - 219

Ferromagnetic Domain Patterns on Single Crystals and Bicrystals of Nickel—*Ursula M. Martius and K. V. Gow* - - - - - - - 225

The Resolution of Four-dimensional Vector Fields and Tensor Fields, and Its Application to Electrodynamics—*N. L. Balazs* - 235

Long Distance V.H.F. Fields. I. Partial Reflection from a Standard Atmosphere—*F. H. Northover* - - - - - - - - - - - - - 241

A Note on Black Body Radiation—*A. M. Crooker and W. L. Ross* - 257

Nuclear Interaction of K Mesons—*A. Husain and E. Pickup* - - - 260

Printed in Canada *by* University of Toronto Press